UNIVERSITY OF SOUTHAMPTON

FACULTY OF ENGINEERING, SCIENCE AND MATHEMATICS

Engineering Materials and Surface Engineering Group

School of Engineering Sciences

Investigation of Damage in Laminated Carbon Fibre Composites Using High Resolution Computed Tomography

by

Peter Michael Wright

Thesis for the degree of Doctor of Philosophy

April 2011

Supervisors:

Professor S. Mark Spearing

Professor Ian Sinclair

Engineering Materials and Surface Engineering Group

School of Engineering Sciences

UNIVERSITY OF SOUTHAMPTON

ABSTRACT

FACULTY OF ENGINEERING, SCIENCE AND MATHEMATICS
SCHOOL OF ENGINEERING SCIENCES

Doctor of Philosophy

INVESTIGATION OF DAMAGE IN LAMINATED CARBON FIBRE COMPOSITES USING HIGH RESOLUTION COMPUTED TOMOGRAPHY

by Peter Michael Wright

Laminated fibre reinforced polymer matrix composites have been used in design and manufacture for more than 50 years, exploiting desirable material properties such as high specific strength and stiffness, enabling large weight savings to be made on structural components. To take full advantage of this class of materials a comprehensive knowledge of behaviour under different service conditions is required. This thesis illustrates the degree to which this is currently achieved, and describes the motivation and progression of an experimental and theoretical analysis of the static damage growth in carbon fibre reinforced polymers.

Notched carbon fibre-epoxy cross-ply composite samples have been manufactured and loaded in uni-axial tension. Synchrotron radiation computed tomography (SRCT) has been used to characterise in 3-D the initiation and evolution of damage during in situ loading. Characteristic splitting, off-axis matrix cracking, interlaminar cracking and fibre failure within the samples were identified and the interaction of the damage mechanisms during crack growth has been evaluated. Splitting in the plies aligned with the loading direction was studied in greater detail, including measurements of crack opening displacement and shear deformation at crack flanks.

3-D finite element models of splitting have been developed based on the observed damage and specimen microstructure from the SRCT results. Thermal residual stress and mechanical loading conditions were simulated for comparison with the experimental findings. Effects of local microstructural inhomogeneities were also embedded in models of varying complexity to assess the degradation of the results or model predictions due to simplifications or homogenisation. Significant discrepancy was found between the measured experimental data and finite element predictions due to simplifications in the model. Likely candidates for the over-prediction of crack growth include the effects of transverse ply cracks, delaminations and the lack of symmetrical damage formulation. Of particular significance is the confirmation that, via qualitative observations and quantitative data extraction, SRCT has facilitated the first known instance of direct full field comparison of model predictions for composite damage for a practical engineering layup.

CONTENTS

LIST OF TABLES

LIST OF FIGURES

DECLARATION OF AUTHORSHIP

I, Peter Wright declare that the thesis entitled ‘Investigation of Damage in Laminated Carbon Fibre Composites Using High Resolution Computed Tomography’ and the work presented in the thesis are both my own, and have been generated by me as the result of my own original research. I confirm that:

- this work was done wholly or mainly while in candidature for a research degree at this University;
- where any part of this thesis has previously been submitted for a degree or any other qualification at this University or any other institution, this has been clearly stated;
- where I have consulted the published work of others, this is always clearly attributed;
- where I have quoted from the work of others, the source is always given. With the exception of such quotations, this thesis is entirely my own work;
- I have acknowledged all main sources of help;
- where the thesis is based on work done by myself jointly with others, I have made clear exactly what was done by others and what I have contributed myself;
- parts of this work have been published as indicated in the list of publications provided with this manuscript.

Signed:

Date:

ACKNOWLEDGEMENTS

The work contained within this thesis would not have been possible without the assistance, advice and contributions from particular individuals and groups.

Exceptional thanks go to my two supervisors; Professor Mark Spearing and Professor Ian Sinclair for their depth of knowledge, experience and continuous guidance throughout the project.

The staff in the Engineering Materials department, Graduate School office and Finance office have been tireless in their efforts behind the scenes to promote professional development and to support the administrative requirements of this doctorate.

The experimental work has been made possible with the assistance and craftmanship of the technicians, in particular Rob Barnes and Chris Williams. The European Synchrotron Radiation Facility provided experimental facilities that were integral to this thesis, with assistance provided by Greg Johnson in using beamline ID19. Essential carbon fibre composite material was supplied by Airbus, while funding was provided by EPSRC, grant EP/E003427/1. Professor Spearing also holds a Royal Society Wolfson Research Merit Award.

Thanks also goes to friends and colleagues within the Engineering Materials and Bio-engineering departments, who have offered an invaluable forum for academic discussion and have given up their time either to help towards completing this PhD, or to participate in the many distractions that extended it.

To all who have helped me along the way to this achievement, I am truly grateful.

CHAPTER 1

INTRODUCTION

1.1 Background and motivation

Laminated carbon fibre reinforced polymer (CFRP) composites are modern engineering materials with a wide variety of applications ranging from sports equipment to high performance aircraft. Although often expensive, they are attractive because of enhanced material properties, particularly their high specific strength and stiffness. In comparison with metals, ceramics and polymers, CFRP composites are relatively new materials and while their macro- and micro-mechanical behaviour has been well defined with principal damage mechanisms readily identifiable; their interactions within a complex microstructure and the resultant damage growth are not well understood. As a result, failure is often difficult to predict and the commissioning of designs that incorporate composites is generally dependant either on costly multi-scale models being rigorously tested for in-service failure or on overdesigning to ensure structural integrity, compromising on weight saving advantages.

Industrial design for critical structures often follows a building-block approach, where, for the particular example of aircraft structure certification, material design: "*must be established on the basis of experience or test*", "*conform to approved specifications (...) that ensure their having the strength and other properties assumed in the design data*" and "*take into account the effects of environmental conditions, such as temperature and humidity, expected in service*" [1]. In order to comply with certification requirements the number of tests performed for a particular specimen scales with the size of the specimen under test [2]. 1000's of tests are performed at the small-scale coupon level to determine parameters such as material behaviour, strength and failure modes. 100's of tests might be carried out at the element or detail level for a specific part to investigate environmental factors and potential size and geometry effects. 10's of tests carried out for a sub-component validate the accuracy of predictions based on previous tests. A few tests on a complete component under service conditions are required to validate design concepts and verify FE models. One full-scale test of the entire assembly allows certification of final performance and fitness for service. Design modifications have severe cost implications as the test procedure advances through the building block chain, providing clear evidence that there are significant advantages to 'virtual testing' that would reduce the dependence on expensive physical tests.

Driven by this motivation, many models have been developed that characterise and predict damage as a guide to various strength and lifeing parameters [3–10]. However, due to the complex nature of composite damage growth these models are often empirically based and do not encompass the micro-mechanisms that govern failure. Moreover they are often fitted to the test samples from which the data sets are produced and cannot, therefore, be truly predictive since alternative material constructions would require alternative fitting functions. There is a general lack of confidence in most current failure models as highlighted in the 'World-Wide Failure Exercise' (WWFE) [10–12] in which 19 leading theories for predicting failure in laminated composites were compared with 14 experimental test cases that included a variety of lay-ups, materials and in-plane loading conditions. The principal findings of the report concluded that for each of the theories, none adequately matched the experimental findings in all test areas. The three most highly ranked theories achieved an accuracy within ±50% of the ultimate laminate failure stress in 80% of the tests, and accuracy within ±10% of the ultimate laminate failure stress in just 30% of the tests. The results for the remainder of the theories showed an even lower success rate with differences in the failure strengths of multi-directional laminates of approximately 620% and a very large spread between the highest and lowest predicted strength values. With little unanimity between empirical or phenomenological models coupled with the expert knowledge required for execution of these models in a practical environment it is unlikely that commercial designers would consider these models over physical tests. A computational approach will gain acceptance only if it can be readily implemented, and can predict failure parameters (strength, deformation, material property degradation etc.) within consistent limits of confidence.

With powerful computing facilities readily available to engineering communities, FE models are capable of resolving increasingly complex configurations and are becoming more commonplace in the study of composites under load. To have true confidence in the output of FE simulations, the applied model must incorporate the effects of the physical mechanisms that govern the problem to be analysed. As with all numerical models, however, there will always be elements of simplification that will cause the simulation to deviate from the true physical situation. Care must therefore be taken in the analysis to ensure that a given model provides meaningful results and that the modeling approach is appropriate to the particular engineering problem to be simulated. Many current FE models are based either on a micromechanical approach where particular mechanisms of damage that can be solved numerically are modeled, or a continuum damage approach where damage is homogenised within a region and a fitted failure criterion is applied. Both approaches have particular strengths, but also weaknesses that prevent the models from predicting the response of an arbitrary composite structure based on different configurations. With material microstructural effects and multiple damage mechanisms affecting composite crack growth, micro-mechanical models become increasingly computationally expensive as element behaviour is required to simulate each of the governing physical processes. These mechanisms and physical processes are homogenized with continuum elements where local properties are smeared to produce a bulk response. This approach is more amenable to efficient FE processing, however accuracy is sacrificed for the computational gains and potentially significant details are lost during the homogenization. FE models comprising cohesive elements, termed cohesive zone models (CZM) have emerged as a promising approach to bridge between damage mechanics and micro-mechanical approaches and are gaining popularity in modeling the behaviour of composite materials [13, 14]. Based on the earlier strip yield theory developed by Dugdale and Barenblatt [15, 16], cohesive elements are continuum elements that obey a traction-separation law (τ-δ), which is usually either bi-linear or trapezoidal. The characteristics of the element are determined by the shape and type of the cohesive relationship, with principal features including initial stiffness, maximum strength before the onset of stiffness degradation and ultimate traction elimination at a corresponding critical separation. With the integral of the τ-δ relationship representing the energy required for the crack to advance by the element edge length, there is a physical trend embedded within the components of a CZM, while the continuum elements can be readily introduced into FE models. If the cohesive elements can be accurately calibrated to a given material system and lay-up using experimental data then there may be scope for the CZM to become a more pragmatic tool for the design of composite structures in terms of lifeing and damage tolerance. This premise, coupled with the more general findings of the WWFE, that there exists a significant lack of experimental data for comparison with model predictions, forms the motivation for the work contained in this thesis; in which an experimental study of CFRP damage growth modeling is described. In addition to the requirement for more successful models, this project aims to develop a data rich mechanics approach to experimentally validated, physically based modelling.

The focus of the work has been directed at *in situ* experimental analysis of damage growth in samples loaded in uni-axial tension using X-ray computed tomography (CT) and synchrotron radiation computed tomography (SRCT) to identify the parameters that would enable calibration of a CZM and subsequent prediction of failure in other laminate configurations. CT and SRCT have been used to obtain exceptionally detailed 3-D qualitative observations and quantitative data sets for the initiation and progression of damage through to laminate failure for generic FE model development and validation. The extracted experimental data allows direct full field comparison with model predictions of crack opening and sliding displacements and crack growth with load. The model incorporates microstructural information, material behaviour and crack front geometry with direct mechanical loading and thermal residual stresses to determine the sensitivity of model predictions to averaging the material properties of local microstructure or the effects of specific damage and failure mechanisms. During the course of the study attention has been drawn away from the development of specific CZMs such as those of Cox and Yang [17] and the scope of the work presented here is concentrated on the use of the comprehensive data sets to demonstrate that qualitative and quantitative observations afforded by SRCT can be utilized to calibrate or validate any given model according to the type, mode and mechanism of damage growth.

1.2 Thesis structure

The content of this report is based around four core journal papers that describe the findings of this work and are set out as follows:

Chapter 2 contains a literature review that describes the background theory, principles and techniques required to reproduce the work documented in the main body of this text and demonstrate its validity. Chapter 3 describes the experimental methods used to generate the results with which the modeling predictions were compared. Chapters 4 to 7 comprise the results, discussion and conclusions of the papers. Chapter 4 demonstrates the potential of computed tomography as a technique to obtain high-resolution images of cracking behaviour in composite laminates and enable an initial qualitative analysis of a specimen near its terminal damage state. Chapter 5 expands the experimental approach to include a loading regime that ranges from initial onset of damage to failure to enable a more in depth evaluation of the mechanisms involved in laminate failure. The initial finite element modelling approach is described, and a comparison is made with the experimental results. Key mechanisms that are identified from the SRCT data and not captured by the model are acknowledged and addressed in chapters 6 and 7. Chapter 6 discusses the results of a model in which microstructural details are more accurately represented and material properties are adjusted to approximate the local toughening behaviour of the laminate. Chapter 7 describes the predictions from the model in which crack front pinning is reproduced from the experimental results. Chapter 8 describes the conclusions of this work, and includes a discussion of resultant research potential. Due to the nature of the papers as articles that stand alone as coherent reports, some information is common and therefore subject to repetition between the chapters. Where this occurs it will be highlighted as such.

As part of the EPSRC funded proposal a Post Doctoral researcher was assigned to the project and was responsible for segments of the work described in the following chapters. Those segments are predominantly image post-processing and extraction of quantitative data from experimental results, however all work with ownership residing with third party researchers will be referenced accordingly. During the period over which this work was carried out, the Post Doctoral position was occupied by the following researchers: Dr Polly Sinnet-Jones [18]; Dr Xiaowei Fu [19]; Dr Andrew Moffat [20]; Dr Mark Mavrogordato [21].

1.3 Contributions to the current field of composite damage

There are five main areas concerning the assessment of composite damage to which contributions have been made from the work described in this thesis.

- First use of synchrotron radiation computed tomography to identify unambiguously sequential progression of damage mechanisms in $[90/0]_S$ CFRP from first damage initiation to failure.
- In situ full field and local displacement mapping made possible through novel processing of composite panels with fiducial particle embedding. Unique features have been identified and tracked between load states to determine the displacements.
- Development of a bespoke mechanical loading device for experimentation at the European Synchrotron Radiation Facility.
- Development of a 3-D FE model simulating the effects of toughening and crack pinning for comparison with CT data.
- Comprehensive data sets generated and made available for public access to compare with models for validation.

1.4 List of publications

The following journal papers and conference proceedings have been produced as a direct output from this work:

Journal papers

Wright, P.M., Fu, X., Sinclair, I., Spearing, S.M., Ultra high resolution computed tomography of damage in notched carbon fiber-epoxy composites. *Journal of Composite Materials*, 2008, **42**(19): pp. 1993-2002. doi:10.1177/0021998308092211.

Wright, P., Moffat, A., Sinclair, I., Spearing, S.M., High resolution tomographic imaging and modelling of notch tip damage in a laminated composite. *Composites Science and Technology*, 2010, **70**(10), pp. 1444-1452. doi:10.1016/j.compscitech.2010.04.012.

Moffat, A.J., Wright, P., Buffière, J.-Y., Sinclair, I., Spearing, S.M., Micromechanisms of damage in 0° splits in a $[90/0]_S$ composite material using synchrotron radiation computed tomography. *Scripta Materialia*, 2008, **59**(10): pp. 1043-1046. doi:10.1016/j.scriptamat.2008.07.034.

Moffat, A.J., Wright, P., Helfen, L., Baumbach, T., Johnson, G., Spearing, S.M., Sinclair, I., *In situ* synchrotron computed laminography of damage in carbon fibre-epoxy $[90/0]_S$ laminates. *Scripta Materialia*, 2010, **62**(2): pp. 97-100. doi:10.1016/j.scriptamat.2009.09.027.

Renault, A., Moffat, A.J., Wright, P., Sinclair, I., Spearing, S.M., Direct measurement of transverse ply crack opening using synchrotron X-ray tomography and comparison with models. *Journal of Composite Materials*, in review.

Wright, P., Mavrogordato, M.N., Sinclair, I., Spearing, S.M., Full field assessment and modelling of damage in a laminated composite using synchrotron radiation computed tomography. Part I: Effect of spatial variation in microstructure. In preparation.

Wright, P., Mavrogordato, M. N., Sinclair, I., Spearing, S.M., Full field assessment and modelling of damage in a laminated composite using synchrotron radiation computed tomography. Part II: Crack pinning and toughening mechanisms. In preparation.

Mavrogordato, M. N., Wright, P., Sinclair, I., Spearing, S.M., High resolution computed tomography observations of damage progression within carbon fibre reinforced laminates under incremental static loading. In preparation.

Conference papers

Wright, P., Moffat, A., Fu, X., Buffière, J.-Y., Sinclair, I., Spearing, S.M., Very high resolution computed tomography of damage in laminated composites. *Proceedings of the 13th European Conference on Composite Materials*, Stockholm.

Wright, P., Moffat, A., Fu, X., Renault, A., Sinclair, I., Spearing, S.M., High resolution computed tomography for modelling laminate damage. *Proceedings of the 17th International Conference on Composite Materials*, Edinburgh.

Moffat, A. J., Wright, P., Buffière, J.-Y., Sinclair, I., Spearing, S. M., In situ calibration of cohesive zone models for composite damage. *Proceedings of the American Society for Composites 23rd Technical Conference*, Memphis.

Mavrogordato, M. N., Wright, P., Helfen, L., Sinclair, I., Spearing , S.M., Assessment of laminate damage micromechanisms using high resolution synchrotron radiation computed tomography & laminography. *Proceedings of the 14th European Conference on Composite Materials*, Budapest.

Burke-Veliz, A., Mavrogordato, M. N., Wright, P., Moffat, A., Sinclair , I., Spearing, S.M., FE modelling and validation of interacting cohesive zones in CFRP with high resolution imaging. *Proceedings of the 14th European Conference on Composite Materials*, Budapest.

CHAPTER 2

LITERATURE REVIEW

This review details the existing research, techniques and theory related to the work carried out in this project. Principal topics of fibre reinforced polymer composites, composite mechanics, damage mechanisms, failure processes specific to polymer composites, damage assessment techniques and modelling approaches are the focus of discussion. Further review is included in later chapters where it is intended to provide a greater level of detail for the more specific work to which it relates.

2.1 Composite materials

Composites are a class of materials typically constructed from at least two distinct component phases, possessing combined properties that are more desirable than those of the individual parent materials, for example improved stiffness, strength and toughness. Composites generally consist of a reinforcement embedded within a matrix and are divided into three principal categories dictated by the matrix material: polymer, metal and ceramic. The choice of reinforcement is dependent on the properties that are required from the composite, and selection is often based on a merit index according to those properties [22]. The matrix is usually continuous, however the reinforcement can assume many different architectures, with the most common examples consisting of fibres (continuous and discontinuous), particles, flakes or whiskers. The volume fraction of reinforcement to matrix the quality of the bond between the matrix and reinforcement and the surface treatment of the fibres are important considerations in composite design since these are key parameters in determining the engineering elastic constants on a micromechanical scale, and therefore the mechanical response to applied load.

2.1.1 Carbon fibre reinforced polymer matrix composites

This project is concerned only with laminated polymer matrix composites with continuous fibre reinforcement, specifically a carbon fibre-epoxy system and no further reference is made to the other systems. The laminate is constructed from individual plies of unidirectional fibres pre-impregnated with epoxy resin (pre-preg). Each ply has highly directional material properties and the stacking configuration, defined by the number of plies and their orientation relative to a reference direction has a strong influence on the mechanical behaviour of the laminate. The 4-ply laminate sequence used for the majority of the work described in this report is $[90°/0°/0°/90°]$ and is denoted as $[90/0]_{\mathrm{S}}$ where $0°$ is defined as being aligned to the loading direction and the coordinate system of $0°, 90°, z$ is used in conjunction with the more familiar system of x, y, z.

2.1.2 Mechanical response

The elastic macroscopic and microscopic behaviour of laminated composites is well defined for small deformations or loads in which no significant damage is induced [23]. Theoretical values of the elastic engineering constants can be calculated using a rule of mixtures, however this approach is based on assumptions that are not realistic in practical manufactured laminates, for example imperfect bonding at the fibre-matrix interface or local variations in fibre volume fraction. Experimental determination of the elastic constants would usually provide a more accurate basis for defining laminate behaviour [24]. In this context, macroscopic analysis implies that the bulk material is not affected by the small-scale fibre-matrix interactions, with the mechanical properties averaged across the structure. A microstructural approach to the analysis of material behaviour will identify and address these interactions with individual mechanisms accounted for.

When a single lamina is loaded in the longitudinal fibre direction (0°), the high fibre stiffness results in the majority of the load being carried by the fibre rather than the matrix. In the transverse direction the fibres contribute little reinforcement and the properties of the matrix play a stronger role in determining the behaviour of the structure. Elastic theory is usually applied to initial evaluations of mechanical loading since the graphite fibres exhibit mainly brittle, linear elastic behaviour [22, 25]. However, defects have a significant impact on brittle materials and a statistical approach is sometimes required when addressing final failure of carbon fibres [26]. The work described in this thesis focuses on splitting in the 0° plies. While the properties of the fibre/matrix interface and the surface treatment of the fibre have a large effect on the mechanisms of splitting, the stress state within the 0° plies is dominated by the properties of the brittle fibres, and analysis is therefore restricted to linear elastic behaviour.

2.2 Damage and failure processes

One of the principal aims of composite damage analysis and modeling is to enable accurate predictions of laminate strength, life and damage tolerance in engineering structures. Conversely, one of the principal reasons why composite failure has not been adequately modelled to date is the complexity of the processes that govern the manner in which damage accumulates for varying geometries, loading regimes, material systems and lay-up configurations [12, 27, 28]. Damage evolution in fibre reinforced composite materials under tensile loading involves the interaction of multiple mechanisms, typically consisting of intralaminar matrix cracking, delamination, and fibre fracture [29, 30]. Analysis of the terminal damage state in notched cross-ply CFRP composites has been shown to consist of transverse ply matrix cracks in the outer 90° plies, fibre-aligned matrix splitting at the notch tip in the central 0° plies, accompanied by fibre failure and regions of self-similar growth of interlaminar delamination between the 90° and 0° plies [31, 32]. While the contribution from additional processes such as fibre bridging between delamination faces and resin behaviour may introduce nonlinear effects [33], the scope of the work presented here is restricted to linear elastic behaviour and the fracture mechanics concepts and approaches that are relevant to later modelling work are discussed below.

2.2.1 Energy approach

From the First Law of Thermodynamics, Griffith defined an energy-based condition for fracture to occur [34]. It was proposed that a crack would only grow if there is sufficient strain energy present to drive the formation of new surfaces. The net change in energy must be equal to or less than zero, according to

$$\frac{dE}{dA} = \frac{dE}{d\Pi} + \frac{dW_S}{dA} = 0 \,, \tag{2.1}$$

where E is the total energy, Π is the potential energy supplied by internal strain energy and external forces, and W_S is the work required to create the new surfaces with an increase in crack area, dA.

A parameter, G, was introduced by Irwin [35] as the energy release rate (ERR), or crack driving force relating to the energy available for an increment of crack growth such that

$$G = -\frac{d\Pi}{dA} \,. \tag{2.2}$$

When G reaches a critical value, G_C, the crack will extend and therefore constitutes a measure of fracture toughness:

$$G_C = -\frac{dW}{dA} = 2w_f \,, \tag{2.3}$$

where w_f is the energy required to generate a new crack surface. Although the formulation of ERR is no different in essence from the Griffith energy balance it is used as a more convenient form for the application to engineering problems [36]. Other energy based approaches are in frequent use, such as the J-integral [37, 38] for which the non linear energy release rate can be written as a path-independent line integral that uniquely characterises crack tip stresses and strains. Strain energy release rate, G, is the parameter used with modelling in this work.

2.2.2 Size effect

The effect of length scale plays an important role in the pursuit of accurate predictions for laminate failure and has been studied at length [39–42]. The damage mechanisms described earlier interact in a complex manner, and the influence of each mechanism on ultimate failure will be affected by the size of the specimen under test [43]. For example, the brittle behaviour of the graphite fibres is highly dependent on stress concentrations arising from material defects. The ‘weakest link’ theory forms the basis of the Weibull distribution that is used extensively in statistical modelling [41, 43–45]. For brittle materials the bulk is assumed to be constructed from a series of elemental links and the strength of the structure is dependent on the stress distribution at which the weakest link fails. Despite good agreement for many strength predictions for brittle materials such as ceramics, this approach has proved inconsistent and inconclusive for single filaments and fibre bundles [26]. Partial fitting to experiment data has been achieved, however the lack of accurate strength predictions for the simplified representation of fibre reinforcement indicates that statistical strength approaches for more complex, practical engineering laminate constructions are not sufficient to describe composite failure.

While a comprehensive study of size effects is outside the scope of the work presented here, a central component of the motivation for this work is derived from the need to understand the mechanisms that dominate at different laminate length scales. The general ‘building block’ approach to aerospace composite design [2], consisting of extensive mechanical tests across various length scales is heavily reliant on empirical data, with knock down factors applied in place of physically based models to achieve safe design. Computed tomography, described below, is a non-destructive 3-D imaging technique that presents an opportunity to observe the mechanisms involved in the accumulation of composite damage to determine the role of those mechanisms during the failure process.

2.3 Damage assessment

2.3.1 Overview of techniques

There are many techniques available to determine damage in carbon fibre reinforced composites, of which scanning electron microscopy (SEM), ultrasound and radiography are among the most commonly used [46–48]. SEM allows exceptionally high-resolution images of surface damage to be obtained [49–52], however in order to assess internal damage, specimens are usually subject to serial sectioning or other machining operations to expose the surface to be assessed. Sectioning artefacts such as machining damage are common, and their effect on experimental results is not easily determined with confidence. In addition, through-thickness resolution is limited to the increment in material removed. Ultrasound is a non-destructive technique that is readily implemented and while it is an effective method by which to detect damage [53–56], it is relatively coarse. Spatial resolution is low, and damage between adjacent plies cannot be directly distinguished. Radiographic projections can provide high-resolution images, however these are also planar with no through-thickness differentiation [57–61]. Also, unless the projections can be obtained during *in situ* experiments where cracks are held open, it is often difficult to identify damage without the use of radio-opaque dye-penetrant. Computed tomography (CT) has been increasingly used in recent years to exploit the capability of the technique to obtain three-dimensional, multi-scale resolution images of damage and material microstructure [62–65]. Although in-plane resolution is significantly lower than for SEM, the through-thickness resolution is much greater. The resolution that can be obtained is limited by specimen size, with high resolution images at the micron-scale generally requiring a specimen size of less than 2 mm. While high fidelity CT images require the experience of an expert user, good results can be obtained with minimal training. Furthermore, the non-destructive nature of CT with limited requirements for specimen preparation makes it an attractive technique for damage assessment.

2.3.2 X-ray computed tomography

Tomography is perhaps most widely recognised as the medical technique of the computed axial tomography (CAT) scan where the internal structure of a patient is imaged as a series of slices along the length of the body. In general, tomography is a technique used to obtain information about a slice of matter within a bulk object. Engineering applications employ computed tomography (CT) for much the same purpose: to analyse the structure of materials to characterise their response to a range of conditions, such as mechanical or thermal loading, for non-destructive inspection of manufactured components or to determine the integrity of materials in terms of defects, void content or other such features. Although there are several methods by which tomography is possible, for example ultrasonic, magnetic field and electric field, X-ray sources are the most widely used class.

The first application of computed tomography for density characterisation of soft tissue in the early 1970's [66] has evolved into the ability to resolve structural detail to sub-micron resolution in 3-D with little or no alteration to the material under test [67]. To acquire the same data previously, 2-D information would be gathered from successive sectioning of a material, which imposes a limit of section thickness resolution, often introduces damage or defects to the sectioned sample and destroys the specimen.

The principle of CT imaging is based on a relatively simple concept; however modern techniques involve complex algorithms. An X-ray radiograph involves the acquisition of a projection of a 3-D object on a radiosensitive detector. The information captured on the surface of the detector is a function of attenuated source X-rays along a path, x, described by the Beer-Lambert law,

$$I = I_0 \, e^{-\mu x} \,, \tag{2.4}$$

where I is the intensity, or power of the transmitted light, I_0 is the initial intensity and μ is the material attenuation coefficient from the photoelectric effect,

$$\mu(x, y, z) = K\rho \, \frac{Z^4}{E^3} \,, \tag{2.5}$$

for which K is a constant, ρ is the material density, Z is the material atomic number and E is the energy of the incident photons.

CT involves recording a series of radiograph projections as the sample is rotated as shown in Figure 2.1. The local value of attenuation for each point within the object for each radiograph is reconstructed, most commonly using filtered back-projection [68], to produce a 3-D volume representation of the sample [67, 69–71]. The attenuation through the sample is represented by a corresponding grey-scale in each radiograph image.

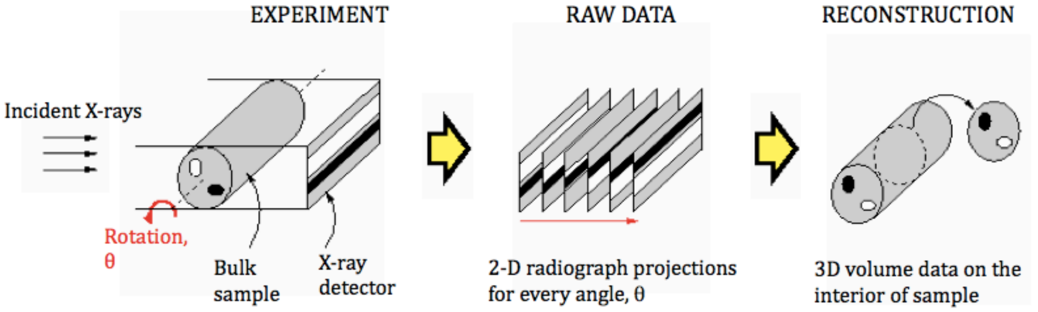

Figure 2.1: Schematic representation of volume reconstruction for computed tomography.

CT can be described in many contexts, however for engineering considerations two classifications are described here, differentiated by image resolution. Microfocus computed tomography (μCT) generally refers to resolutions of the reconstructed sample volume in the range of 5-10 μm using bench-top scale equipment. The second classification is synchrotron radiation computed tomography (SRCT), which is capable of greater volume detail, with submicron voxel resolution routinely achieved [72]. Compared to the relatively wide availability of commercial μCT facilities, synchrotron radiation facilities are few and consequently beamtime for SRCT experiments is considerably more valuable.

2.3.2.1 Microfocus computed tomography

X-rays can be generated by focusing accelerated electrons onto a suitable target, for example molybdenum or tungsten, by means of magnetic lenses. The incident electrons lose energy on interaction with the target producing X-rays, with the majority of the energy converted to heat that must be removed from the target area via a cooling system. A detector system and CCD camera record the intensity of the X-rays and are used to produce the 2-D radiographic projections of an object placed between the X-ray gun and the detector. μCT is a relatively new technology when compared to optical and electron microscopy, however the technique is reasonably well established within the material science community as a reliable method for producing high quality 3-D images [65, 73, 74]. Computed tomography has been applied to microstructural observations and analysis of composite damage; for example as a complimentary technique to SEM by Banyay et al. to study the microstructure of polymeric and composite foams to develop FE models of the cellular foams as materials for pressure vessels [73] and by Bayraktar, Bessri and Bathias to enable *in situ* observations of fracture processes in elastomeric matrix composites under static loading conditions [74]. Bayraktar, Antolonovich and Bathias observed *in situ* damage growth in elastomeric, wooden plastic, and metal matrix composites to determine the relationship between fatigue behaviour and material properties [75], while Torquato reviewed the potential role of CT in modelling the physical properties of composites [76]. Studies are not common, however, for carbon fibre reinforced epoxy composites. Damage assessment and characterisation of internal damage, including delamination and matrix cracking was carried out for glass and carbon fibre reinforced epoxy specimens by Schilling et al., in which observations were supported by the rendered images of segmented damage [77]. Symons used CT, ultrasound and optical microscopy to characterise impact damage and quasi-static indentation on CFRP laminated plates [78], and measurements of microstructural features within short-fibre reinforced polymer foams have been carried out in work by Shen, Nutt and Hull, providing quantitative analysis of fibre length distribution and fibre orientation [79]. Tsao and Hocheng used CT and ultrasound to investigate drilling induced delamination in woven cross-ply carbon fibre laminates. The extent of delamination within the specimens was measured using CT images and compared to ultrasound data to validate computed tomography as an effective technique for qualitative and quantitative analysis of internal structural damage [80].

2.3.2.2 Synchrotron radiation X-ray computed tomography

Synchrotron radiation computed tomography (SRCT) exploits a monochromatic, low divergence synchrotron source to obtain significantly greater image resolution than that of microfocus CT, while a high beam flux ensures a very high signal to noise ratio. A voxel resolution of 0.7 μm is routinely achieved at the European Synchrotron Radiation Facility (ESRF), where all SRCT experiments for this work were performed. The ESRF consists of a linear accelerator (linac) to introduce electrons into a circular booster synchrotron that increases the electron energy. Once the electrons have reached an energy of 6 GeV they are transferred to a larger storage ring (Figure 2.2). The generation of synchrotron radiation with the necessary properties for high resolution tomography is dependent on the electron interactions with bending magnets, undulators, wigglers and focussing magnets contained within the storage ring [81].

The bending magnets shown in Figure 2.3 are used to achieve the circular path of the electrons around the storage ring by controlling the magnitude of deviation from their free trajectory. The deflection of the electrons is a result of the Lorentz force that acts orthogonal to the direction of electron motion and the magnetic field vector. The synchrotron radiation is generated in a direction tangential to the electron trajectory during deflection and experiment hutches that make use of the synchrotron X-ray beams are located behind the bending magnets.

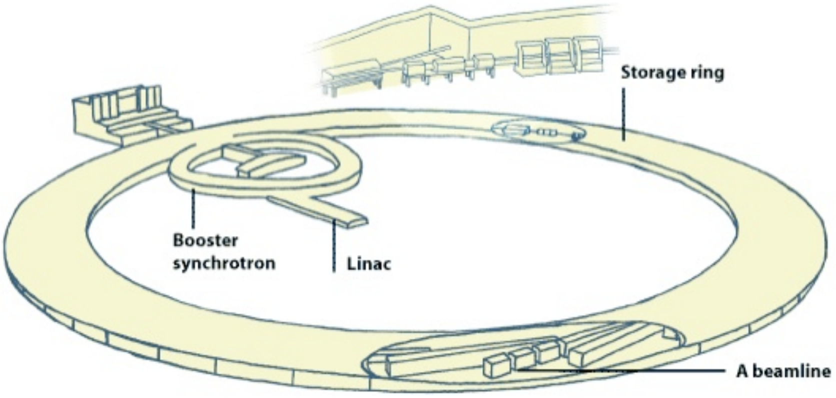

Figure 2.2: Electron storage ring at ESRF [81].

The purpose of the undulator as an insertion device is to generate a more powerful X-ray beam than that which is produced as a result of the bending magnet electron deflection alone. It consists of a series of magnets that deflect the electrons in a corresponding series of bending stages. The X-rays produced at each stage interfere constructively to provide an increase in intensity. A second insertion device called a wiggler is similar to the undulators but generates a wider spectrum of radiation. The focussing magnets are used on the straight sections of the storage ring and produce a

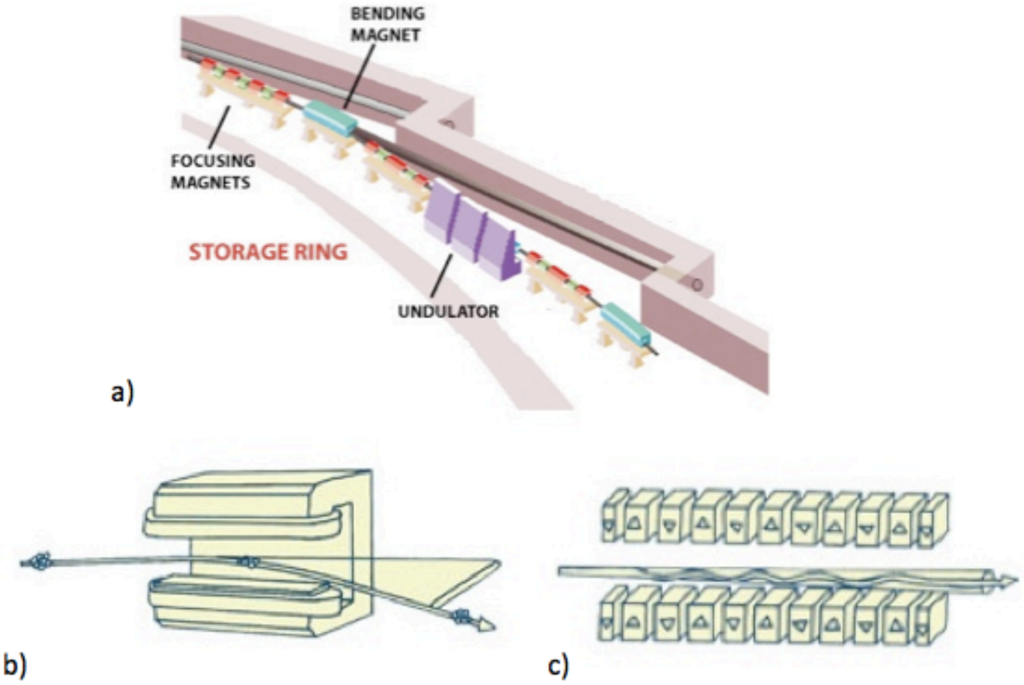

Figure 2.3: Detail of magnets within storage ring. (a) Configuration within storage ring; (b) bending magnet; (c) undulator. [81].

brighter source by focussing the beam. This acquisition of radiographic projections is similar to the more conventional conventional μCT technique; however a key difference is that the highly coherent beam enables the use of phase contrast to improve feature detection in materials with little variation in density and absorption coefficient through the bulk.

Phase Contrast

By varying the detector-to-sample distance during SRCT, Fresnel diffraction patterns can be exploited to improve the contrast between adjacent regions of varying material density. For samples with low density, or containing features that are a very similar density to the bulk, phase contrast can be a vital method by which to detect features such as cracks, voids and inclusions within a structure. When an X-ray beam is transmitted through a specimen, it experiences a phase shift due to interaction with the electrons within the specimen [82, 83, 83, 85, 86]. The phase shift will therefore depend on the (electron) density of the sample. Interference patterns in the wavefronts from the different phase shifts results in the formation of contrast in the image. At specific distances from the detector, different regimes will result in different patterns from the diffraction. Table 2.1 describes the different regimes where z is the distance of the specimen to the detector, d is the feature size and λ is the wavelength of the synchrotron radiation.

Table 2.1: Details of the regions distinguishable by varying the distance (z) of the camera from the sample [81].

Region	**Resultant Image Description**
Contact ($z = 0$)	Intensity distribution is a pure absorption image
Near field ($z < d^2/\lambda$)	Contrast is achieved due to sharp changes in the refractive index (*e.g.* at interfaces/defects)
Fresnel ($z \approx d^2/\lambda$)	Image becomes less of a resemblance to the specimen
Fraunhofer ($z > d^2/\lambda$)	The image intensity is a Fourier transform of the object transmission function

Figure 2.4 illustrates an example of near field, or ‘edge detection’ phase contrast. In Figure 2.4a the sample-detector distance is close to zero so there is no interference pattern and the resultant projection of the specimen is due to absorption only. The distance was adjusted for the projection in Figure 2.4b to obtain the bright fringe surrounding the reinforcement material.

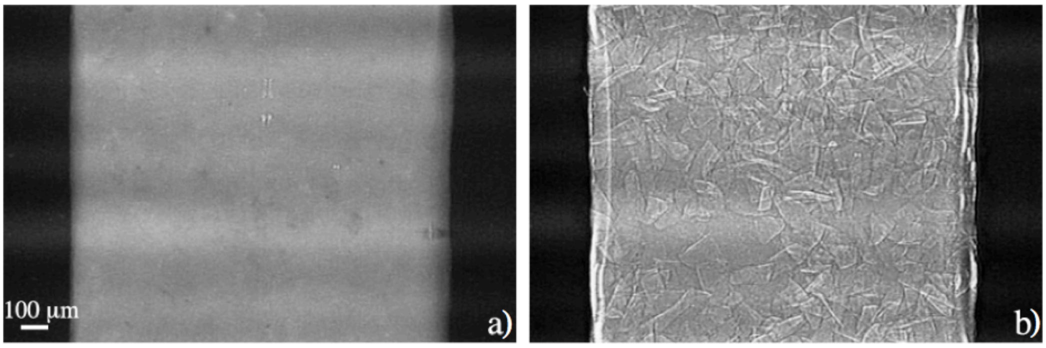

Figure 2.4: SRCT image of aluminium-based particle-reinforced SiC composite (a) absorption regime (detector-sample distance, z = 0.003 m), (b) edge detection regime employing phase-contrast (z = 0.83 m). Images reproduced from Cloetens et al, [82].

It is clear from the Table 2.1 and from Figure 2.4 that it is important to place the sample within the range of distances required for near field (edge detection regime).

Artefacts

There are a number of physical effects that can cause degradation of CT image quality [87–91]. Beam hardening is manifested as streaks and cupping in images across a sample where the edges of a sample often appear brighter than the centre. For polychromatic X-ray sources, lower energies are more easily absorbed. As the beam passes through the specimen, the lower energy radiation is more likely to be absorbed, thus changing the energy spectrum. The variation in the X-ray energy spectrum at the detector from different attenuation paths (*e.g.* from variations in section thicknesses as the sample is rotated) is the cause of beam hardening. The synchrotron radiation X-rays are monochromatic and beam hardening artefacts have not been observed in these SRCT experiments. Ring artefacts are the most common artefact and appear as concentric rings in the reconstructed axial images. The cause of ring artefacts is the presence of defective pixels across the detector. The defective pixels will result in particular points in the 2-D projections having a slight deviation from the true grey-scale value. As the sample is rotated the greyscale deviation from the same defective pixel points will trace a ring in the image. Ring artefacts are also caused by badly corrected pixels in the projection. Centring errors due to unintentional translation of the specimen during stage rotation may be induced if the centre of rotation of the stage is not aligned with the centre of rotation of the sample or if the motors that control the specimen stage are subject to feedback errors. Streaking is due to inconsistent measurements of the attenuated X-rays and results in bright traces across an image emanating from the root feature. The most common causes are fullscale X-ray attenuation and edge gradient effects. Full-scale attenuation will arise when an object in the field of view is too dense for the X-rays to penetrate. Edge gradient effects are due to a sharp edge or interface between materials with a large difference in density, where the accurate representation of the true attenuation across adjacent detector pixels is not possible. Given that the accurate analysis of the volume is dependent on the quality of the reconstructed images, it is clear that great effort should be made to reduce the occurrence of artefacts.

Applications of SRCT

The use of SRCT to obtain volume information is established within many areas of materials science research. Examples from the literature include investigations of the development of microstructure in ceramics during sintering [92], the effect of void content on ductile crack growth in aluminium alloys [93], the characterisation of microstructural features to determine their influence on fatigue crack closure mechanisms within aluminium alloys [94] and within aluminium-silicon piston alloys [95], and very high resolution of the microstructural architecture of multiphase metals [96]. There are very few applications of SRCT to the study of composites in the literature, where the technique has been used predominantly to characterise composite microstructure, for example, the observation and measurement of the internal structure of a polymer sponge [97], and within the work of Cosmi *et al.* in which the orientation of short carbon fibres was determined within a thermoplastic specimen, separately identified from the matrix through the use of phase contrast [98]. SRCT was used for quantitative analysis of the relationship between fibre volume and orientation of continuous fibres within polymer- and metal-matrix composites [99], and the role of resin impregnation on the stress transfer between fibre-fibre bonds in paper sheets [100]. Analytical investigations include the structural response and strain fields of wood during three-point bend tests was evaluated by Forsberg *et al.* [101] and the tensile damage behaviour of metal matrix composites was investigated in the work by Williams *et al.* [102] in which a statistical analysis of the effect of voids and inclusions on fracture mechanisms is presented for specimens loaded to failure. The only work to investigate damage and failure in fibre reinforced polymer composites that has been identified to date is that by Aroush *et al.* [103]. SRCT scans of close-packed quartz bundles consisting of 125 fibres embedded in an epoxy matrix were performed during *in situ* tensile loading for comparison with a statistical strength model based on the size (N*) of a critical cluster of adjacent broken fibres. Observations of damage evolution were presented, and direct measurements provided evidence that existing models under-predict critical cluster size of broken fibres by a factor of between 3 and 5. The work provides valuable insight into the dominant damage mechanisms in the simplified representation of a uni-directional composite, and demonstrates the potential to expand the area of research to include laminates that consist of practical engineering layup configurations.

2.4 Modelling damage and fracture

Many modelling approaches have been used in an attempt to characterise the damage and fracture mechanics in composite materials, and they have been met with mixed success [3–10]. The characteristic damage that accumulates prior to failure evolves as complex interactions of both linear (fibre response) and potentially non-linear (matrix response) damage mechanics. Many of the models to date employ empirical factors to fit model predictions to experimental results [5, 104]. However, the complex interaction of the damage processes and the scale at which they occur are not readily transferable to these empirical models. The response from neither a change in laminate lay-up configuration nor component size can be predicted from existing data for alternative configurations. Those models that aim to predict parameters such as strength, fatigue life, residual stress and residual strength, and that do not rely completely on phenomenological approaches consist of two main categories. Continuum damage mechanics addresses the failure mechanisms from a global view, where individual damage mechanisms are homogenised and constructed around a failure criterion. Micromechanics provides a more detailed analysis of each physical process involved in fracture, but due to the complex damage interactions, exhibit difficulty in amalgamating the separate mechanisms. A further approach to modelling that has received recent interest is the cohesive zone model (CZM) [105–109]. CZMs are readily integrated into finite element programs, and show promise with regards to combining preferred modelling strengths from empirical, micromechanical and continuum damage approaches. A brief description of the main features of these modelling approaches is presented below.

2.4.1 Continuum damage mechanics

Continuum damage mechanics places little emphasis on the microstructural damage and attempts instead to define general homogenised damage propagation that leads to failure once a specified criterion has been reached. The criterion is often based on either empirical parameters or a mechanical approach such as a maximum stress or strain, where a ply is considered to have failed and contributes no further strength or stiffness to the laminate once the stress or strain has been exceeded. Continuum-based criteria have been derived to relate stresses and experimental measures of material strength to the onset of failure [7, 10], however since the microstructural detail is not considered, continuum damage models do not generally offer accurate predictions with modified material systems, lay-up configurations or size effects.

2.4.2 Micromechanical models

Individual damage mechanisms are modelled explicitly for micromechanical models. The models often incorporate elements of fracture mechanics, equating the strain energy release rate to the growth of new fracture surfaces [102, 110, 111]. Although the approach has a sound physical basis, it is not easily implemented into finite element models due to the complexity of the mechanism interactions. As such it is inherently difficult to model successfully or accurately and individual mechanisms of damage such as transverse ply cracking or delamination are usually modelled separately. In addition, since the application of fracture mechanics requires the presence of an existing crack, such models cannot predict initiation of damage. Work by Zhang *et al.* [112] and Kashtalyan and Soutis [113] has shown that measured damage parameters in laminates, such as matrix crack density and delamination area can be used in conjunction with material parameters and ply orientation angle to develop models for prediction of SERR for crack growth. Quantitative and qualitative experimental observations made using SRCT images is well suited to this modelling approach, with the ability to provide information on these damage parameters for comparison with model predictions.

2.4.3 Cohesive zone models

Perhaps the earliest example of a cohesive zone is the strip yield model conceived by Dugdale and Barenblatt [15, 16]. The basic premise of a CZM is that an interface is placed within a region of a continuous solid. The behaviour of the interface element is dictated by a cohesive law that is defined by characteristic traction-separation relations [106]. The cohesive law can take many forms but is generally classed as one of 4 types: linear, bilinear, trapezoidal, or exponential. In the latter three cases the behaviour is described by an increasing traction with increasing separation until a maximum cohesive strength is reached. This is followed by a decrease in traction with further increasing separation (softening), until the traction approaches zero at the displacement corresponding to total de-cohesion of the interface element. The choice of CZM selection depends on the problem to be modelled [114]. The ratio between the interface toughness and the stiffness of the bulk material has been shown to determine the degree to which the shape of the softening curve is important. For the double cantilever beam test, results show very little variation between the different cohesive law shapes. For very rigid compact specimen tests, a variation of up to 15% was detected. In general, the trapezoidal law provides the worst performance in terms of numerical stability and convergence to the exact solution, the exponential law provided the most accurate predictions, while the bi-linear was deemed to represent the most effective compromise between the accuracy of predictions and computational cost. Advantages of a CZM are evident in their application to finite element analysis. Fracture mechanics requires that an initial crack is present in a model. In a CZM, if cohesive elements can be placed along a pre-defined crack path, the cohesive law for these elements will govern the initiation and propagation of a crack. In order to have useful predictive capability, however, the cohesive law for a particular element must first be calibrated for the particular material system and response of the laminate. Cox and Yang have demonstrated the application of cohesive law models to composite damage [17], and through a collaborative proposal with Teledyne Scientific the SRCT technique provides an opportunity to apply a data rich mechanics approach to calibrate the parameters that define the cohesive element behaviour.

2.4.4 Virtual crack closure technique

The virtual crack closure technique (VCCT) is a method implemented in a finite element model to determine the strain energy release rate, G, at a crack tip [115,116]. The technique is related to the more intuitive ‘two step crack closure method’ which is derived from Irwin’s crack closure integral [117] and assumes that the energy required to close a crack by a length, Δa, is identical to the energy required to grow the crack by the same Δa. Two analysis steps are required and the crack is physically closed by Δa between the steps. For the 2-D elements shown in Figure 2.5 the energy, ΔE, required to grow the crack between the steps (equivalent to SERR) is calculated using

$$\Delta E = \frac{1}{2}\left[X_{1l} \cdot \Delta u_{2l} \ + \ Z_{1l} \cdot \Delta w_{2l}\right] \ , \tag{2.6}$$

where X_{1L} and Z_{1L} refer to the sliding and opening force acting to close the crack at a point close to the crack tip in analysis step 1. Δu_{2L} and Δw_{2L} refer to the sliding and opening displacement at the same point close to the crack tip in analysis step 2.

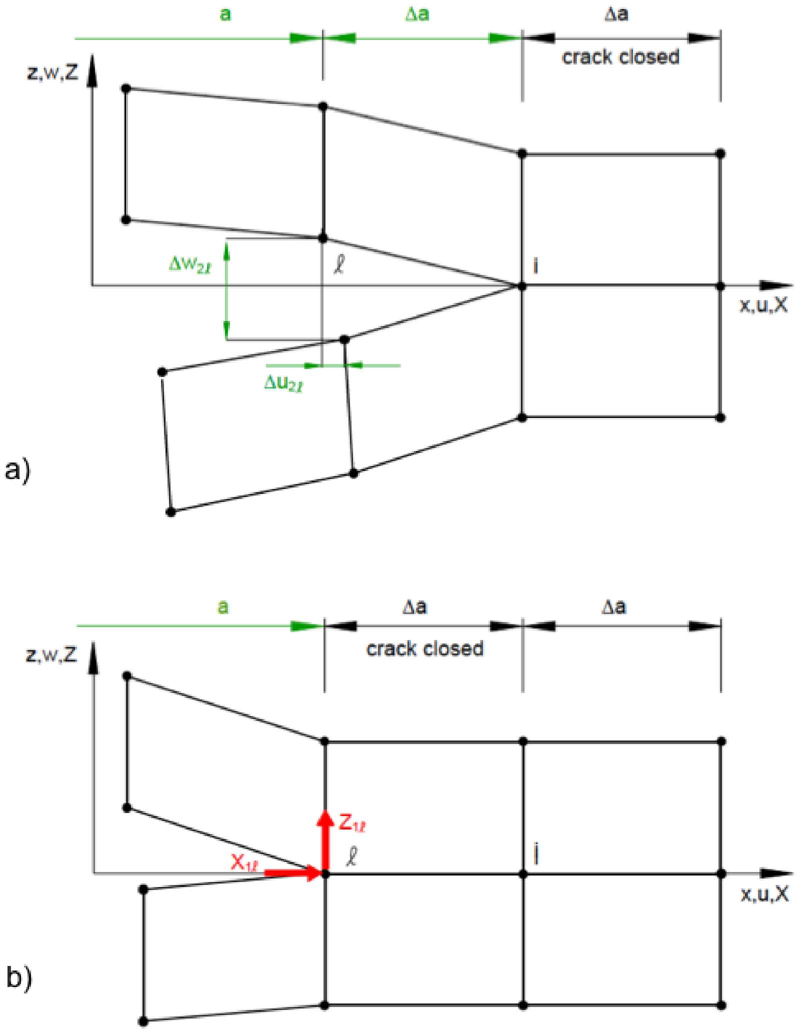

Figure 2.5: Illustration of the two step crack closure method used to calculate the energy required to grow a crack. (a) Step 1 – crack closed, (b) step 2 – crack extended. [115]

The ‘modified-’, or ‘virtual-’ crack closure method assumes that the change in crack length does not significantly change the conditions close to the crack tip. This assumption enables the calculation of energy required to grow the crack to be carried out in a single analysis step since the displacements behind the crack tip in step 1 are the same as the displacements behind the crack tip in step 2 and equation (2.6) becomes:

$$\Delta E = \frac{1}{2}\left[X_i \cdot \Delta u_l \; + \; Z_i \cdot \Delta w_l\right] \, . \tag{2.7}$$

The following describes the application of the virtual crack closure method as a technique to extract mode specific SERR at the crack tip in a 3-D model with 20-node hexahedral elements. The crack of length, a, is represented as a three-dimensional surface discontinuity by a line of nodes as shown in Figure 2.6. In the unloaded, undeformed state, nodes at the top surface and the bottom surface of the discontinuity occupy the same coordinates, however they are duplicate nodes and not connected. As such the elements attached to the top surface of the crack are able to deform independently with respect to those connected to the lower surface in the wake of the crack tip. The material ahead of the crack tip and the crack tip itself is intact and modeled using single, non-duplicated nodes.

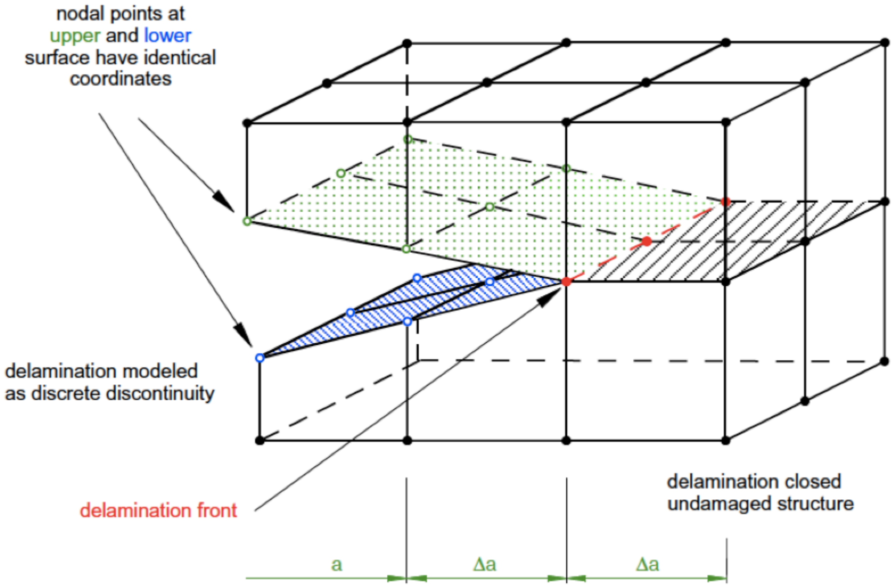

Figure 2.6: Delamination modelled with three-dimensional hexahedral elements [115].

The modal components of SERR at the mid-side node on the crack front at location M_i, as shown in Figure 2.7 are calculated as

$$G_I = -\frac{1}{2\Delta A_M}\left[+\frac{1}{2}Z_{Li}\big(w_{Ll} - w_{Ll^*}\big) + \frac{1}{2}Z_{Lj}\big(w_{Lm} - w_{Lm^*}\big) + Z_{Mi}\big(w_{Ml} - w_{Ml^*}\big)\right.$$
$$\left. + \frac{1}{2}Z_{Ni}\big(w_{Nl} - w_{Nl^*}\big) + \frac{1}{2}Z_{Nj}\big(w_{Nm} - w_{Nm^*}\big)\right] \tag{2.8}$$

$$G_{II} = -\frac{1}{2\Delta A_M}\left[+\frac{1}{2}X_{Li}\big(u_{Ll} - u_{Ll^*}\big) + \frac{1}{2}X_{Lj}\big(u_{Lm} - u_{Lm^*}\big) + X_{Mi}\big(u_{Ml} - u_{Ml^*}\big)\right.$$
$$\left. + \frac{1}{2}X_{Ni}\big(u_{Nl} - u_{Nl^*}\big) + \frac{1}{2}X_{Nj}\big(u_{Nm} - u_{Nm^*}\big)\right] \tag{2.9}$$

$$G_{III} = -\frac{1}{2\Delta A_M}\left[+\frac{1}{2}Y_{Li}\big(v_{Ll} - v_{Ll^*}\big) + \frac{1}{2}Y_{Lj}\big(v_{Lm} - v_{Lm^*}\big) + Y_{Mi}\big(v_{Ml} - v_{Ml^*}\big)\right.$$
$$\left. + \frac{1}{2}Y_{Ni}\big(v_{Nl} - v_{Nl^*}\big) + \frac{1}{2}Y_{Nj}\big(v_{Nm} - v_{Nm^*}\big)\right], \tag{2.10}$$

where: $\Delta A_M = \Delta a \cdot b$; the upper case prefix symbols, X, Y, Z represent the components of force acting at the delamination front to close the crack; and lower case symbols u, v, w represent the displacements in the corresponding directions. Column and row notation is used to denote the particular nodes for which the contributing SERR is calculated. For example, Z_{Li} represents the mode I opening component of force at the node located at column, L, and row, i. One further notation is required to differentiate between the upper and lower surfaces of the delamination. The components of displacement for the lower surface at node location, Ml, are denoted by u_{Ml}, v_{Ml} and w_{Ml}, while the upper surface displacements are denoted as u_{Ml^*}, v_{Ml^*} and w_{Ml^*}. A factor of 1/2 is required for the forces at nodes that share element boundaries since one half of the forces at nodes, L_i and L_j, act to close the adjacent crack area, ΔA_K, and half of the forces at nodes, N_i and N_j, act to close area, ΔA_O. Similar expressions can be defined for SERR at the corner nodes, C_i, and the summation of the separate components of G_I for the total area along a delamination front that contains n elements leads to

$$G_I = -\frac{1}{2\Delta A}\left[\sum_{i=1}^{n}\Big[Z_{C_i}\big(w_{C_i} - w_{C_i*}\big) \;+\; Z_{M_i}\big(w_{M_i} - w_{M_i^*}\big)\Big]\right]. \tag{2.11}$$

Expressions for G_{II} and G_{III} can be obtained by substitution of the forces, Z, and displacements, w, for the corresponding values for X, Y and u, v respectively.

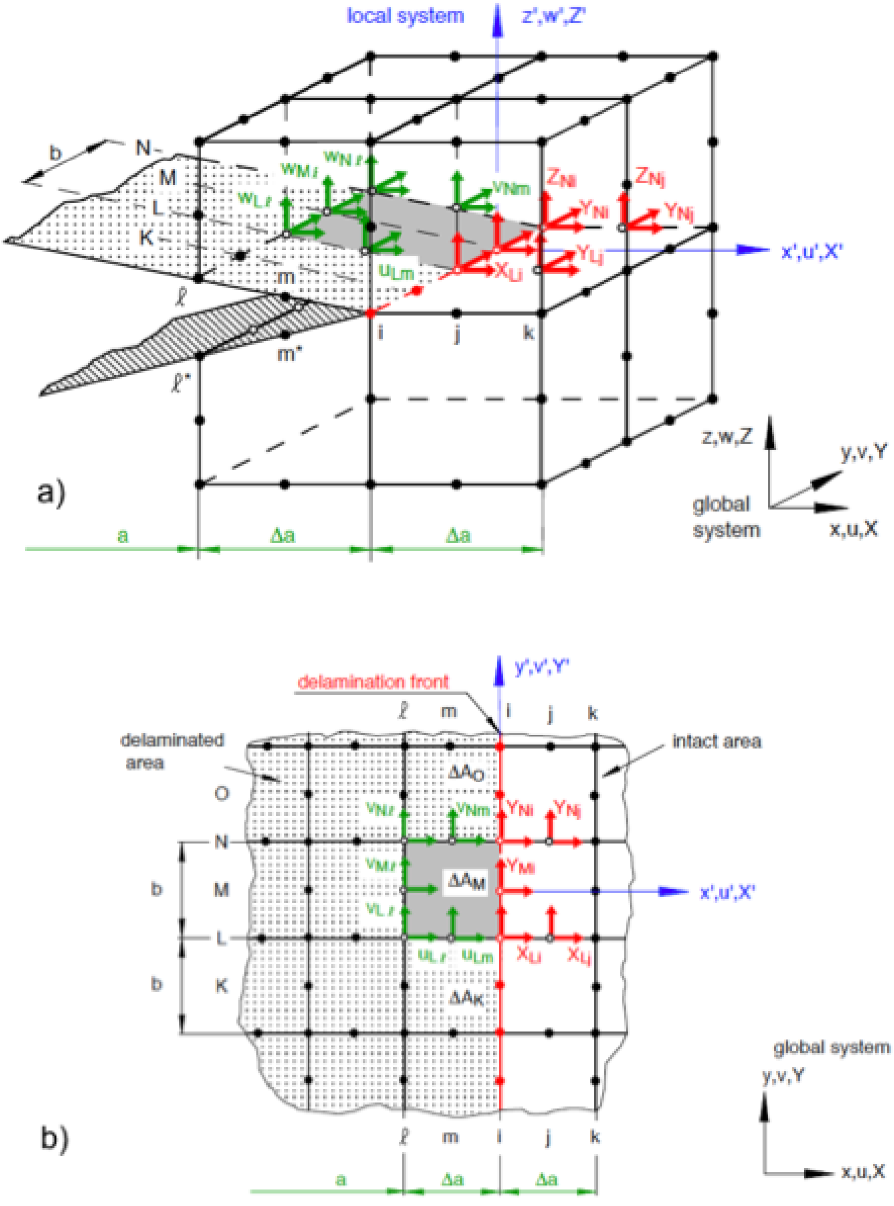

Figure 2.7: VCCT applied to an individual element along a delamination front. (a) Three-dimensional view, (b) force and displacement vectors at element nodes (lower surface not shown for clarity). [115]

The virtual crack closure technique is more readily implemented within FE code compared to cohesive zone models, and can be compared directly with experimental measurement of COD and CSD, however the technique requires the existence of an initial crack length. Cohesive zone models, on the other hand, can cope well with crack initiation, however cannot easily be calibrated according to the required parameters in order to provide meaningful predictions.

2.4.5 Concluding remarks

The following chapters describe the results from SRCT experiments that have enabled the observation, visualisation and measurement of damage initiation, growth and interaction in laminated CFRP composites. A finite element model is constructed to simulate 0° ply cracks using observed damage states in the SRCT images at a range of loads. The extraction of quantitative data from SRCT results is used to compare the performance of the model, in which crack opening displacement, crack sliding displacement and SERR is predicted. The effect of particular features such as matrix toughening and crack front pinning on damage growth in a laminate is discussed and the effect of these features on model predictions is investigated. Recommendations for future work to support and extend the results described in this thesis are provided, with particular reference to further experimental scope, model development and data reduction for SRCT imaging.

CHAPTER 3

EXPERIMENTAL METHODS

The experimental techniques employed for this work and the associated results form the basis of a powerful capacity to validate or calibrate models according to a variety of quantitatively observed and measured parameters. SRCT provides an unprecedented level of three-dimensional spatial resolution for analysis of through-thickness composite damage, and the data extracted from the images supports a platform for a ‘data-rich mechanics’ approach for comparison with model predictions. The particular focus of the experimental program was subject to the evolution of the project as the results revealed potential for a number of avenues of research. Much of the underlying methodology is common throughout this work, however, and is therefore presented as a separate chapter here.

The following sections describe the isolated stages of the experimental work carried out. Section 3.1 discusses the practical operation of benchtop microfocus computed tomography and synchrotron radiation computed tomography. Section 3.2 describes the various material systems that were manufactured and the specimen preparation process. Section 3.3 contains the method and results for strength tests to determine the failure strength of the specimens. Section 3.4 describes the design for a bespoke loading rig to enable in-situ SRCT data acquisition. Section 3.5 describes the development and rationale of the experimental program and outlines the intended outcome of the results.

3.1 Microfocus X-ray and synchrotron radiation computed tomography

Chapter 2.3 within the literature review describes the theory and principles of operation for microfocus CT and SRCT. This section is concerned with the details of the application of the techniques specific to this work.

3.1.1 Microfocus computed tomography

Microfocus CT took place at the μ-VIS facility at the University of Southampton using the X-TEK Benchtop CT 160 xi [118]. This system has an upper resolution bound at approximately 5 μm, dictated by the X-ray beam spot size. With a CCD detector of 1024 x 1024 pixels the minimum sample size correlates to a maximum cross-section length scale of 5 mm with further reduction in size bringing no benefit in image resolution. The experiment chamber can accommodate samples up to approximately 250 mm in axial cross-section, however an increase in sample size will be translated to a reduction in image resolution.

The imaging work using microfocus CT was carried out to reproduce previous observations [31] and to gain familiarity with the technique and principles of tomography. Specimens containing damage were scanned with X-ray generation conditions selected according to specimen material and geometry to achieve optimum transmission through the specimen without detector pixel saturation. The image stack output was reconstructed using commercial software, CT Pro™ [119] with visualization, analysis and rendering of the reconstructed volume using VG StudioMax™ [120]. Static tests were performed in which laminate specimens were loaded prior to CT imaging. Cracks and delaminations introduced during the application of load would close again when the load was removed, resulting in difficulty determining with confidence the crack profile, in particular the location of the crack tip. For this reason a dye penetrant with a zinc iodide base was used as a contrasting agent. The specimens were loaded and subsequently soaked in the penetrant for at least two hours, after which CT imaging readily revealed the cracks and delaminations.

In order to identify individual damage mechanisms within the laminate specimens and to obtain experimental results at sufficient resolution for higher order comparison with models, synchrotron radiation computed tomography was used. The zinc iodide was not required during SRT to resolve damage and unless stated, all images and results presented here were obtained without the presence of zinc iodide in the specimens.

3.1.2 Synchrotron radiation computed tomography

SRCT imaging took place at the ID19 beamline at the European Synchrotron Radiation Facility (ESRF) in Grenoble, France. The experiment procedure for SRCT is similar to that of microfocus CT, with an incident beam focused at a sample, transmission through the sample, and attenuated radiation collected by a CCD camera. Particular differences include the control of the equipment and the set-up parameters specific to optimal imaging conditions. The X-ray beam energy was 20 keV for all experiments and imaging conditions were set for both absorption and phase contrast. The specimens were positioned using a precision movement stage, with a sample-detector distance of 37 mm for phase contrast in the edge-detection regime. A 14 bit fast read-out, low noise (FReLoN) detector was attached to a 2048 x 2048 pixel CCD camera to achieve an isotropic voxel size of 0.7 μm or 1.4 μm using this system according to the imaging optics used. For initial experiment sets 1000 radiographs were collected through the 180° rotation for each reconstructed volume. The exposure time for each radiograph was 50 ms, which resulted in scan times of less than 4 minutes. Subsequent analysis showed that there was no damage from exposure to the high flux radiation and the number of radiographs was increased to 1500 to reduce averaging effects and improve image quality. The radiographs were reconstructed using ESRF in-house software and the resultant volume was output as a collection of up to 8 sub-volumes of 2048 x 2048 x 256 voxels, which were then aligned and recombined using the public domain software ImageJ™ [121] to create a single volume containing the original region of interest. The images shown in later sections were produced using the commercially available software, Amira™ [122], and VolumeGraphics Studio™. Post-processing routines were developed using MATLAB™ [123] and ImageJ™.

A schematic representation of the principal differences between the two techniques is shown in Figure 3.1. The specimen under test in each schematic is contained within a load frame described in Section 3.4 and located in the path of the X-ray beam. The load frame is included in the diagram for microfocus CT for comparison with SRCT of specimen location only; no *in situ* loading was carried out for microfocus CT experiments.

3.2 Specimen preparation

The complete body of experimental work described in this thesis consists of three individual sets. The method of preparation for the specimens in each experiment set is described below.

Set 1

Laminate plates from previous work [32] with a $[90/+45/\text{-}45/\bar{0}]_S$ lay-up configuration were prepared using Ciba Geigy's Fibredux 914C/T300 carbon fibre-epoxy composite system. The fibre diameter was 7 μm with a fibre volume fraction of 60% in a ply with thickness of 125 μm. The laminate with a cured thickness of 0.85 mm was cut to dimensions 24 mm x 250 mm with a guillotine. Two central holes were drilled and connected with a fine diamond coated hacksaw blade to create two semicircular notch-tips 8.5 mm apart (Figure 3.2a). Specimens were loaded according to the program described in Section 3.5. To achieve a voxel resolution of 0.7 μm in the SRCT imaging of damage at the notch tip, the laminates were sectioned around the notched region using a diamond-coated, low speed circular saw to extract thin 'matchstick' specimens of 1 x 0.85 x 20 mm (Figures 3.2b, 3.2c). The specimens were determined to be free from machining damage through microfocus CT analysis.

Set 2

Laminated plates of Hexcel HexPly® M21 carbon fibre pre-preg were laid up in a $[90/0]_S$ configuration with dimensions 300 x 300 x 1 mm and cured in an autoclave to the manufacturer's specifications at a single dwell temperature of 180 °C [124]. While the cure process will initiate before this temperature with the accompanying onset of residual thermal stress, this value is considered to represent an upper bound estimate of temperature for the stress free reference state. Double edge notched (DEN) specimens

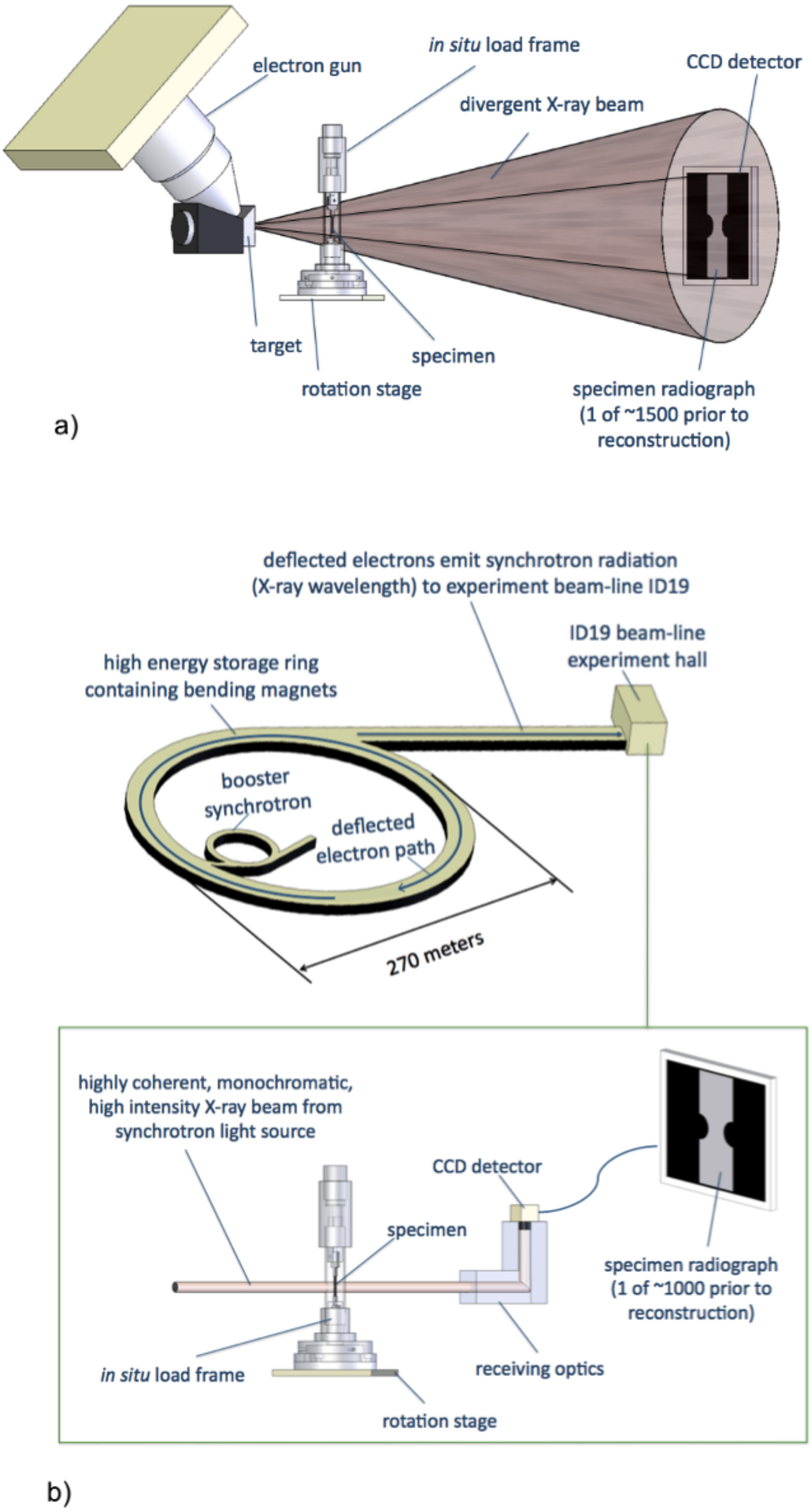

Figure 3.1: Schematics of the operation of computed tomography. (a) Divergent cone beam micro-focus X-ray CT and (b) generation of a high intensity, low divergence synchrotron X-ray beam at the European Synchrotron Radiation Facility showing SRCT experiment set-up.

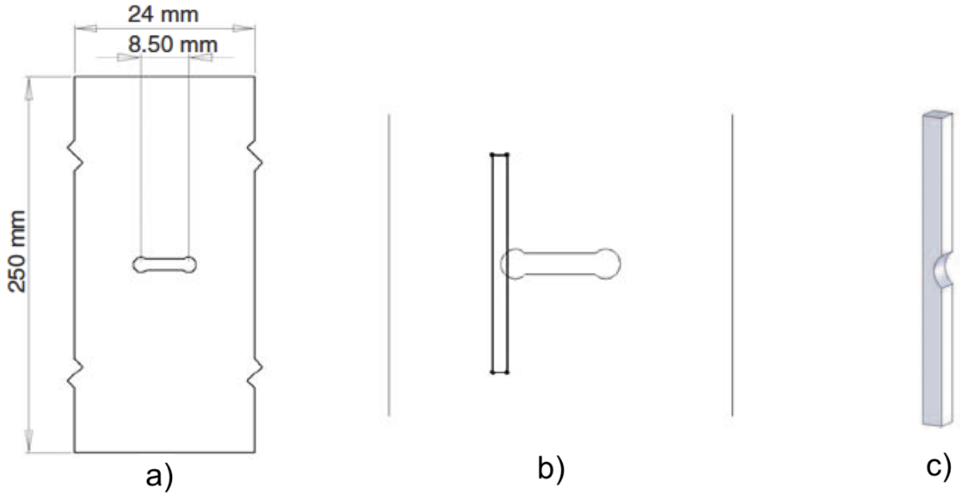

Figure 3.2: Experiment set 1 specimen geometry. (a) Schematic of laminate coupon; (b) region of sectioned laminate; (c) sectioned matchstick specimen.

that varied in size from a width of 4 mm to 25 mm were machined from the plates using an abrasive waterjet. Each specimen has similar geometry with a specified notch to width ratio of $2a/w = 0.5$ with the measured notch to width ratio after machining is contained within Table 3.1. 1 mm x 1 mm, straight-sided test specimens were sectioned from a laminate plate using the same method as described for experiment set 1. A comprehensive analysis of tomographic images of the specimens prior to loading showed that no observed damage occurred as a result of either machining processes and that all of the damage reported in this work was a direct result of the applied loading.

In order to load the 4 mm and 1 mm specimens during the tests a screw driven load frame was designed which is described in Section 3.4. Aluminium tabs shown in Figure 3.3 were produced using electric discharge machining and were bonded to the laminates to allow load transfer in the load frame. The jig shown in Figure 3.5 was used to ensure the tabs were bonded with consistency and were aligned accurately with the specimen loading direction. The 4 mm specimens produced for the SRCT tests are shown in Figure 3.4. Figures 3.4a and 3.4b illustrate the dimensions of the laminate specimen geometry and a schematic of a tabbed specimen is shown in Figure 3.4c. The geometry of the specimen was based on constraints of the load frame and on standard tensile test practice. The load frame must be contained within the stage envelope of the SRCT imaging equipment, imposing a maximum width and length on the specimen. The length of tab was selected based on the adhesive bond area required to transfer a force of 2 kN to the specimens. The maximum length was chosen for the specimen, such that the notched area was located at a distance of more than four times the notched width from the tabbed grips. The width of the specimen was chosen to enable SRCT imaging with a voxel resolution of 0.7 μm.

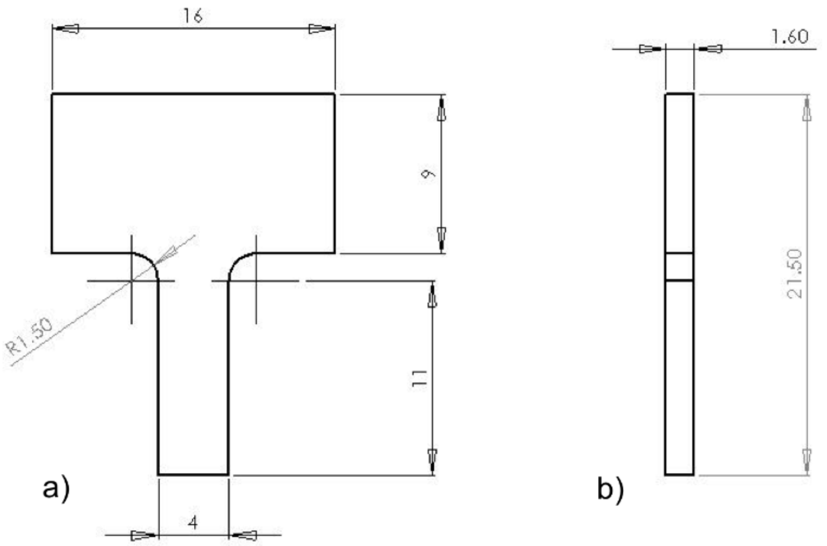

Figure 3.3: Bonded specimen tabs for *in situ* loading. (a) Front view of coupon tab; (b) side view of coupon tab.

Some of the 4 mm specimen notches were extended with a narrow slit introduced at the tip of the original notches using the low speed saw. This served two purposes: to

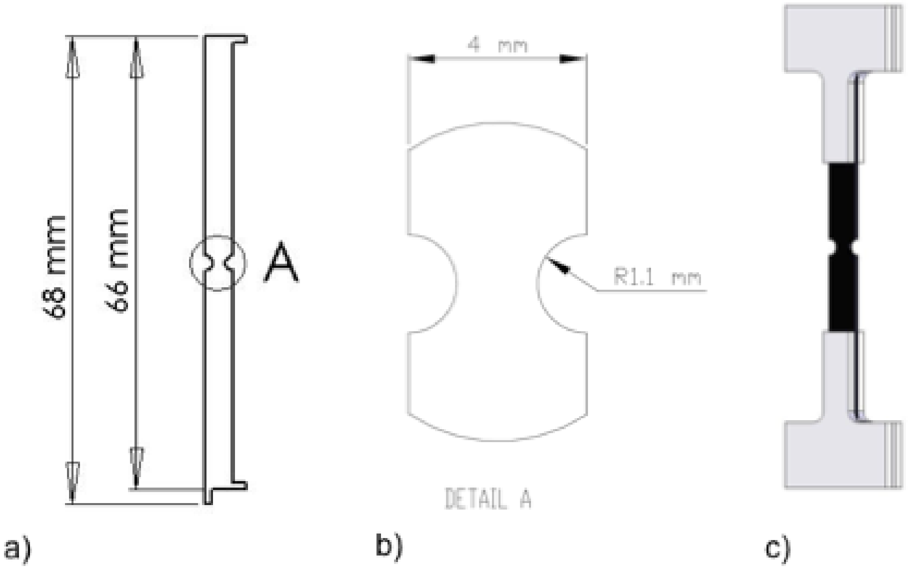

Figure 3.4: Experiment set 2 specimen geometry. (a) Geometry of composite specimens; (b) detail of notch section of specimens; (c) illustration of specimen with bonded aluminium tabs.

reduce the load required to achieve the terminal damage state (TDS) in the event that the load frame or aluminium tabs did not perform as designed; and to ensure that the damage would be guaranteed to be within the imaging field of view if the progression of damage occurred at a greater rate compared with material tested previously. The epoxy glue used was Devcon Devweld 531, whose selection was based on material properties of high strength, appropriate working time and time to full cure.

The alignment jig consists of a base plate in which dowels are located with each dowel separated by a clearance of 4 mm in width to accommodate the specimen. The side plates press the tabs against the dowels, which also align the tabs and ensure that all corresponding edges are parallel. The surfaces to be bonded on the tabs and the laminate were abraded and cleaned to produce a good keying surface. Epoxy was applied to the laminate along the bond line and placed between the set of four tabs. The radius of each tab was located against the dowels on the base plate to ensure that the tabs were aligned accurately. The top plate was used as a press to ensure good contact over the bond area. The process was repeated at each station on the jig and left for 30 minutes until sufficient cure allowed the epoxy to be handled. The specimens were then removed and left for a further 24 hours until full cure had occurred. The alignment jig was coated in several layers of Freekote release agent to promote separation of the specimens post cure. The 10 mm and 25 mm specimens were too large for high resolution SRCT in an intact state, therefore coupons were loaded prior to the ESRF session as described in Section 3.5 and subsequently sectioned as described above to extract a 1 mm x 1 mm matchstick that contained the damage. Although SRCT reconstructions showed damage profiles similar in type and appearance to the 4 mm specimens, indications of minor machining damage was also evident.

Set 3

Analysis of the SRCT volumes of experiment set 2 showed that local microstructural features had a significant effect on damage initiation and crack morphology. To investigate this phenomenon in greater detail, four material systems were used in this experiment set. In addition, a principal aim of this work was to develop comprehensive data sets of composite damage growth for public reference in recognition of the recommendations of the worldwide failure exercise. To this end seven layup configurations of $[90/0]_S$, $[0/90]_S$, $[90/0/90]_T$, $[90/+45/-45/0]_S$, $[90/0]_{2S}$, $[0/90]_{2S}$ and

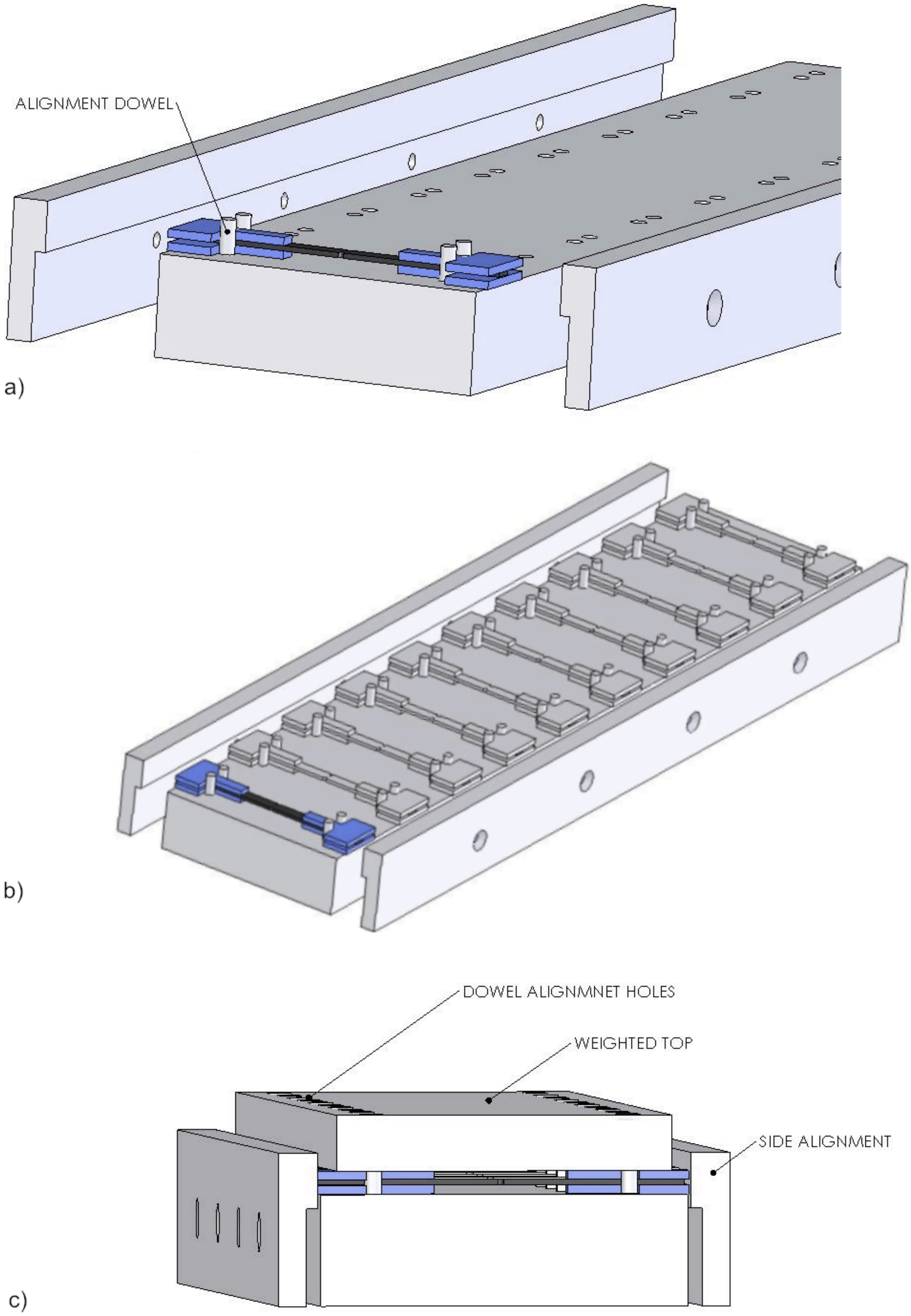

Figure 3.5: Schematic of jig used to align specimens for tab bonding. (a) Positioning of tabs on alignment jig; (b) batch processing; (c) completed batch.

$[90/\text{-}45/\text{+}45/0]_S$ were prepared from the material systems in order to observe the evolution of composite damage for various laminate stacking sequences and to obtain quantitative experimental data sets to test against model predictions. Notched and un-notched geometries were included in the experiments. Notched specimens had a maximum width of 4 mm and a nominal notched net section width of 1 mm. While abrasive waterjet machining enables intricate specimen geometry with no observed machining damage, it is not a precise tool, with tolerances yielding specimens with a maximum deviation of 0.3 mm. The un-notched specimens were straight-sided, with a width of 1 mm. A summary of the specimens prepared for the experiment set is provided with the measured strength of each specimen type in Table 3.1.

As damage propagates within the laminate the stress distributions within each ply will change according to the ply orientation and the type of damage (matrix cracking, delaminations and fibre breaks). A further aim of this experiment set was to determine full field *in situ* strain profiles using feature tracking and image correlation. To enable this for a selection of the composite specimens, aluminium particles with an average diameter of 3.5 to 4.5 μm were distributed across the surface of the pre-preg plies during lay up prior to curing. As the laminates were cured at 180 ℃ the epoxy resin containing the particles flowed through a small displacement through the thickness of each ply. The experimental hypothesis is that under load the particles will undergo a displacement from which the local 3-D strain field can be calculated. A comparison of strength and damage growth was carried out between coupons with and without particles to confirm that there was no discernable effect from the presence of particles on the mechanical properties of the laminate. The specimens were prepared for SRCT imaging at ESRF as per experiment set 2 described above with the exception of the 1 mm specimens. The bond area was found to be too small to allow the specimens to be loaded to failure in experiment set 2, and the bond between the tab and specimen failed before the laminate. For this experiment set, 4 mm specimens were prepared with the aluminium end tabs in the alignment jig to allow a load that exceeded the failure strength to be applied. These specimens were then held in a bespoke clamp and carefully machined along the exposed length (approximately 20 mm) to a symmetric width of 1 mm using a milling machine and end mill tool. SRCT inspection revealed no observed damage in unloaded specimens produced in this manner.

3.3 Strength tests

The tensile failure strength of each specimen prepared using material manufactured for this work was determined by a series of strength tests using an Instron 5569 electro-mechanical load rig with a dynamic load cell rated to 50 kN. The specimens were tested to failure and the loads at which failure occurred was measured for each material using a calibrated load cell. The failure strength was recorded as the mean value of all tests for each material/ layup system within all ESRF experiment sets. The data are summarized in Table 3.1 in which C_V is the coefficient of variation, and all remaining symbols represent their usual parameters. Large variations in the UTS were recorded for the 1 mm specimens due to the difficulty in holding the specimens in the load rig securely without inducing laminate damage. Where reference within this thesis is made to % σ_f, the value of notched UTS should be used.

Table 3.1: Summary of material strength tests for each experiment set.

Experiment	Material	Lay-up	w (mm)	t (mm)	$2a/w$	UTS^a (MPa)	C_V
Set 1	914C/T300	$[90/+45/-45/\bar{0}]_S$	24	0.88	0.35	312	–
Set 3	M21/T700GC	$[90/0]_S$	1	1.05	–	937	0.00
	M21/T700GC	$[90/0]_S$	4	1.05	0.55	918	0.03
	M21/T700GC	$[90/0]_S$	10	1.05	0.55	1133	0.01
	M21/T700GC	$[90/0]_S$	25	1.05	0.55	789	0.07
Set 3	M21/T700GC	$[90/0]_S$	1	1.05	–	1638	0.01
	M21/T700GC	$[90/0]_S$	4	1.05	0.42	1193	0.05
	M21/T700GC	$[0/90]_S$	1	1.05	–	–	–
	M21/T700GC	$[90/0/90]_T$	4	0.79	0.42	634	0.04
	M21/T700GC	$[90/+45/-45/0]_S$	4	2.2	0.39	595	0.09
	8551-7 / IM7G	$[90/0]_{2S}$	4	1.17	0.42	1231	0.04
	8551-7 / IM7G	$[90/-45/+45/0]_S$	4	1.17	0.32	819	0.07
	3501-6 / IM7G	$[90/0]_{2S}$	4	1.15	0.36	1419	0.07
	3501-6 / IM7G	$[90/-45/+45/0]_S$	4	1.12	0.32	797	0.15
	8552 / IM7G	$[90/0]_{2S}$	4	1.08	0.34	1271	0.12
	8552 / IM7G	$[90/-45/+45/0]_S$	4	1.09	0.32	693	0.09
	8551-7 / IM7G	$[0/90]_{2S}$	1	1.17	–	–	–
	3501-6 / IM7G	$[0/90]_{2S}$	1	1.15	–	–	–
	8552 / IM7G	$[0/90]_{2S}$	1	1.08	–	–	–

[a] Notched strength

3.4 Load frame

In addition to the high fidelity data that can be extracted from tomographic reconstructions, the non-destructive nature of the technique allows time resolved *in situ* loading to fully characterise the evolution of composite damage. The specimen positioning stage in the experiment hutch at ID19 is designed for high quality imaging, and little space is provided for loading devices. As such a dedicated load frame was designed and manufactured for this experiment. Figure 3.6a shows a schematic of the frame and Figure 3.6b shows the frame as an annotated section view.

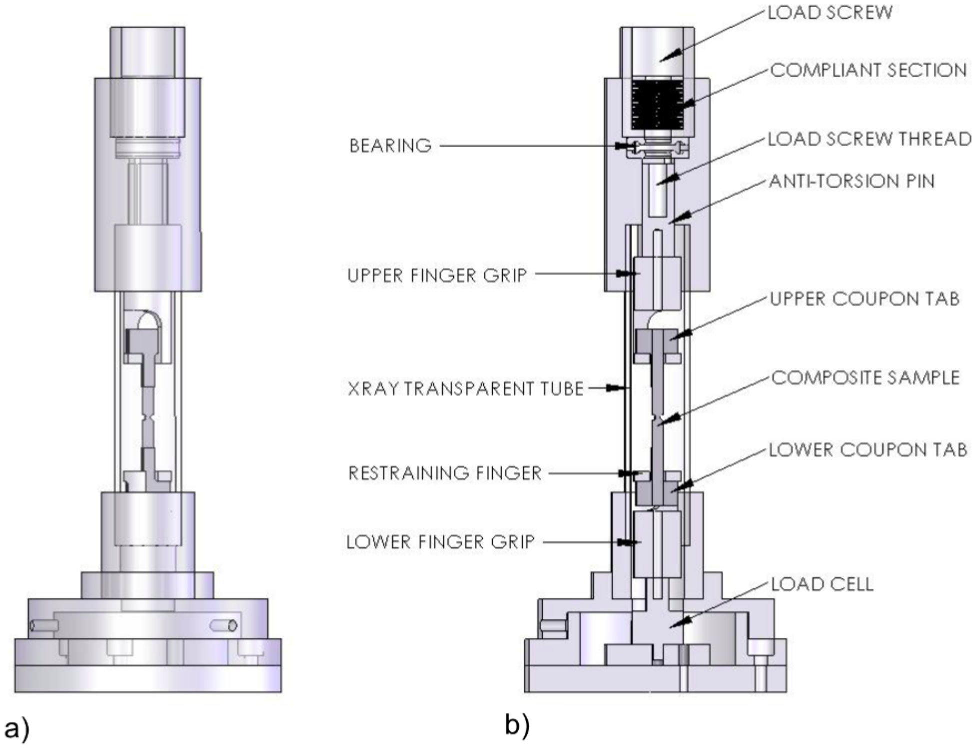

Figure 3.6: Schematic of load frame designed for *in situ* specimen loading. (a) Semi-transparent schematic of load frame; (b) annotated cross section.

The load is applied via a screw driven mechanism at the top of the frame that applies a linear displacement to the upper clevis. The tensile load is transferred to the laminate specimen through the aluminium tabs, which are restrained by fingers attached to the upper and lower clevis. The load is reacted by a transparent polycarbonate compression tube and measured using a calibrated load cell placed between the lower clevis and the stage mounting plate to form the final section of the load chain. A sliding pin whose profile prevented rotation ensured that the applied load was uni-axial. A thrust bearing beneath the screw cross-head reduced the resistance to rotation at higher loads and assisted smooth loading increments. Stress relaxation within the system was evident due to the visco-elastic properties of the compression tube. When the peak design load of 1 kN was applied to a specimen, the measured force gradually decreased to approach a lower plateau of approximately 850 N. To reduce the effect of stress relaxation, the compliant section near the top of the frame was included to improve the stability of the load with time. The section is comprised of disc springs whose number and arrangement was adjusted to maximize the stability for the maximum load. The load frame was capable of applying tensile loads in excess of 2 kN however the maximum operational load was limited to 1 kN by the calibrated range of the load cell.

3.5 Experimental program

The experiments described in this section represent the chronological acquisition of data sets and measurements used in the work reported here. Supplementary experiments that were carried out during the project and not included here have been omitted for clarity, since the results do not form part of this report. These experiments instead affect recommendations for future work and are described in Chapter 8.

Set 1

The first experiment set was carried out as an initial proof of concept during the ESRF session belonging to another group within the School of Engineering Sciences at the University to determine the ability of SRCT to identify and quantify failure mechanisms and damage propagation. Using a servo-hydraulic testing machine, the coupons were loaded in quasi-static uniaxial tension to 250 MPa (nominal remote section stress), corresponding to 80% of the average failure stress in identical coupons, as observed by Kortshot [31] and Spearing [32]. Microfocus CT was used to compare the damage observations with the results of the original work for which the specimens were initially prepared. The matchstick sections were extracted from the specimens as described in Section 3.2 and imaged using SRCT. Post-processing of the experiment data produced the results described in Chapter 4.

Set 2

The results obtained in experiment set 1 showed sub-micron resolution of damage in the laminates, allowing high fidelity observations to be made on the interactions of damage mechanisms throughout the volume of the notched region. On the basis of these results a proposal was put forward for three days of beamtime experiments at ID19 to investigate further the evolution of damage in laminated composites for a greater breadth of load cases, the size effect using specimens with a range of length scales, the notched effect using straight sided and DEN specimens, and the contribution to the damage state from thermal residual stresses. Table 3.2 summarises the tests carried out in the experiment session, classified according to the specimen size, the type of loading, applied load and the experiment purpose. Each entry in the table represents the conditions at which a scan was carried out.

1 mm specimens

The 1 mm specimens were imaged at the highest resolution conditions of $(0.7\ \mu\text{m})^3$ voxel size. The specimens were loaded according to the sequence referred to in Table 3.2, and from this point in the report as L1, which consisted of sequential load steps. Each new specimen in this sequence was scanned in the pre-loaded state with no damage, followed by subsequent SRCT imaging at incrementally increasing stresses that ranged from 30% σ_f to 90% σ_f for characterisation and analysis of damage progression from initiation to the TDS.

4 mm specimens

The first loading sequence was L1, as described above. The second loading sequence, referred to in Table 3.2, and from this point in the report as L2, consisted of an initial zero-load scan in the pre-loaded state, re-loaded to the pre-load stress value and re-scanned, and finally scanned again in the unloaded state. A comparison of the loaded state (combining mechanical load and residual thermal load) and the un-loaded state (purely residual load) allows the components of mechanical and thermal loads to be separated during post-processing analysis. A comparison of the damage state at the pre-loaded and un-loaded conditions also enables the effect of exposure to X-rays on laminate damage to be determined since no additional damage would be present from mechanical loading.

10 mm and 25 mm specimens (sectioned)

Dominant failure mechanisms in laminated composites are sensitive to changes in characteristic length scales [26]. This phenomenon has been studied extensively in the literature using a variety of assessment techniques, however to date electron microscopy is the only other common technique that provides direct image information at sub micron resolution and is restricted to a 2-D surface and subject to sectioning artefacts at the surface to be viewed. SRCT for a variety of laminate coupon length scales represents the first known full field data sets to be obtained and would offer a useful comparison for multi-scale model predictions.

Based on the extent of damage observed in the laminates in experiment set 1, the 10 mm and 25 mm specimens were loaded to 50% and 70% of their failure strength to obtain fully developed damage profiles that included all previously observed damage mechanisms. The loads were applied using a servo-hydraulic Instron 5569 prior to the ESRF session and the 1 mm x 1 mm matchsticks were extracted from the bulk specimen as described in Section 3.2.

During the experiment the preloaded sections were bonded to the aluminium tabs to be held securely in the load frame for SRCT imaging, however no additional load was applied. Post-processing of the experiment data produced the results described in Chapter 5.

Image Rastering

For loads above 50% UTS the 0° splits often extended out of the field of view of the detector. In order to capture the crack tip, after SRCT imaging captured the damage state at the notch, the precision stage was lowered in the path of the synchrotron beam and imaging was repeated. This process is referred to hereafter as rastering. The extent of splitting was greater than expected based on damage observed in previous work [31] and the experiment program was developed with the intention of a single scan per damage state. As such there was insufficient beamtime available for rastering to be carried out for all specimens in which damage length scales exceeded the field of view of a single scan and the results described in later chapters will consist of a combination of rastered and non-rastered reconstructed volumes. Where images are included in the results with non-rastering it will be for clarity of an observed damage mechanism. Extraction of quantitative data will be carried out for rastered reconstructions that contain the entire crack.

Set 3

The results obtained in experiment set 2 illustrated the sensitivity to the local microstructure of the initiation and interaction of damage mechanisms in the laminate. Limitations were also apparent within the data set, however. As described above; when compared to the length scales of damage in the literature for similar materials, the crack lengths were greater than expected and as such the crack tips of damage above 50% UTS was not often captured within the region of interest in the images. The final experiment set described here was developed with three principal aims. Experiments were designed:

i) to capture the full extent of damage in the laminates with the use of rastering;

ii) to investigate the effects of local microstructure and toughening mechanisms through the characterization of a wider range of material systems and layups;

iii) to quantify full field stress redistributions through strain mapping using feature tracking and image correlation.

Seven experiment sub-sets, outlined in Table 3.3, were prepared to fulfill each of the requirements of the experiment proposal. The details of each sub-set are described below according to the naming convention, where the prefixes *u1_* to *u8_* and *t1_* to *t9_* refer to the material system and layup and are summarized in Table 3.1. The suffixes *_e1* to *_e8* refer to the experiment sub-set method, explained in further detail below. The experiment elements of Table 3.3 are listed in order of the priority of purpose.

Experiment sub-set _e1

4 mm notched specimens were incrementally loaded from 30% to 90% σ_f to determine damage propagation and stress re-distribution. These specimens contained a sparse

distribution of aluminium particles to enable feature tracking for full field strain mapping. Specimens were also prepared without particles to characterise the damage propagation in the event that the particles had too great an effect on the composite behaviour. The material system for this sub-set was selected to provide the basis for a direct comparison of damage growth a range of lay-up configurations with constant lamina material properties.

Experiment sub-set _e2

1 mm straight-sided specimens with lay-up of $[90/0]_S$ and $[0/90]_S$ were incrementally loaded from 30% to 90% σ_f for analysis of TPCs and effect of lay-up. The post-processing and analysis for this work consists predominantly of 0° ply splits, however the analysis of other damage mechanisms, such as transverse ply cracks, would be required for complete comparisons with models.

Experiment sub-set _e3

4 mm notched specimens were imaged at loads approaching failure to capture the extent of mechanism interaction in the terminal damage state. The principal aim of the sub-set was the quantification of parameters such as crack length, extent of delamination and fibre breaks.

Experiment sub-set _e4

The same material system as sub-set *_e1* was imaged at load profiles consisting of before load, at load and un-loaded to determine the contribution from residual thermal stresses in addition to crack sliding and crack opening displacements. Separate specimens were used for each loading profile, with the values of load applied ranging from 30% to 90% UTS.

Experiment sub-set _e5

The stepwise load/ unload profile of experiment sub-set *_e4* was applied to the material system in sub-set *_e2* to determine residual stresses and displacements for TPCs.

Experiment sub-set _ e6

Material provided by Teledyne Scientific Company enabled an analysis of the variation in toughening mechanisms for pre-preg systems with varying material properties. Two lay-up configurations with three materials were incrementally loaded from 40% to 80% σ_f, with imaging at each load step and at a final unload step to determine damage propagation and residual stresses and displacements. A second set of scans of specimens loaded incrementally from 30% to 90% σ_f was implemented for an analysis of TPCs and the effect of lay-up in the three additional matrix systems.

Experiment sub-set _ e7

The initial proposal included this sub-set to capture the terminal damage state of the Teledyne material, however there was insufficient time to carry out the entire experiment program during this session due to accrued beam shut down time at ESRF. The primary aim for this material was to determine the variation in toughening mechanisms in toughened and non-toughened material systems. This sub-set was considered therefore to have lowest priority and was not performed.

Experiment sub-set _ e8

The failure strength, damage growth characteristics and qualitative assessment of damage mechanism interaction across a range of loads was compared in specimens manufactured with and without aluminium particles to determine their effect on mechanical properties.

Figure 3.7 shows a photograph of a component under test. Included in the image is the *in situ* load frame on the precision movement stage, a 4 mm DEN specimen with aluminium end tabs, the scintillator, radiation collector optics and camera housing. Post-processing of the experiment data produced the results described in Chapters 6 and 7.

Table 3.2: Summary of test program for experiment set 2.

Name	Size	Load Type	Applied Load (% nominal UTS)	Experiment Purpose
ct_1	1 mm	–	–	Characterize microstructure of material for features and fiducial markers to enable strain mapping.
ct_1a	4 mm	L1 *in situ*	0, 30, 40, 50, 60	Incremental loading for characterisation and analysis of damage initiation and propagation
ct_2a	4 mm	L1 *in situ*	0, 50, 60, 70, 80 ,90	Incremental loading for characterisation and analysis of damage prior to failure
ct_2b	4 mm	L2 *in situ*	(50), 0, 45, 0 (60), 0, 55, 0 (70), 0, 65, 0 (90), 0, 85, 0 (90), 0, 95, 0	Step-wise loading with an initial pre-load, with scanning at zero-load, at-load, and un-load to evaluate damage or specimen degradation due to X-ray exposure and the determination of mechanical loading and residual thermal stress contributions to the damage state
ct_3	4 mm, 1 mm 10, 1 25, 1	– – –	(50) (70) (50) (70) (50) (70)	Extraction of 1 mm matchsticks from pre-loaded specimens to characterize size effects on the evolution of damage and interaction of damage mechanisms for 3 specimen sizes
ct_4	4 10 25	– – –	(50) (70) (50) (70) (50) (70)	Pre-loaded specimens prepared for low resolution characterization of size effects on the evolution of damage and interaction of damage mechanisms for 3 specimen sizes
ct_5	1	L1 *in situ*	0, 80, 90, 95, 100, 105, 118, 127	Characterization of the damage state prior to failure in un-notched specimens

Table 3.3: Summary of test program for experiment set 3.

Name[a]	Lay-up	Size[b]	Particles[c]	Experiment Purpose
u1_e1 u6_e1 u8_e1	$[90/0]_S$ $[90/0/90]_T$ $[90/45/\text{-}45/0]_S$	4 mm 4 mm 4 mm	✓ ✓ ✓	Incrementally loaded from 30% to 90% σ_f to determine damage propagation and stress re-distribution using particles for feature tracking.
u3_e8[d]	$[90/0]_S$	4 mm		Determine effect of particles.
u1_e2 u4_e2	$[90/0]_S$ $[0/90]_S$	1 mm 1 mm	✓ ✓	Incrementally loaded for analysis of TPCs and effect of lay-up.
u1_e4 u6_e4 u8_e4	$[90/0]_S$ $[90/0/90]_T$ $[90/45/\text{-}45/0]_S$	4 mm 4 mm 4 mm	✓ ✓ ✓	Stepwise load/ unload to determine resisual stresses and crack sliding and crack opening displacements.
u1_e3	$[90/0]_S$	4 mm	✓	Load to observe final damage state.
u1_e5 u4_e5	$[90/0]_S$ $[0/90]_S$	1 mm 1 mm	✓ ✓	Stepwise load/ unload to determine resisual stresses and displacements.
t1_e6 t2_e6 t3_e6 t4_e6 t5_e6 t6_e6	$[90/0]_{2S}$ $[90/45/\text{-}45/0]_S$ $[90/0]_{2S}$ $[90/45/\text{-}45/0]_S$ $[90/0]_{2S}$ $[90/45/\text{-}45/0]_S$	4 mm 4 mm 4 mm 4 mm 4 mm 4 mm		Incrementally loaded from 40% to 80% σ_f all with unload step to determine damage propagation and residual stresses and displacements in three additional material systems with varying matrix properties.
t7_e6 t8_e6 t9_e6	$[90/0]_{2S}$ $[90/0]_{2S}$ $[90/0]_{2S}$	1 mm 1 mm 1 mm		Incrementally loaded for analysis of TPCs and effect of lay-up in three additional matrix systems.

[a] Defines material and experiment type

[b] 4 mm samples have dimensions as shown in Figure 3.4. 1 mm samples are un-notched with cross-section of 1mm^2

[c] Sparse distribution of aluminium fiducial marker particles present

[d] Experiment set _e7 not carried out

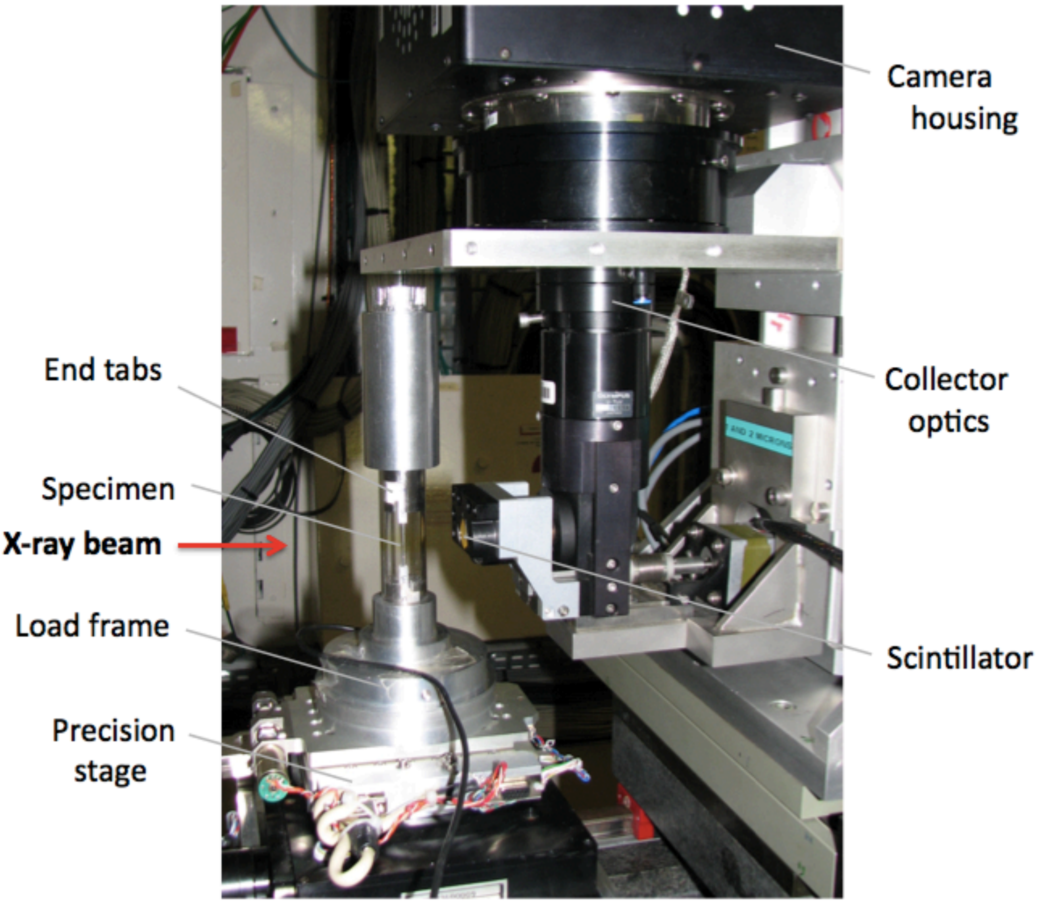

Figure 3.7: Photograph of specimen in load rig for SRCT imaging.

CHAPTER 4

HIGH RESOLUTION IMAGING OF DAMAGE IN NOTCHED CARBON FIBRE-EPOXY COMPOSITES

This chapter is based on the first journal paper to be published from work carried out during this project [125]. The conclusions towards the end of the chapter have been appended with the motivation for the subsequent work that was driven from the results in Section 4.3. The experiment details are described in Chapter 3 as experiment set 1. The rendering of images from the SRCT results were produced with assistance from Xiaowei Fu [19].

This work presents the first use of synchrotron radiation computed tomography (SRCT) to achieve sub-micron resolution of damage in aerospace grade carbon fibre-epoxy composites. The structure and interaction of the damage can be visualised in 3-D on a scale not previously observed in practical engineering configurations. The ability to detect and accurately measure features down to individual fibre breaks provides a valuable platform for future research; from the rigorous evaluation of damage models to understanding the fundamental physical mechanisms governing crack growth in composites. In particular the key role of intralaminar cracks and delaminations in localising fibre fractures is unambiguously identified for the first time.

4.1 Introduction

Damage in polymer matrix composite (PMC) laminates when loaded under uniaxial tension is comprised primarily of intralaminar and interlaminar cracking, fibre pull-out, and fibre fracture. The initiation and subsequent propagation of damage is a complex interaction of these mechanisms, however, the mechanics of their interactions are not well understood. There is also little agreement on the primary mechanism from which all other damage follows.

With the aim of determining the micro-mechanisms of damage interaction and the order of progression, this paper examines very high resolution images of the damage in a notched carbon fibre-epoxy laminate using a synchrotron radiation source for computed tomography (SRCT). 3-D images of composite damage have been obtained previously using micro-focus X-ray computed tomography (CT) [73–79] however the resolution achieved using current SRCT facilities is more than an order of magnitude greater (down to ~ 0.3 μm is readily available [72]) than that achieved in previous work. Furthermore SRCT offers the capability to resolve cracks in low density materials with significant enhancement by the use of phase contrast [63, 84]. The scale of detail that can be obtained is sufficient to identify individual fibres within a ply and crack face displacements of the order of 100 nm. To date, however, the only SRCT analysis of PMC materials known to the authors is that of Aroush *et al.* [103] who analysed fracture predictions based on stochastic models in simple uni-directionally reinforced quartz bundle-epoxy composite, using SRCT images to show fibre damage. The present paper considers the detailed 3-D structure of damage occurring in $[90/+45/-45/\overline{0}]_S$ PMCs after monotonic loading in uniaxial tension. A qualitative approach is taken to analysing the damage, paying particular attention to the interaction of intralaminar cracks, interlaminar cracks, and fibre fracture.

4.2 Results and discussion

After extensive radiographic analysis prior to loading negligible damage due to machining was observed. The damage shown in the figures below is due entirely to the applied load of 80% σ_f. Figure 4.1 is a simplified schematic of the laminate damage shown in Figure 4.2 near the notch, and is used to identify reference planes in subsequent figures. The illustration indicates fibre orientation for the plies, and illustrates the damage that is observed in each ply and at their interfaces. Figures 4.2 and 4.3 show a 3-D rendering of the segmented regions of damage and identify the interaction of the cracks, delaminations and fibre breaks. In each of the non-zero degree plies, intralaminar cracks are seen that follow the fibre direction within that ply. Extensive delamination occurs between both of the +45° and -45° plies. There are numerous broken fibres in the notch tip region in the 0° ply. Areas of delamination are only evident between the +45° and -45° plies, where the angular difference between the fibres in adjacent plies is twice that for all other interfaces. For all other plies, intralaminar cracks are arrested at the interlaminar boundary. The separation between the delaminated surfaces is also greatest where the cracks through the two plies are not aligned.

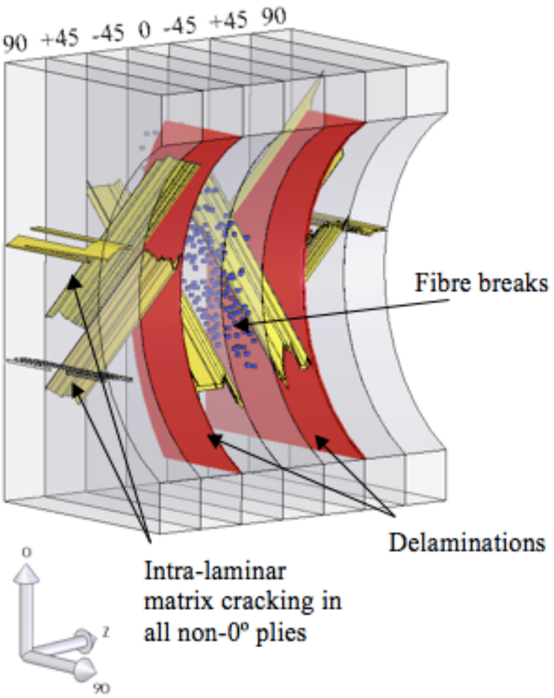

Figure 4.1: Schematic of fibre orientation and damage observed in $[90/+45/-45/\bar{0}]_S$ 914C/T300 laminates at 80% σ_f.

Figure 4.4 contains 2-D image slices, showing the distribution of damage at two distances from the notch. Phase contrast effects are clearly seen, highlighting crack locations. Both slices show the presence of fibre breaks at the points where the -45°

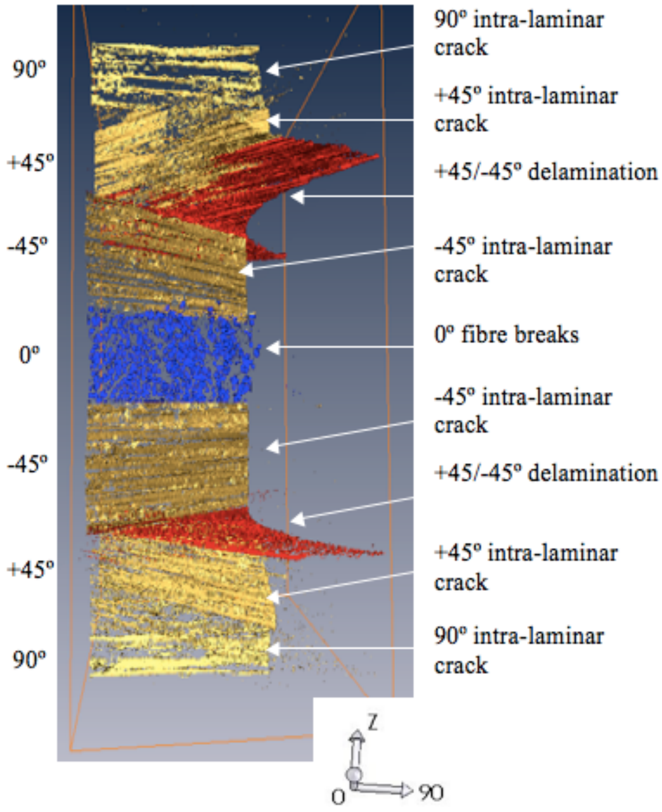

Figure 4.2: Cropped SRCT volume showing segmented cracks, delaminations and fibre breaks. Notch is to the right of the image.

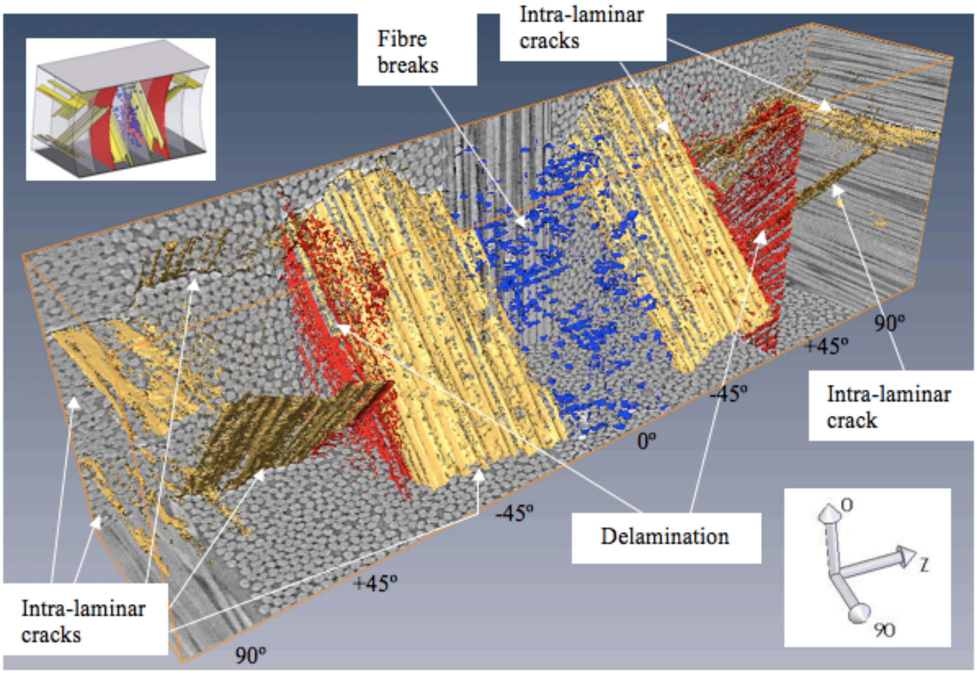

Figure 4.3: SRCT volume showing segmented cracks, delaminations and fibre breaks ahead of the notch at 80% σ_f. The segmented damage is overlaid on orthogonal SRCT slices showing the fibre orientation within each ply. The volume is cropped at the notch tip.

intralaminar cracks meets the 0° ply, consistent with the 0° fibres remaining intact until the stress redistribution ahead of the growing crack overloads the fibres. Similar observations have been made previously using deply techniques [32]; however, it has not been possible previously to assess the prevalence of such broken fibres through the 0° ply thickness. It is significant that the broken fibres at the surface closely correspond to the incidence of the intralaminar cracks, whereas those in the interior of the 0° ply are more widely distributed, indicating the statistical aspects of load sharing and fibre fracture. The paths of the intralaminar cracks follow the fibre orientations, however, the crack profiles through the thickness (z-direction) are markedly non-planar and in some cases bifurcate, particularly where they intersect with delaminations.

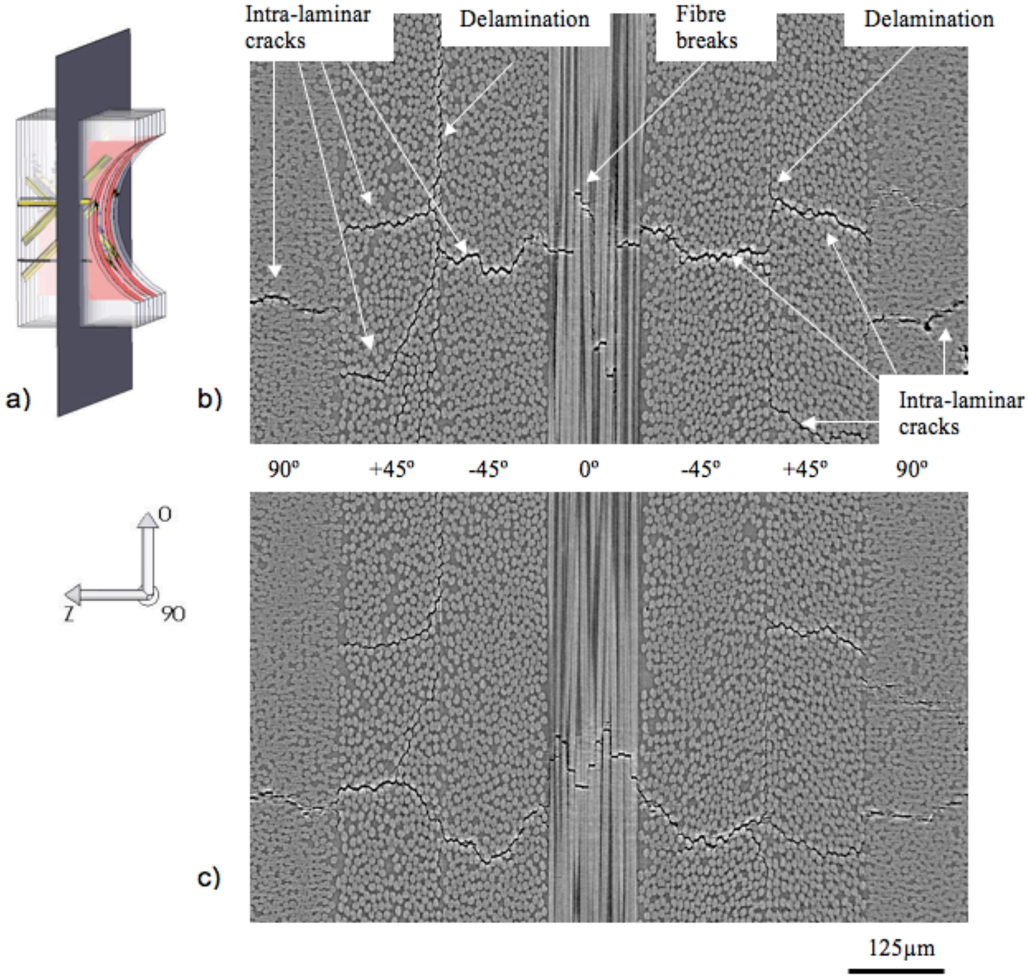

Figure 4.4: 2-D digital slices through the SRCT volume at 80% σ_f. (a) Reference plane (side) for SRCT slices; (b) 200 μm ahead of the notch; (c) 350 μm ahead of the notch.

Figure 4.5 shows the cracks and delaminations advancing ahead of the notch through the sample in the transverse (90°) direction. As with the sections shown in Figure 4.4, the 0° fibres have broken at the interfaces with the 45° plies; however, the density of breaks is greatest at the centre of the sample (b). Although the predominant damage in the 0° ply consists of fibre breaks, these are accompanied by fibre-matrix debonding and local matrix cracking as the stress field surrounding the fibres is redistributed in the wake of fibre failure. The cracks in the +45° ply can also be seen to blend into the delamination as they approach the +45°/-45° boundary.

As shown in all images, the intralaminar cracks tend to follow the orientation of the fibres within the ply; however, the propagation through the thickness is not planar. An additional interaction is clearly seen in the two interface images shown in Figure 4.6. The fibre breaks in the 0° ply cascade along the position of the intralaminar crack in the -45° ply which is tangential to the circular notch. The dominant role of these tangential intralaminar cracks in determining delamination has been previously noted [126].

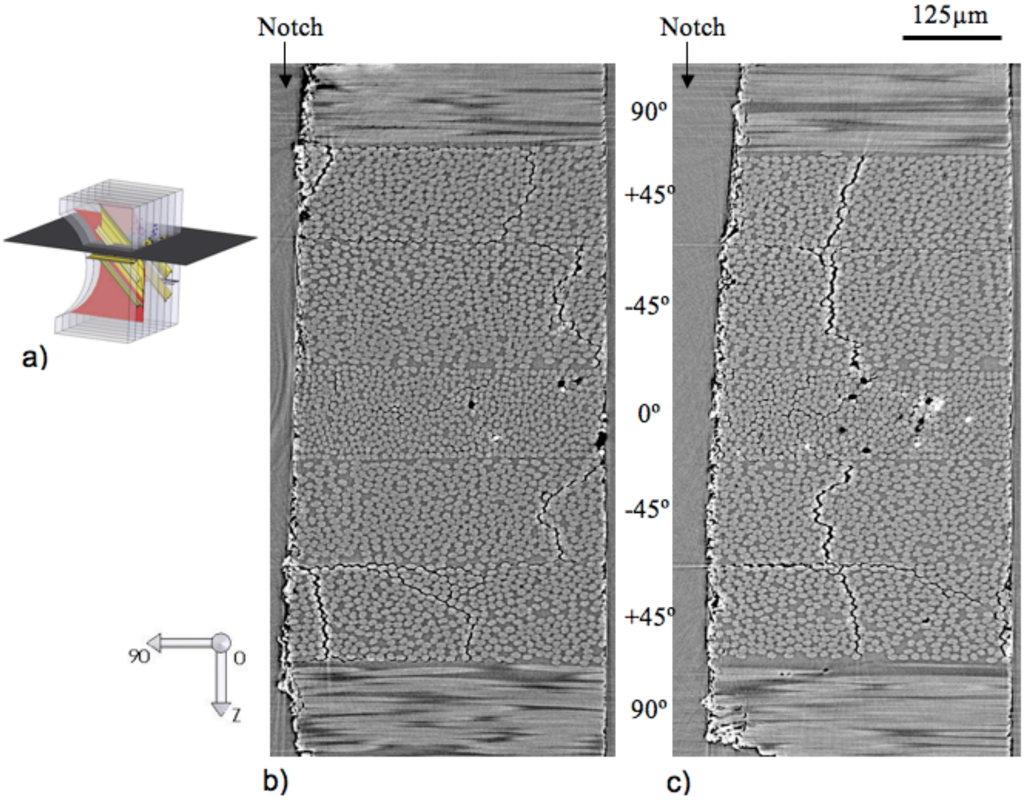

Figure 4.5: 2-D digital slices through the SRCT volume at 80% σ_f. (a) Reference plane (axial) for SRCT slice; (b) 250 μm above centre of notch; (c) Centre of notch. Notch is at left of the images.

The summary of damage observed in the notched $[90/+45/-45/\overline{0}]_S$ laminate sample in uniaxial tension is as follows:

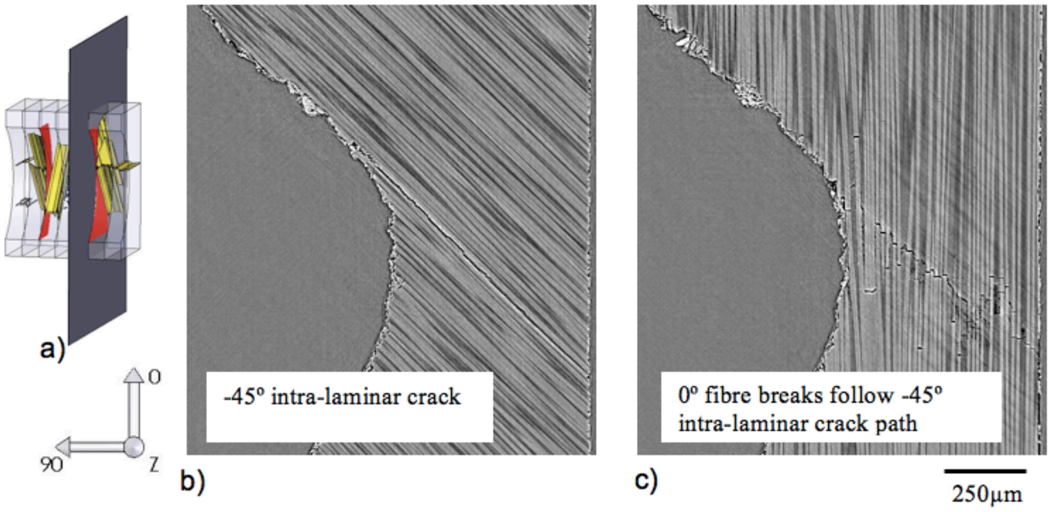

Figure 4.6: 2-D digital slices through the SRCT volume at 80% σ_f. (a) Reference plane (front) for SRCT slice; (b) 530 μm in front -45°/0° interface; (c) 530 μm behind -45°/0° interface.

- All the intralaminar cracks grow parallel to the fibre direction of that ply in which the split occurs. The profile of the cracks through the thickness is not planar.
- 90° plies contain either one large intralaminar crack that initiates close to the centre of the notch tip, or two smaller cracks either side of the notch centre.
- +45° plies contain one main split that runs tangential to the notch, accompanied by smaller cracks. Both +45°/-45° interfaces have delaminated; however, the 0/-45 and +45/90 interfaces remain intact. In one of the +45° plies, the intralaminar splits deviate from their initial path and merge into the delamination.
- Both -45° plies contain just one intralaminar crack that runs tangential to the notch.
- The majority of the damage in the 0° ply consists of fibre breaks that are predominantly positioned in the central region of the ply. At the -45°/0° interface there is a concatenated series of breaks, aligned with the split in the -45° ply. The fibre breaks are also accompanied by minor matrix cracks that interlink around the broken fibre sites.

Some important insights can be derived from these observations. First, the extent of interactions between the damage modes has rarely been so clearly illustrated. The intimate connections and synergy between the growth of intralaminar cracking, delamination, and fibre fracture is irrefutable. This has clear implications for composite damage modelling, particularly the need for models that provide for an holistic treatment of damage growth processes, rather than a decomposition into separate components. Second, the strong correlation between fibre fracture, through the thickness of the principal load bearing, 0°, plies, and intralaminar cracks suggests that such interactions must be accounted for in any mechanistic modelling of composite strength or lifetime. This correlation also suggests that in this material system the intralaminar cracks grow slightly ahead of the delamination front. If delamination preceded intralaminar cracking, then the 0° fibres would be isolated from the stress concentration due to the intralaminar cracks and would not fracture in a correlated manner. Finally, the strong influence of the tangential -45° cracks on defining the extent of delamination and 0° cracking, and the relatively weak influence of +45° and 90° cracking suggests that in configurations such as this it may be possible to develop mechanistic models with predictive capability while only modelling a subset of all the damage observed. This makes the concept of 'virtual testing' [127] tractable by reducing the computational expense incurred.

The volumes from which the images were obtained have a voxel width of 0.7 μm providing a resolution due to pure X-ray absorption of approximately 1 μm. The phase contrast fringe produced by an abrupt change in X-ray refractive index (for example the material/air interface of a crack or delamination) allows the detection of such features down to $\sim$ 0.1 μm. Although the presence of an opening of 100 nm can be determined, producing reliable results to this resolution is not straightforward and is greatly dependent on the experience of the user since the data is presented as an array of discrete gray-scale values from which meaningful information must be extracted. In the images shown here the matrix cracks are easily identified since they are held open by the residual stress distribution resulting from the thermal expansion mis-match between adjacent plies during cure. The delaminations are not as clearly defined since the opening displacements are much smaller. *In situ* SRCT, where the sample is held at load during scanning would provide a greater depth of understanding for damage evolution and interaction, at the same time providing clearer images of the three characteristic mechanisms of cracks, delaminations and fibre breaks.

4.3 Conclusions

Information obtained using reconstructed SRCT volumes allows the microstructure of polymer composite materials to be characterised on a scale not previously obtainable in non-destructive testing. Indeed, even electron microscopy, although capable of resolving greater planar surface detail, is inherently limited in through-thickness spatial resolution due to the discretised process of serial sectioning.

The images included in this report are the first of their kind as there is no literature of which the authors are aware, that maps contiguous damage in a PMC with an applied lay-up configuration. It is anticipated that the detail shown in these images will lead to a number of future research avenues. Time-resolved damage initiation and evolution obtained from *in situ* loading will establish the means to study the complex interactions of damage mechanisms that take place in composite materials. There is potential to develop microstructure level calibration for finite element models, given the ability to measure the scale and position of damage for the model inputs and boundary conditions. It will also be possible to evaluate the accuracy of existing damage models not only in terms of mechanical strength, but also for crack initiation, crack growth, and the chronological interaction of the damage mechanisms.

SRCT imaging is limited neither to monotonic uni-axial tensile loading regimes nor to polymer matrix composite laminates. The ability to obtain strain, displacement and structural information and to identify the sequence of damage in 3-D on a microscopic scale provides the opportunity to gain a deeper understanding of additional materials and areas of damage analysis. It is anticipated that valuable results could be acquired in many fields of research such as impact damage, including compression after impact (CAI) strength analysis, damage evolution in through-thickness reinforced structures (z-pinning) and fatigue mechanics.

The damage observed in the images presented here is advanced, with all dominant damage modes present as a result of high applied stress (80% σ_f). The experiment sets described in Section 3.5, in which incremental load steps were applied to a variety of material systems and stacking sequences, were developed to enable the identification, progression and interaction of damage modes. The results of these experiment sets are discussed in the following chapters.

CHAPTER 5

MODELLING NOTCH TIP DAMAGE IN A LAMINATED COMPOSITE

This chapter includes material from two further publications providing detailed observations of damage micromechanisms [128, 129] and a comparison of quantitative experimental results with predictions from a 3-D finite element model [130]. The experiment details are described in Chapter 3 as experiment set 2. Certain aspects of the theory relating to modelling techniques and to the practical application of SRCT, described in greater detail in Chapter 2, are revisited in the results section to explicitly demonstrate validity and confidence in the technique. SRCT image rendering and quantitative extraction of experimental data for sliding displacements and crack opening displacements were provided by Andrew Moffat [20].

Synchrotron radiation computed tomography (SRCT) has been used to observe *in situ* damage growth and enable micromechanical damage characterization in notched M21/T700 $[90/0]_S$ carbon fibre-epoxy composite samples, with un-notched width of 4 mm, loaded in uniaxial tension to stresses ranging from 30% to 90% of the nominal failure stress. A 3-D finite element model of the $[90/0]_S$ specimen has been constructed to predict crack opening displacements and sliding displacements in the 0° plies resulting from thermal residual stress imposed during autoclave cure and from the application of mechanical load. Of particular interest is the demonstration of SRCT as a technique to enable direct, *in situ*, 3-D, non-destructive damage quantification to assist model development and provide model validation. In addition it has been identified that SRCT has the potential for full field analysis of strain re-distributions during damage growth.

5.1 Introduction

Modelling the behaviour of composite materials is far from trivial due to the complex interactions of multiple damage mechanisms, including fibre-matrix debonding, inclusion-matrix decohesion, delamination, intralaminar cracking and fibre rupture [79, 131]. A large number of models have been able to predict successfully the strength of laminated structures for a particular lay-up configuration or loading regime [6, 132–134], however the inherent assumptions and simplifications within these models usually result in a lack of predictive capability when the material system, lay-up or type of loading is modified [10]. Many current models are only successful in their predictions due to empirical fitting to a particular data set. With its limited physical basis, the fitted model will not predict changes in failure processes (lay-up, load case). A homogenised damage mechanics approach to modelling requires an understanding of the interacting mechanisms leading to damage initiation and propagation while a micro-mechanics approach that captures the physics of fracture mechanics is computationally expensive.

This paper has two principal objectives. The primary aim is to demonstrate the potential of synchrotron radiation computed tomography (SRCT) [72] as a technique to observe the *in situ* initiation and propagation of damage in a $[90/0]_S$ carbon fibre-epoxy composite and to identify the critical damage interactions that lead to laminate failure to assist model development, calibration and validation. Particular damage parameters such as crack opening displacement (COD) and sliding displacement have been quantified and used in conjunction with high resolution images of damage evolution to inform the development of a finite element (FE) model of intralaminar matrix splitting in the 0° plies. The secondary aim is to compare a 3-D FE model with the SRCT results and to determine the extent to which the model of an observed damage mechanism of a split in a 0° ply has useful predictive capability. In addition, the data acquired from SRCT has been compiled as a library of experimental results that can be accessed for comparison with existing and future model predictions. It is acknowledged that the growth of 0° splits will be affected by the presence of transverse ply cracks, and this has been addressed in additional work by Renault *et al.* [135]. In this initial investigation, damage in the 0° plies alone in considered.

5.2 Results and discussion

5.2.1 Experimental observations

CT reconstruction allows the volume of a given sample to be visualized as a 3-D grey-scale map [125] in which the grey-scale value correlates to the local material X-ray adsorption coefficient, depending strongly on atomic number (photoelectric regime). Two distinct peaks in the histogram of gray-scale intensity represent air (cracks, splits, voids, delaminations and the area surrounding the notch boundary) and solid material (continuous, intact fibre and epoxy). By defining thresholds around the appropriate grey-scale values, material and cracks can be segmented and separated. For low-density objects, or for regions in which two separate structures have similar densities, phase contrast can be exploited to improve edge detection. Figure 5.1a shows a section of a typical reconstructed SRCT volume while Figure 5.1b and 5.1c show particular 2-D slices through the volume in which segmented intralaminar damage is identified. Figure 5.1b shows damage viewed parallel with the 0° splits and Figure 5.1c shows a view parallel with the transverse ply crack. In Figure 5.1a the volume has been partly withdrawn to the laminate centre-line to reveal one transverse ply crack in the 90° ply and two splits in the 0° ply emanating from the notch tip. In this particular material system, with a toughened epoxy matrix, delamination did not occur until a load of 70% σ_f was exceeded. In this figure the sample was loaded to 40% σ_f and as such no delaminations are present between the plies. The rough appearance of the notch is due to the abrasive water jet used to create the sample geometry and may have an effect on damage initiation.

When including samples taken to failure, three principal damage mechanisms have been observed in this work: 0° ply intralaminar splits, 90° ply transverses ply cracks and 90°/0° ply-interface delaminations. The three mechanisms initiate and interact in a complex manner. While the influence of the mechanisms and interactions are discussed, this work represents an initial analysis of the laminate damage, and since delamination does not occur in this material at loads lower than 70% σ_f quantitative analysis is restricted to intralaminar damage in the 0° ply alone.

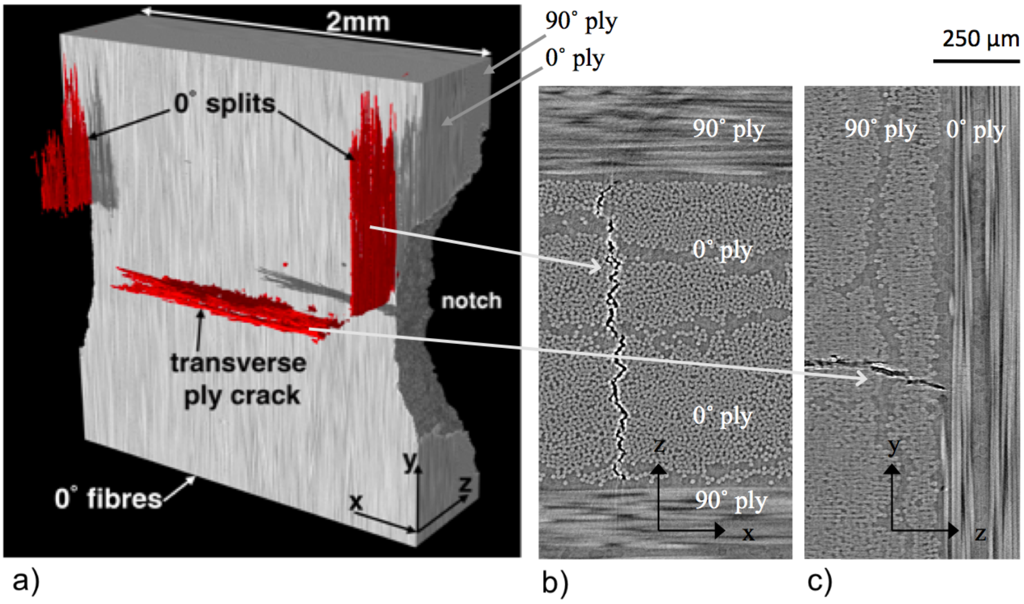

Figure 5.1: Observed damage in the notched region of the specimen. (a) Tomography image of intralaminar damage in a $[90/0]_S$ laminate at 40% σ_f. The bulk of the composite has been withdrawn to reveal the damage, comprising two 0° splits and a transverse ply crack, (b) digital 2-D slice through the SRCT volume in the X-Z plane showing the 0° splits, and (c) digital 2-D slice through the SRCT volume in the Y-Z plane showing the transverse ply crack (half laminate thickness shown). Note that no delamination is present at this load.

The damage was carefully segmented from the surrounding material using a 3-D thresholding tool within VolumeGraphics VGStudio Max™ [120]. The segmented images were manually checked to ensure accurate results.

To evaluate the interaction between damage and the composite microstructure it is informative to use 2-D sections of the CT volume. The images produced are similar to those from conventional sectioning and polishing but are not susceptible to sectioning artefacts. of the two 0° plies. The bright fringe around the split results from phase-contrast and is particularly useful for identifying the crack when it is narrow, *i.e.* near the crack tip. Whilst the laminate contains only two 0° pre-preg plies it can be seen in Figure 5.2a that there appears to be four plies and these are separated by the resin-rich regions that have been identified by circles b, c and e. This is likely to be a feature of the pre-preg manufacture process where a single pre-preg ply actually comprises two thinner plies.

The damage in the resin-rich regions is different to that in the regions where the fibres are close packed. It can be seen in Figure 5.2b, c and e (which correspond to circles b, c and e in Figure 5.2a) that in the resin-rich regions damage is in the form of small

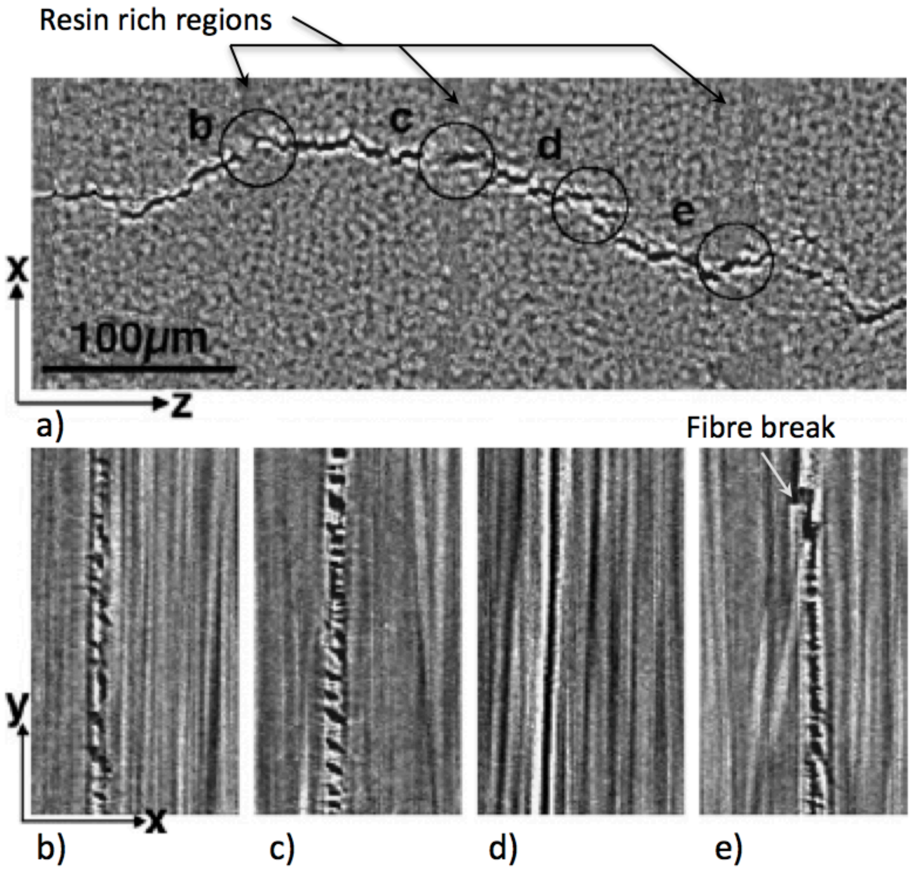

Figure 5.2: 2-D SRCT sections through a 0° split in a $[90/0]_S$ laminate. (a) Four regions have been identified: b, c and e are resin-rich regions and d is representative of a region of close packed fibres. These regions correspond to (b)-(e), which show that echelon cracks form in the resin-rich regions b, c and e.

hackles or echelon cracks at approximately 45° to the loading direction. In the fibre-rich regions the damage is smooth and is apparently associated with the debonding of the fibre/matrix interface. Higher-resolution imaging would be required to confirm this and will be the subject of future investigations. Individual fibre breaks are not common at loads less than 60% σ_f. However, they were observed occasionally and were usually associated with misaligned fibres. An example of such a fibre break can be seen towards the top of Figure 5.2e.

Closer examination of the resin-rich regions revealed the presence of rubber toughening particles, as identified in Figure 5.3. Two types of echelon cracks have been observed in the resin-rich regions. The first type are approximately 20 μm in length and are associated with the toughening particles. Under load the toughening particles are seen to debond from the surrounding epoxy matrix. Some evidence of near-complete particle decohesion has been observed, but in the 0° splits it can be seen (Figure 5.3a) that most are only partially debonded. The second type of echelon crack is smaller (<5 μm) and can be seen towards the bottom of the split in Figure 5.3a. These are usually found emanating from the edge of fibres that border resin-rich regions. Figure 5.3a and b show the same CT slice of the xy plane in a sample scanned in the unloaded and loaded (50% σ_f) states respectively. In the unloaded state the echelon cracks are not completely closed, consistent with the action of local residual stresses. In the loaded specimen it can be seen that the cracks have a greater level of opening and that shear has occurred. The material between the cracks (both epoxy matrix and toughening particles) provides bridging [136] across the split.

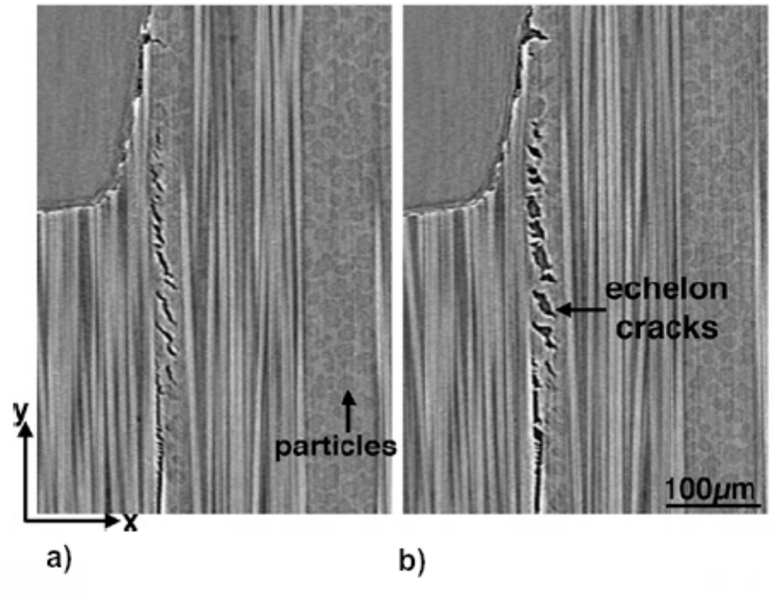

Figure 5.3: 2-D SRCT images showing the effect of loading on echelon cracks that form in the resin-rich regions in a 0° ply within a $[90/0]_S$ laminate. (a) Unloaded specimen; (b) specimen loaded at 50% σ_f.

5.2.2 Quantitative experimental results

While detailed qualitative observation and interrogation of high-resolution damage is informative, it is more desirable to obtain results that can be used to compare with models to determine predictive capability. Using features such as pores and inclusions in the composite immediately surrounding the split, in addition to features on the crack flanks themselves, it has been possible to quantify the sliding displacement associated with loading. Following the methodology of Toda *et al.* [137] it was possible to use the differences in the y direction between pairs of features in the unloaded and loaded volumes to ascertain the displacements due to loading. The method is illustrated by the schematic shown in Figure 5.4. In this diagram *notch side* refers to the area closest to the free edge of the sample, while *bulk side* refers to the area closest to the centre of the sample. The displacements are largest on the notch side of the sample where, because of the split, the constraint of movement is mostly supplied by the 90° plies and any bridging across the split. These measurements of internal crack behaviour provide input to ongoing model development and validation.

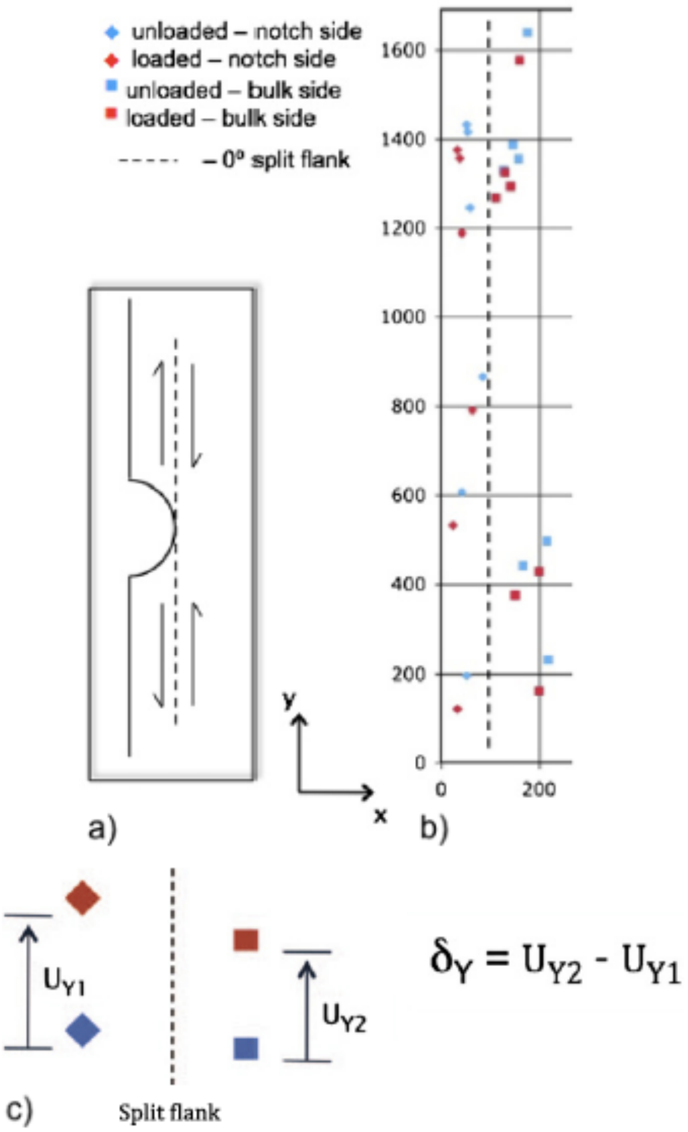

Figure 5.4: Schematic illustration of sliding displacements in the region of the notch. (a) Shear stress acting between the split flanks in the 0° plies, (b) position of microstructure features (in pixels) either side of the split identified for tracking in the loaded and unloaded stated, and (c) Schematic of definition of sliding displacement, δy.

The crack opening displacement (COD) is often used to determine the stress intensity factor (K) or the strain energy release rate (G). Experimentally COD is usually obtained using a clip gage or via optical measurements of the outer surface of the sample, depending on the specimen geometry. X-ray CT allows a more direct method of measuring the COD along both the length and the width of the crack, and so it is possible to obtain accurate, internal measurements of COD, overcoming conventional limitations. The accuracy of such measurements is dependent on the degree to which features, such as crack flanks and fiducial markers, can be detected and segmented which, in turn, is limited to the voxel size of the SRCT images. In Figure 5.1 it is shown that cracks can be segmented from the surrounding composite; as such, the COD may be measured from the segmented crack data. To analyse the cracks of interest (in this case the 0° splits), each 3-D volume was cropped into a set of smaller volumes that contained only the splits.

Observing a split perpendicular to the yz plane it is possible to see the 2-D projected profile of the crack. The extracted data is resolved in 3-D however, as the crack has a depth in direction x (opening displacement). The COD at each yz position is the sum of the voxels in the x direction. A routine was specifically written using MATLAB™ to analyse the segmented cracks and produce plots of COD (Figure 5.5a, c and e). Figure 5.5a is a COD plot for a split in a sample loaded to 40% σ_f. This plot allows for a qualitative observation of the (projected 2-D) crack shape but also gives COD information: the darker the colour, the larger the COD; the background white colour corresponds to a COD of 0 μm, *i.e.* no crack. Figure 5.5b corresponds to a CT section in the xz plane taken at 140 μm from the near notch position (due to the roughness of the notch and the resulting crack the near notch position is defined as the point at which the split and notch are clearly separate along the width of the split). Figure 5.5c and d, and e and f correspond to the same sample loaded to 50% σ_f and 60% σ_f, respectively.

At 40% σ_f (Figure 5.5a) the split consisted of two main sections from 0-170 μm and 240-360 μm in the z direction. There is a small fork of crack growth between these two regions but there are clearly regions where there is no crack. From 360 μm (in the z direction) it can also be seen that there is no split. The COD at 40% σ_f was determined to be 1-3 μm throughout the majority of the split. At 50% σ_f (5.5c) the crack has advanced and the tip is outside the field of view. However, it is clear that the crack front is not planar: in the region 170-240 μm (in the z direction) the crack front

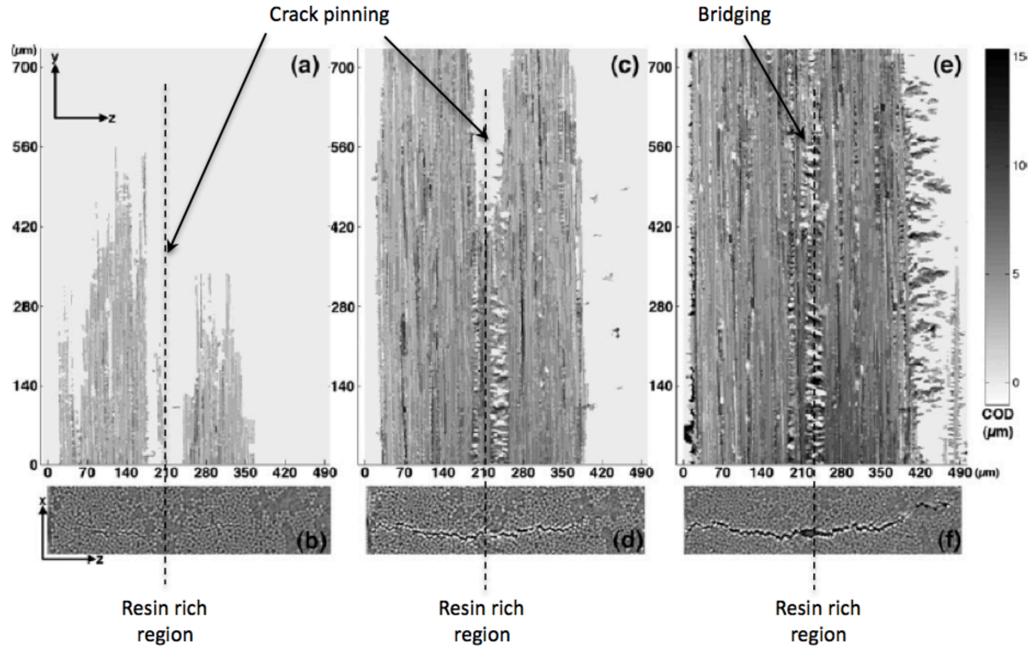

Figure 5.5: Evolution and COD of a 0° split in a $[90/0]_S$ laminate at increasing loads. Width, $W = 4$ mm. (a) Shape and COD of the split at 40% σ_f, (b) is a CT section taken at 140 μm in the y direction. (c, d), and (e, f) are the corresponding images but at 50% σ_f and 60% σ_f, respectively.

is retarded or pinned (and so within the field of view). It can also be seen that in this region there are areas in the crack wake where the COD $= 0$ μm. Analysis of the microstructure shows that this region corresponds to a resin-rich layer between the plies, which also contains a high density of toughening particles (Figure 5.5d) and the positions where COD $= 0$ μm are the bridging points between the echelon cracks similar to those identified in Figure 5.3b. The COD is approximately 3-6 μm throughout the split (although it may be narrower towards the end of the split that was not captured). There is no split towards the right-hand edge of the ply at 50% σ_f. Microstructural observations indicate that this region is unusually resin-rich. This region appears to be able to withstand the high local strains and inhibit crack initiation. This may be attributed to the toughening particles, which are ductile and affect load transfer and therefore the local stresses.

At 60% σ_f (Figure 5.5e) none of the crack tip is within the field of view. The bridging points between the hackles can still be observed along the length of the split. At 60% σ_f there is damage in the resin-rich region to the right of the sample; this damage has an irregular form similar to that seen in the resin-rich region in the centre of the split. Debonded toughening particles have been observed (Figure 5.3) but it is not possible to determine if they caused initiation or if they are associated with a preferential mode of propagation. The COD is generally greater along the split compared with either the 40% σ_f or 50% σ_f images with the COD being greatest towards the notch at 7-9 μm.

5.2.3 Finite element model

The qualitative observations from the SRCT images have been used to inform the development of a 3-D finite element model with the position of crack initiation and the split length forming the principal construction parameters. Quantitative information extracted from the CT images has been used to determine the accuracy of the model by comparison with its predictions. Whilst the voxel resolution of the images presented here is limited to 1.4 μm, sub-voxel interpolation may be exploited to determine edge locations to an accuracy of the order of 1/10$^{\text{th}}$ of this value (*e.g.* via the partial volume effect, taking into account the local grey scales associated with the edge detection regime).

For the initial analysis, linear elastic, 20-node second order hexahedral continuum elements, with reduced integration points were selected to be used with the ABAQUS™ solver [138]. The laminate has 3 planes of material symmetry to allow a model of 1/8$^{\text{th}}$ of the specimen volume to be used with appropriate boundary conditions for the nodal degrees of freedom. The conditions applied at each node at the 0°/0° interface within the solver input deck was $ZSYMM$, with degrees of freedom (DOFs) 3,4,5 equal to zero and 1,2,6 unconstrained. The conditions applied at each node at the centre-line in the x-z plane at the base of the model geometry was $YSYMM$, with DOFs 2,4,6 equal to zero and 1,3,5 unconstrained. The conditions applied at each node at the centre-line in the y-z plane at the side of the model geometry was $XSYMM$, with DOFs 1,5,6 equal to zero and 2,3,4 unconstrained. Within this model, DOFs 1,2,3 correspond respectively to translations along the x-, y- and z-axis and DOFs 4,5,6 correspond to rotations about the x-, y- and z-axis. Eight layers of elements were used to model each ply through the laminate thickness. The material properties for each ply have been specified directly according to the supplier's data sheet and are listed in Table 5.1 [124].

Figure 5.6 shows the mesh geometry representing the experimental samples that were imaged using the *in situ* SRCT test conditions. Nodal coordinates and element

Table 5.1: Material property constants used to define M21/T700 carbon fibre-epoxy composite in the fibre direction for finite element modelling.

Young's modulus E (GPa)	Poisson's ratio ν	Shear modulus G (GPa)	Thermal coefficient of expansion α ($10^{-6}K^{-1}$) [a]
$E_{11} = 148.0$	$\nu_{12} = 0.35$	$G_{12} = 3.8$	$\alpha_{11} = -1.0 \times 10^{-3}$
$E_{22} = 7.8$	$\nu_{13} = 0.35$	$G_{13} = 3.8$	$\alpha_{22} = 34.0$
$E_{33} = 7.8$	$\nu_{23} = 0.35$	$G_{23} = 2.9$	$\alpha_{33} = 34.0$

[a] Stress free temperature of 180 ℃

connectivity between these nodes were defined and created using an automatic meshing script developed in MATLAB. Within the linear elastic fracture mechanics framework, there is a stress field singularity at the crack tip due to the $r^{-1/2}$ term. In real materials where a singularity is impossible, local stress redistribution would occur, for example due to plasticity in ductile metals. To address the singularity in this model, the location of the mid-side nodes within the elements used to construct the crack tip were moved to become the quarter point nodes [36]. The 0° and 90° ply connectivity was defined by tying together the corresponding elements of the interface surface from each ply. The crack surface was modeled using separated nodes that initially occupied the same co-ordinates with the overall length of the crack determined from the SRCT images. The crack pinning described earlier and identified in Figure 5.5 implies that there is no single crack length. This ligamented crack front has not been accounted for and the value of the length to be used in the model was calculated based on equal overall crack face area. The loading conditions for the model were chosen to simulate the method by which the load was applied during the experiment. A mechanical load was applied by specifying a displacement of 5 mm on the upper surface of the model and the reaction force associated with this displacement was compared to the load cell measurements for each specimen. The ratio of the model reaction force to the load cell measurements was calculated to obtain an equivalent conversion factor. Due to the linear elastic behaviour of the FE analysis, the equivalent loading factor could be applied to the model predictions of COD and sliding displacement to obtain the results for comparison with the SRCT data. A thermal load induced by the residual stresses imposed during autoclave cure was also applied to the model, based on the coefficient of thermal expansion mismatch between adjacent plies during a temperature change of 180 ℃ to 25 ℃. A mesh refinement study was also carried out to confirm that the model results converge at the selected mesh density. The element edge lengths for the initial simulation were reduced until there was no further change in COD results between subsequent increases in mesh density. Using the meshing script, the crack position and length, material properties and mesh density could be varied parametrically for analysis of the model predictions for a variety of specimen size, layup and material systems.

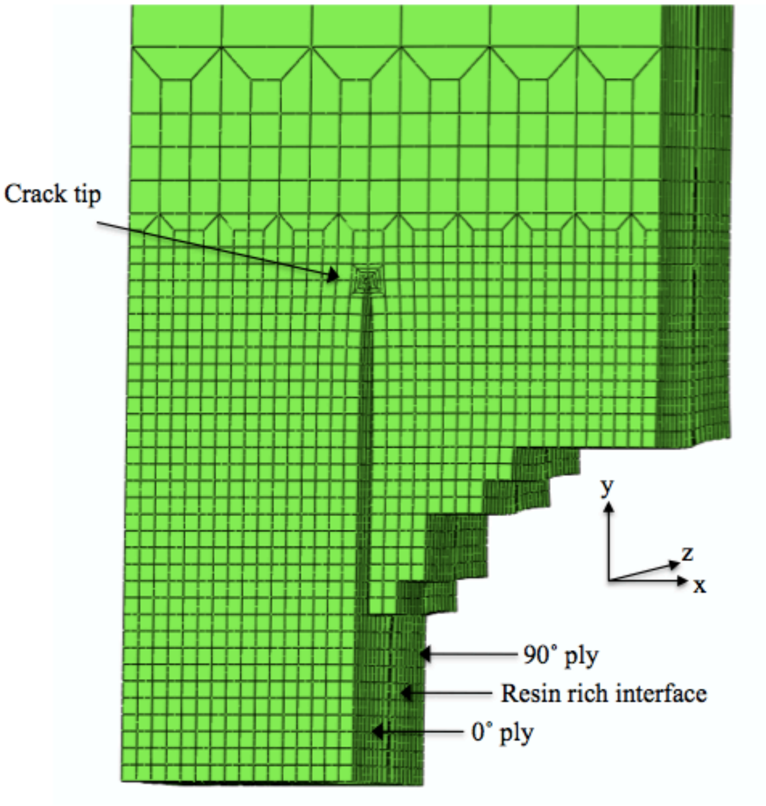

Figure 5.6: Finite element model mesh geometry representing the $[90/0]_S$ M21/T700 experiment sample. View of the deformed mesh around the split at the 0°/0° ply interface (symmetry conditions) under load.

To obtain COD and CSD results, the nodal displacements of the mesh were recorded after loading. For COD, the relative movement along the X-axis of each node pair that represents the split was determined along the length of the split for each of the eight elements through the thickness of the laminate. The sliding displacement was calculated as the relative motion of the node pairs along the Y-axis. Post-processing of the model returned separate results for mechanical load and thermal load for comparison with the corresponding experimental results derived from the loaded and un-loaded SRCT data.

For model validation the COD and CSD calculated from the SRCT data was compared to the model predictions. Figure 5.7 illustrates the locations around the split at which the calculations and predictions were taken. A COD plot was calculated from segmented SRCT images. The 3-D nature of the technique and analysis allows COD to be plotted as a function of position through the thickness of the two 0° plies and of position along the split length. The FE model assumes laminate symmetry and therefore consists of just one 0° ply. To facilitate an equivalent comparison with the experiment the COD data from SRCT analysis was mirrored and averaged across the two 0° plies. Figure 5.7b shows four locations along the length of the split. Each location is labeled according to the fraction of the split length and a plot of COD *vs.* position through the 0° ply thickness has been generated for each location. The location '4/5' is closest to the crack tip and the data is shown graphically in Figures 5.7 and 5.8. Figure 5.7c shows four additional, separate locations through the thickness of a 0° ply. Each location is labeled according to the fraction of the ply thickness and a plot of COD *vs.* position along the split length has been generated for each location. The location '1/5' is closest to the 0°/90° ply interface and the data is shown graphically in Figure 5.9. The dotted centre-line shows the boundary between the two 0° plies.

5.2.4 Model - experiment comparison

A comparison of the model results against the measured experimental results for COD is shown in Figures 5.8, 5.9 and 5.10 for a specimen loaded to 60% σ_f. In Figure 5.8 and 5.9 the opening displacement is plotted against the position through the thickness of the 0° plies for four positions along the length of the split. In Figure 5.10 the opening displacement is plotted against the length of the split for four equal incremental positions through the thickness of the two 0° plies. Figure 5.8 shows the results in the loaded state (a combination of mechanical and thermal stress). Figure 5.9 shows the results in an unloaded state where the thermal residual stress acts alone. Figure 10 shows the results of the difference between the loaded and unloaded states (purely mechanical load). Figures 5.8a, 5.9a and 5.10a show the experimental data and Figures 5.8b, 5.9b and 5.10b display the model data. The data in Figure 5.10b starts at 500 μm as the split does not initiate from the same location through the ply thickness. The experimental data was measured from the location closest to the notch at which the split was present through the entire ply thickness.

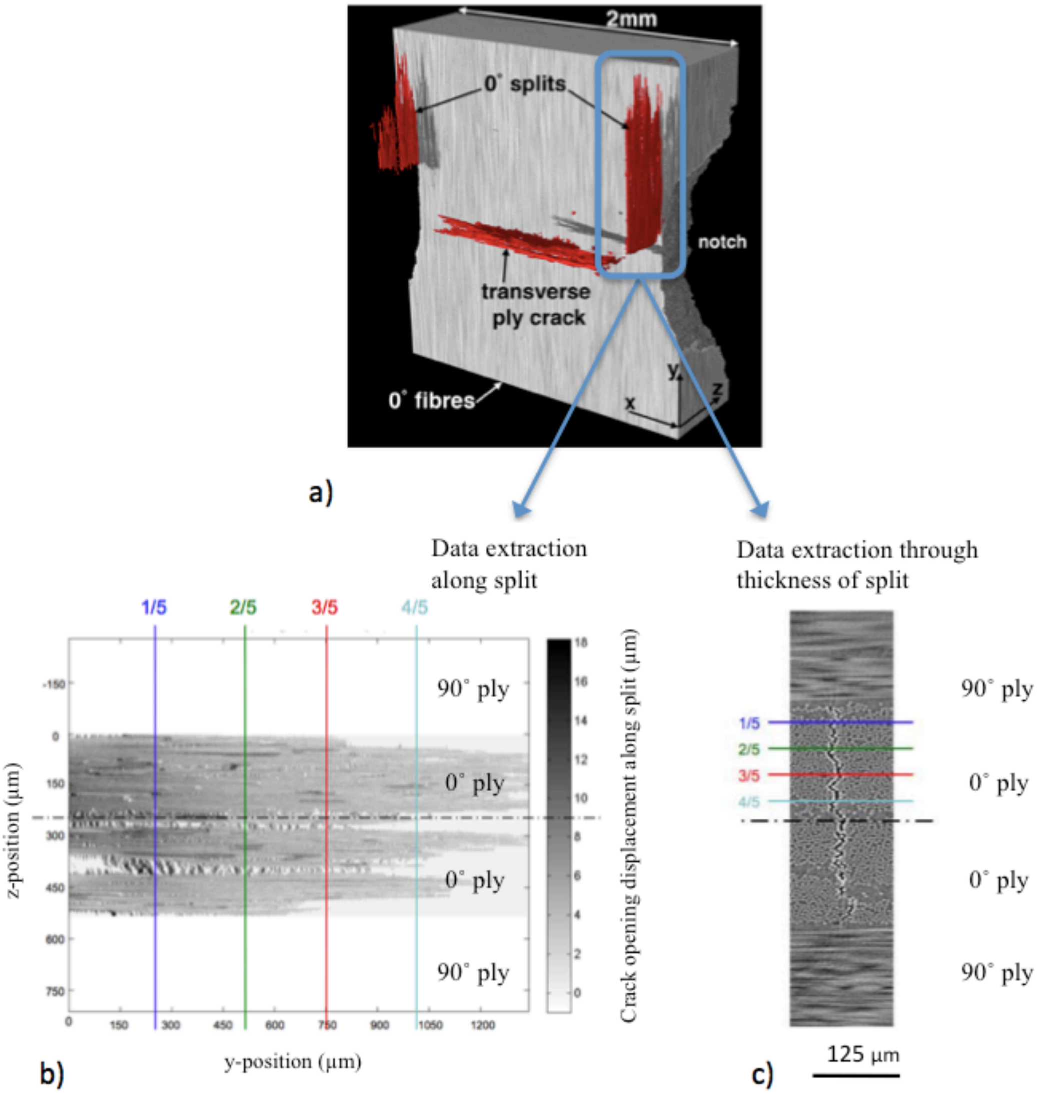

Figure 5.7: Extraction of quantitative experimental data at 60% σ_f. (a) Segmented tomographic volume of notch region of sample identifying particular region of damage (0° split) to be quantified, (b) COD plot of 0° split showing the four positions along the split length at which a comparison is made with model data, and (c) 2-D radiographic projection of 0° split showing the four positions through the laminate thickness at which a comparison is made with model data.

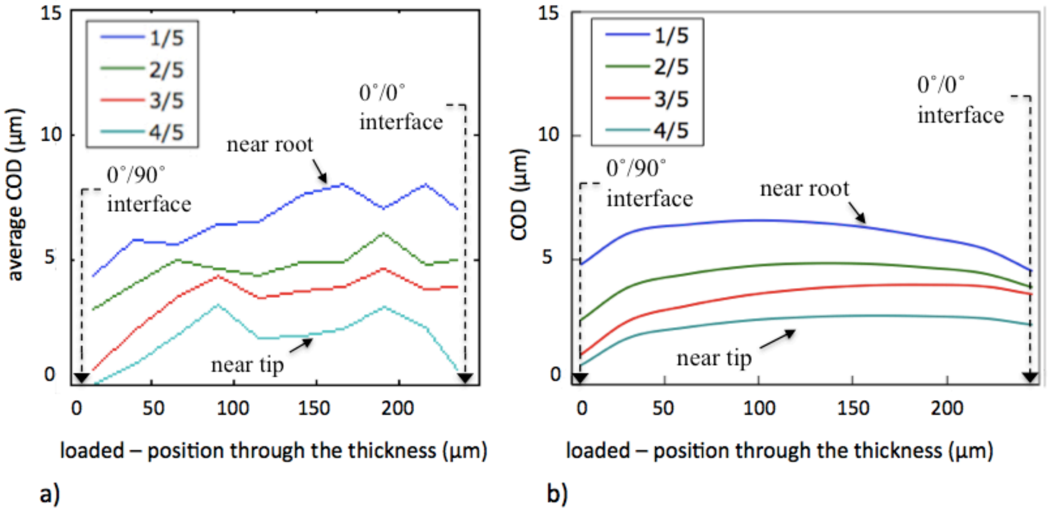

Figure 5.8: Plots of loaded-specimen crack opening displacement through the ply thickness for multiple positions along the split length from the split root towards the tip. (a) Experimental data mirrored and averaged across two 0° plies, and (b) model data for one 0° ply (by symmetry).

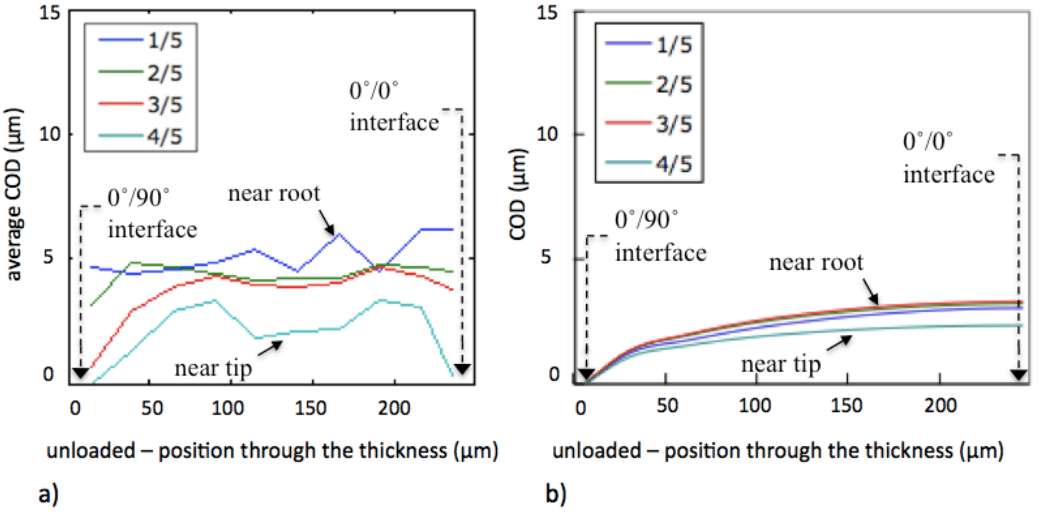

Figure 5.9: Plots of unloaded-specimen crack opening displacement through the ply thickness for multiple positions along the split length from the split root towards the tip. (a) Experimental data mirrored and averaged across two 0° plies and (b) model data for one 0° ply (by symmetry).

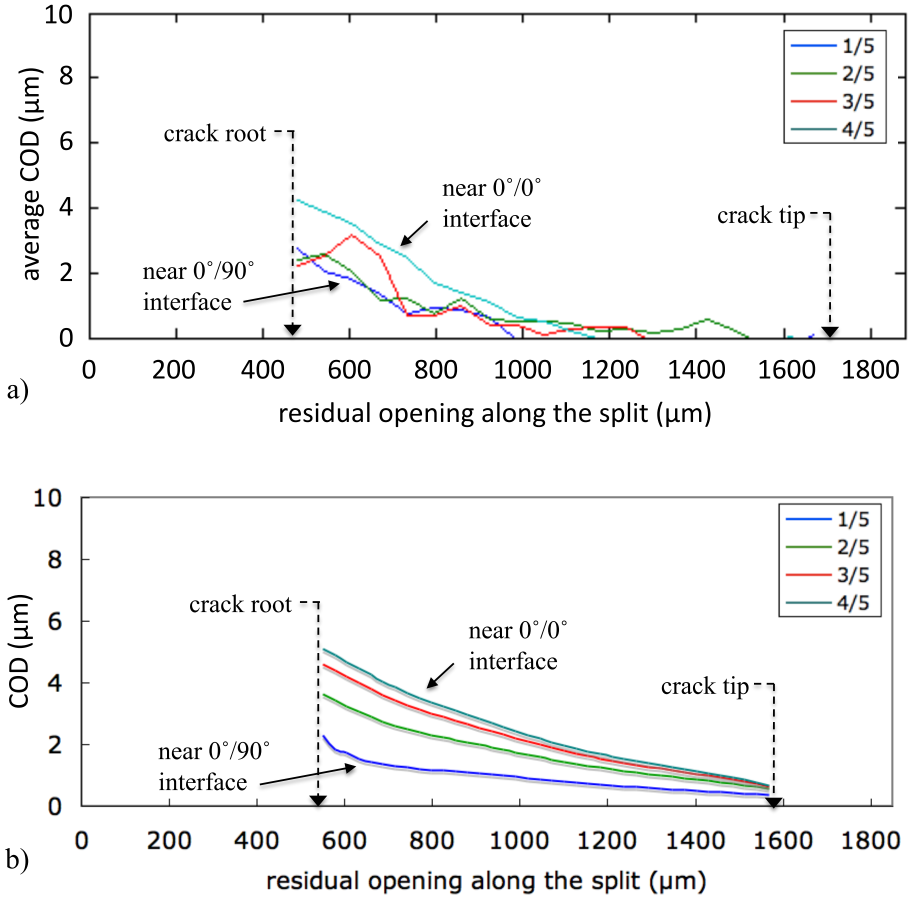

Figure 5.10: Plots of residual crack opening displacement along the split length for four positions through the ply thickness. (a) Experimental data and (b) model data. Positions are distinguished by fraction of the depth into the 0° ply thickness from the 90°/0° interface towards the 0°/0° interface.

The COD data presented in Figures 5.8 and 5.9 show that there is reasonable agreement between the experimental and model results. As expected the crack is more open at the root than at the tip and exhibits pinned behaviour with reduced opening as the crack approaches the 0°/90° interface. The graphs of experimental and model results show similar trends both through the thickness of the laminate and along the length of the split despite the immediate simplifications in the idealized model compared to the observed experimental data. As identified in Figure 5.5, the experimental crack does not have a single simple length value to which the model can be compared. In addition there are many microstructural features that have not been accounted for in the model, most notably the bridging and crack pinning along the length of the split, which occur at resin rich regions. Matrix-toughening particles have also been identified in these resin rich regions throughout the plies. The uneven trend of the experimental results is due to the non-straight-fronted crack propagation.

The crack opening displacement in the unloaded state is shown in Figure 5.9 and is due to the thermal residual stress. These graphs show that the contribution to COD is significant and as such thermal effects must be included when modelling laminate damage. Subtraction of the residual opening from the loaded case allows the COD from mechanical loading alone to be extracted. This is shown in Figure 5.10 in which COD is plotted along the length of the split for four positions through the laminate thickness. The experimental results and model predictions show good correlation both in terms of the overall trend and the absolute values.

The sliding displacement data is shown in Figure 5.11 where it can be seen that the model displacements vary substantially from the measured experimental results. In addition to the above discussion of experimental and FE data, further contributions to their comparison can be identified in the effect of the de-bonding of rubber toughening particles that have been introduced within the matrix (Figure 5.3) and transverse ply cracks in the 90° ply. The bridging/ pinning behaviour of the resin toughened regions has not been accounted for in the model. The experimental results show that the COD does not vary significantly through the thickness of the 0° ply. SRCT images also show that there is a matrix rich region at the interface between the 0° and 90° plies. The reduced compliance of the matrix with respect to the averaged 0° lamina properties may allow the stress gradient at the 0°/90° ply interface to act mostly across this region alone. The model does not incorporate this region at present and uses element tying to attach the plies. This method effectively pins the split at the interface and does not allow for deformation.

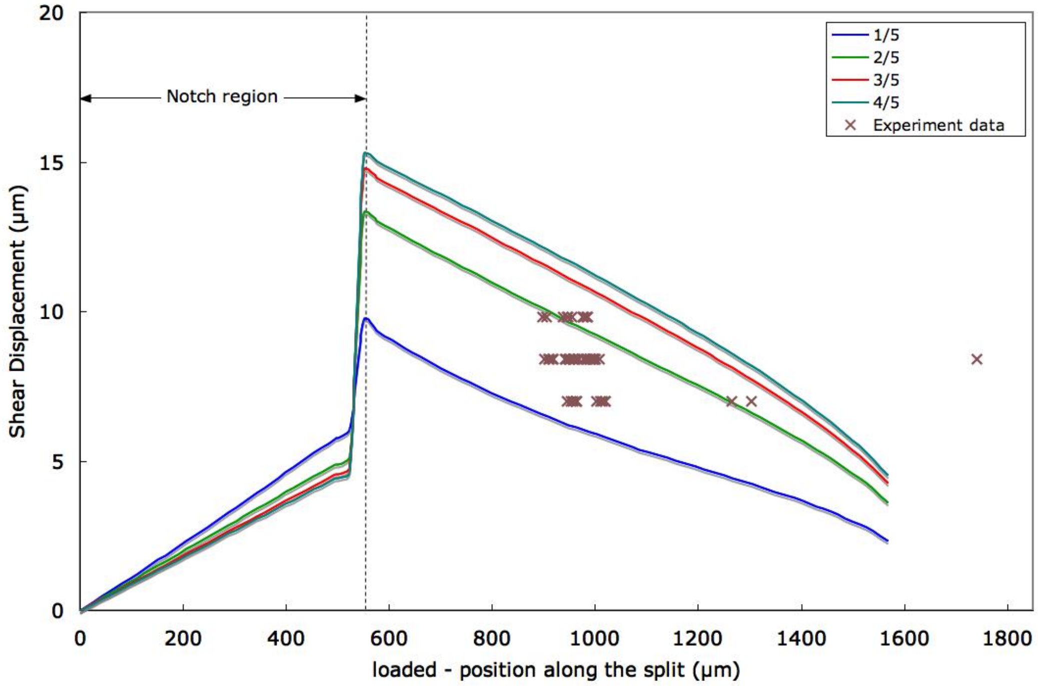

Figure 5.11: Plots of sliding displacements along the split length for 4 positions through the ply thickness.

It is evident that, having seen the true three dimensional behaviour of cracking in the CT data, the FE modelling of a simple straight crack front is missing important micromechanical detail. Future work is underway to develop more detailed finite element models that include the observed micromechanical detail and an analysis of the sensitivity of the model to resin material properties and toughening processes. The loads applied in the study presented here were below the threshold for initiation of delamination: future modelling work aims to determine the effect of inter-ply decohesion on displacement fields and energy release rate during damage growth as the load approaches the laminate failure stress using approximations for element behaviour from the SRCT data. The strain energy release rate can be used to predict onset and propagation of crack growth and can be calculated from finite element models using the virtual crack closure technique. The experimentally measured displacement field can be used to estimate SERR as G is equal to the product of opening displacement and stress field at the crack tip [36]. Matrix cracking has been shown to reduce laminate stiffness and SERR in work by Zhang *et al.* [112] and by Kashtalyan and Soutis [113] in which the laminate stiffness matrix is used to calculate SERR with an analytical model.

SERR from exepriment data can therefore be compared to analytical results and FE predictions to determine the effect of matrix cracking on crack growth. Notwithstanding the need for more refined models it is evident that the initial modelling presented herein makes predictions for the internal crack openings and displacements under load experimentally which are of the correct order. A key point to highlight is that with the internal full field measurements afforded by the SRCT data, uniquely detailed model initialisation and validation may be achieved.

5.3 Conclusions

Using X-ray CT it has been possible to evaluate the complex shape of 0° splits in toughened composite materials. In the resin-rich regions, which have been shown to contain toughening particles, both crack pinning/retardation and bridging mechanisms have been observed. In the regions where fibres are close packed, the splits are less constrained and appear able to advance more freely. Further analysis is required to fully understand the effect of the resin-rich, toughened regions on the crack tip K and G.

The three-dimensional nature of damage onset and growth has been observed, allowing the extent of intralamina damage to be quantified with a confidence not possible using conventional 2-D imaging methods. Using microstructural features it has been possible to calculate local displacement fields around the intralaminar 0° splits. In addition the CT data provides information on crack opening displacements along the splits and this information has been used to inform the development of an initial finite element analysis model of the intralamina damage. While the 0° splitting is mode II dominated, the ability to quantify damage in three dimensions has enabled a study of crack density and opening displacement for transverse ply cracks within the 90° plies using the same *in situ* SRCT data [135]. The quantitative data for strains and COD allows the model of 0° splitting to be validated for the loading conditions of interest. The ‘data rich’ mechanics approach that SRCT offers is a valuable tool in developing and validating finite element models. Micron-scale damage can be resolved readily and full field, internal 3-D data is made available for model comparison.

Chapter 6 will concentrate on a more complete evaluation of micromechanical toughening and the development of full-field strain maps for composite materials subjected to a range of static loads. COD and CSD is studied in greater detail and strain energy release rate is calculated in the FE model to predict crack growth with load.

CHAPTER 6

DETAILED MICROMECHANICAL OBSERVATIONS AND MODELLING OF THE EFFECTS OF VARIATIONS IN COMPOSITE MICROSTRUCTURE

This chapter describes the extension of the previous experimental work to include the analysis of multiple material systems to determine the effect of toughening mechanisms and the variation in local microstructure on damage initiation and propagation. The baseline model described in Chapter 5 has been developed to include approximations of the effects of toughening for comparison with the earlier model predictions and with additional experimental results. The application of the virtual crack closure technique is described in further detail in this chapter with reference to the extended model. While the focus of the model-experiment comparison is directed at the finite element model developed as part of this project, it is intended that the methodology described in this chapter demonstrates the capability of SRCT as a technique that can be applied to develop, calibrate or validate a generic model. The details of the experiment are described in Chapter 3 as experiment set 3. All of the material systems and stacking sequences within Table 3.1 were tested, with the raw image data from the experiments available to the composites community from the Materials Data Centre [139]. However, the experimental results and FE analysis presented here correspond to $[90/0]_S$ M21/T700 laminates with 4 mm DEN specimen geometry. SRCT post-processing for quantitative experimental results and segmented images of damage was carried out by Mark Mavrogordato [21].

Synchrotron radiation computed tomography (SRCT) has been used to obtain 3-D, high fidelity, high resolution, *in situ* damage growth characterization in notched, laminated carbon fibre-epoxy $[90/0]_S$ composites. Damage has been quantified in terms of crack opening and sliding displacements and crack front growth under tensile loads ranging from 30% nominal failure stress to failure. Evolution of damage has been identified and presented in greater three-dimensional detail than previously reported in the literature, illustrating the complexity with which the primary damage mechanisms interact. Key microstructural features have been identified and their effect on the initiation and evolution of damage evaluated. In addition a 3-D finite element (FE) model has been developed to predict the mode I and mode II crack face displacement profiles and strain energy release rate in a 0° ply split of the notched laminate for comparison with the SRCT data. The model has been formulated to account for the observed damage mechanisms, the resultant thermal residual stress imposed during autoclave cure and material behaviour and properties. The sensitivity of the model predictions to each of these parameters has been evaluated to determine the effect of homogenising particular microstructural features and material properties.

6.1 Introduction

The inherent complexities of laminated composite failure mechanisms (0° ply splitting, off-axis matrix cracking, interlamina cracking, fibre rupture etc. [27–30]) require sophisticated models incorporating the fundamental mechanics that govern the interacting fracture processes in order to predict accurately initial and progressive damage parameters. A micro-mechanical model that captures and defines each of these processes would be excessively costly in terms of computational resources. Although qualified assumptions can simplify the problem, and allow more practical simulation run times, each simplification will incur a sacrifice in the accuracy of the model predictions. Fitting parameters can be applied to the model to improve the data sets against a given material system, layup and loading regime, however this approach has no physical justification and is unlikely to yield satisfactory predictions if, for example, the layup or load case is changed [42–44]. This is illustrated by a recommendation that ±50% of the predicted final strength of a number of internationally recognised failure theories that has been suggested as an appropriate tolerance to be used for component design [11].

This paper continues from previous work [125, 128–130, 136] in which the capability of SRCT to identify the micromechanisms involved in damage initiation and propagation leading to laminate failure was demonstrated in 3-D with unprecedented fidelity. In the work presented here the influence on damage evolution of particular features and regions, such as toughening mechanisms within resin rich areas of the laminate and the morphology of crack fronts, has been unambiguously identified and has informed the construction of 3-D FE models to predict damage parameters based on an approximation of these features. This study has afforded an original insight into the damage processes that have significant effects on the model predictions, and the degree of complexity required of a model in order to predict damage growth with sufficient precision.

A benchmark model with homogenised ply material properties was defined from which subsequent models have been derived, each incorporating an approximation of the effect of directly observed mechanisms. Material properties have been modified to account for regions of local toughening of the epoxy matrix due to low modulus polymer precipitates [141]. Crack lengths have been adjusted to account for pinning which results in a geometrically non-linear crack front. Resin rich regions have been included at the mid-ply locations observed via SRCT imaging. Data sets for crack opening displacement (COD) and sliding displacement have been produced from the SRCT images for direct comparison with the model results as a function of applied load and 0° ply split length. Quantitative experimental results are restricted to 0° ply splitting, however the progression of damage from initiation to final failure has been characterised in greater detail with particular attention focussing on the evolution of transverse ply cracks, splits and delamination. Fiducial marker particles, introduced to the laminate during cure, have been tracked during each load step to enable full field displacement maps to be plotted through manual volume correlation. The virtual crack closure technique (VCCT) has also been employed to determine the mode I and mode II components of strain energy release rate [115] and to predict the crack growth with load for comparison with experimental results.

The post-processing involved in the analysis of each SRCT scan is extremely laborious, requiring meticulous examination of very large data sets. As such, although a total of 160 scans were performed during this experiment set, with test specimens varying in matrix toughness, laminate layup, specimen geometry (notched and un-notched) and loading regime, only one material system and layup is considered in this paper. The fully populated set of results and images obtained represent a comprehensive insight into progressive damage processes associated with composite structures of a useful engineering configuration, providing a more complete understanding of laminate failure. Access to these results and high resolution tomography images has been provided at the University of Southampton Materials Data Centre [139].

6.2 Results and discussion

6.2.1 Experimental observations

Reconstructed SRCT data produces a representative volume of the original test specimen. The local X-ray attenuation due to structural variations during transmission through the material translates to a high fidelity 3-D grey-scale map. Figure 6.1 shows an example of a volume centred about the notch with each ply clearly identified by the orientation of the fibres.

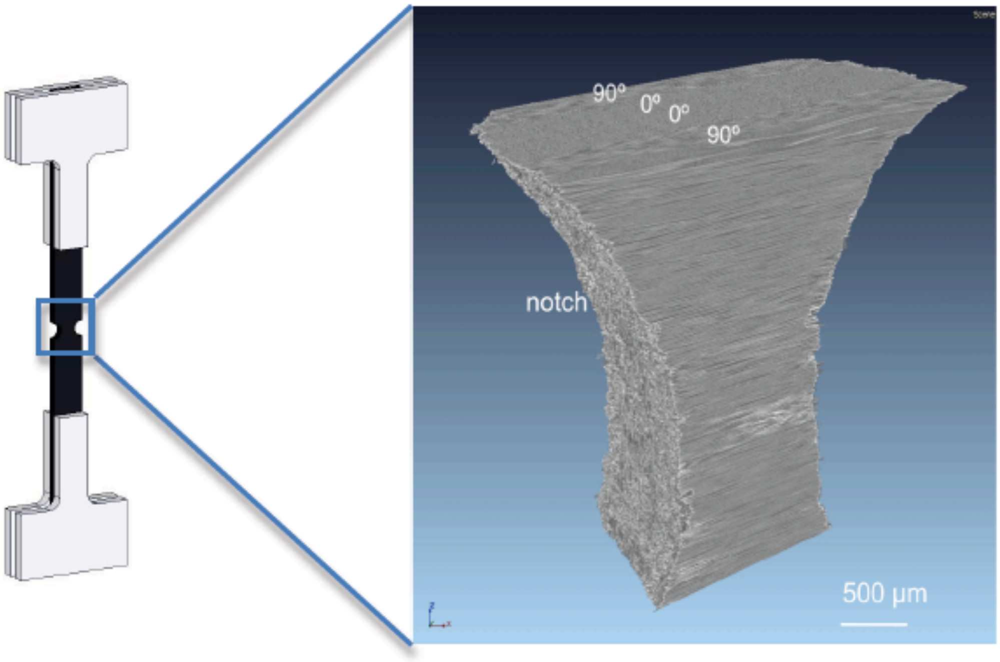

Figure 6.1: Reconstructed SRCT volume showing a 4 mm DEN undamaged $[90/0]_S$ M21/T700 laminate construction and notch geometry.

The grey-scale intensity spectrum contains two distinct peaks that represent air (cracks, splits, delaminations, *etc.*) and intact material. Defining regions of a specific grey-scale threshold enables particular features to be identified and segmented. Figure 6.2 shows the progression of damage with load in which transverse ply cracks (TPCs) have formed in the 90° plies at 30% σ_f. At 50% σ_f new TPCs have formed and existing cracks have extended in both the in-plane and through thickness directions. At 60% σ_f splitting in the 0° plies has initiated with distinct branching or pinning observed. At 70% σ_f the 0° ply splits have grown and one of the TPCs has evolved into the onset of delamination. With increasing load the 0° splits continue to grow in length, and further delamination is observed to consist of interactions between fibre-matrix debonding at 0°/90° inter-ply interfaces and rubber toughening precipitate-matrix debonding in resin rich regions. The final image was obtained at 110% σ_f and shows multiple interactions of TPCs, 0° ply splits and delaminations.

Individual fibre breaks have been identified with a further increase in load resulting in final laminate failure as cascading fibre-cluster breaks occur at 1165 MPa in this sample, which failed at 113% of the nominal notched failure stress. The increase in laminate strength with damage has been documented [31], and is due to the isolation of 0° ply sections from the stress raising effect of the notch due to splitting and delamination as shown in Figure 6.3. Comprehensive damage growth observations and the effects of local microstructure have been detailed previously [140, 141], and while it is evident that these images provide informative, qualitative observations relating to the initiation and accumulation of damage in a laminate, quantitative data is required in order to make a useful comparison with model predictions.

6.2.2 Quantitative experimental results

6.2.2.1 Crack opening displacements

The splits in the central 0° plies have been segmented and extracted from the remainder of the volumes as individual objects showing the progression of splitting damage alone (Figure 6.4). The raw 3-D image data has been binarised to create a 3-D array of connected voxels that represent the coordinates of the volume of the crack. The binarised data has been converted into crack opening displacements for each split

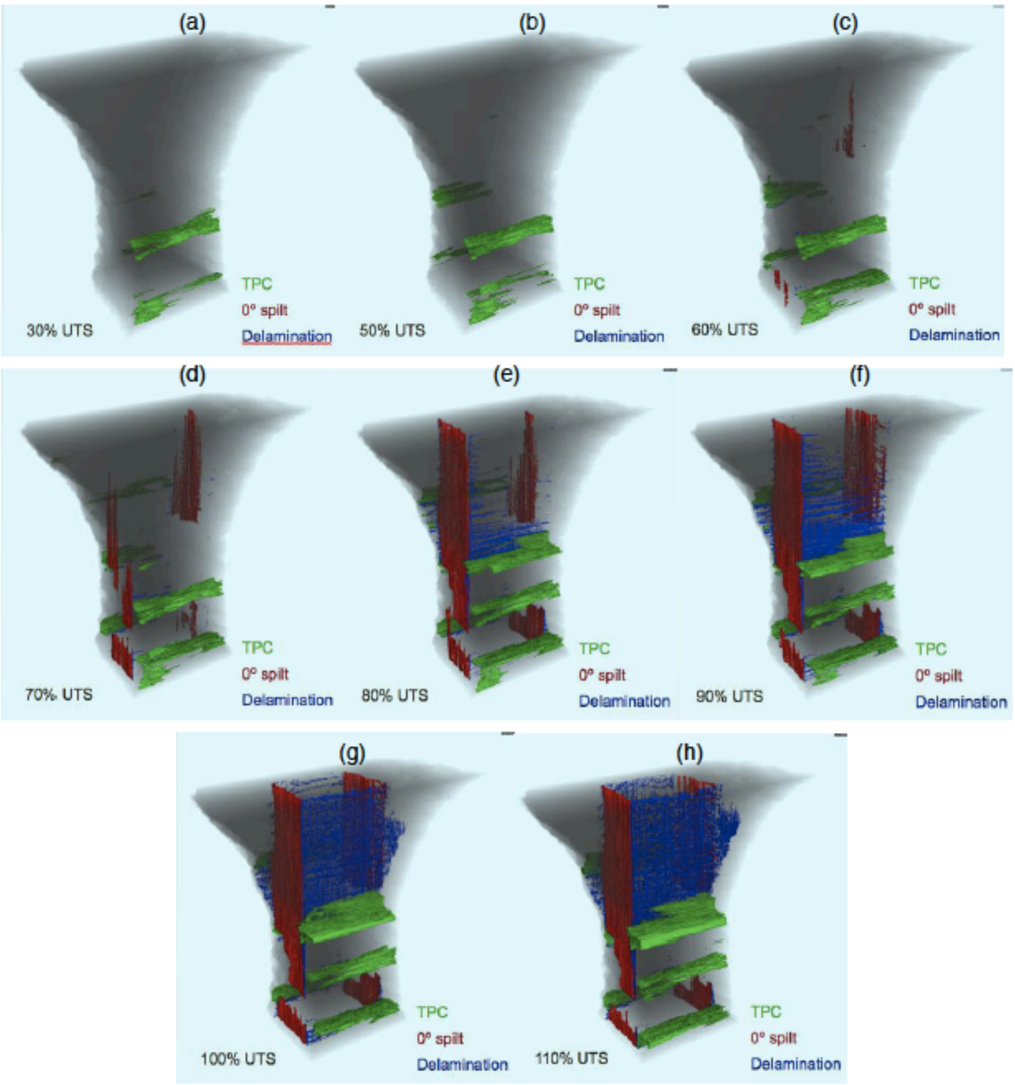

Figure 6.2: Segmented SRCT volumes showing damage accumulation during incremental static tensile loading of a DEN $[90/0]_S$ carbon fibre reinforced specimen from 30% to 110% nominal UTS. The specimen bulk is shown as a shadow for reference; TPCs are shown in green, 0° splits in red, and delaminations in blue. [140].

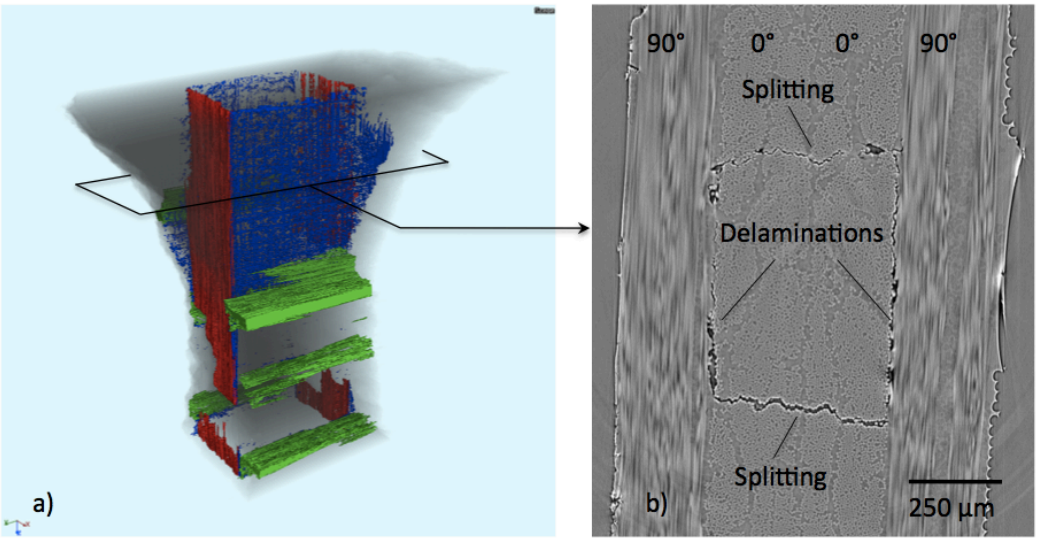

Figure 6.3: Direct SRCT observation of specimen damage state. (a) Damage state in a specimen loaded to 110% nominal failure stress; (b) 2-D slice in which splitting and delamination in the specimen isolate a central section of the sample from the stress concentrating effect of the notch tip stress concentration.

by calculating the number of connected split voxels through the ply thickness for each of the in-plane voxel positions. The resultant plot shown in Figure 6.5 is a 2-D map of the in-plane split profile with a scale that represents opening displacement. The darker regions indicate a larger opening.

The 0° ply splits illustrated in Figure 6.4 and the COD plot in Figure 6.5 show the variations in length of the crack front for each load-step and the effect of local toughening mechanisms, evident in the form of crack bridging and pinning. The extent of the influence of these mechanisms, for example total pinning length as a function of split length, changes through the load-steps, implying not only that there is a local variation in fracture toughness throughout the ply, but that the fracture toughness also changes with position relative to the crack tip.

To enable comparison with the model predictions, line plots of COD along the length of the 0° ply split were produced from the split profiles. The symmetry conditions applied to the FE simulation allows a single 0° ply to be modeled. To produce equivalent experimental results, the COD measurements from SRCT images at the crack surface were mirrored across the centerline of the 0°/0° ply interface and averaged to produce displacement values for the crack across a single 0° ply. The crack surface was divided into five bins of equal width through the 0° ply thickness, with bin 1 representing the region closest to the 0°/0° ply interface and bin 5 closest to the 0°/90° interface.

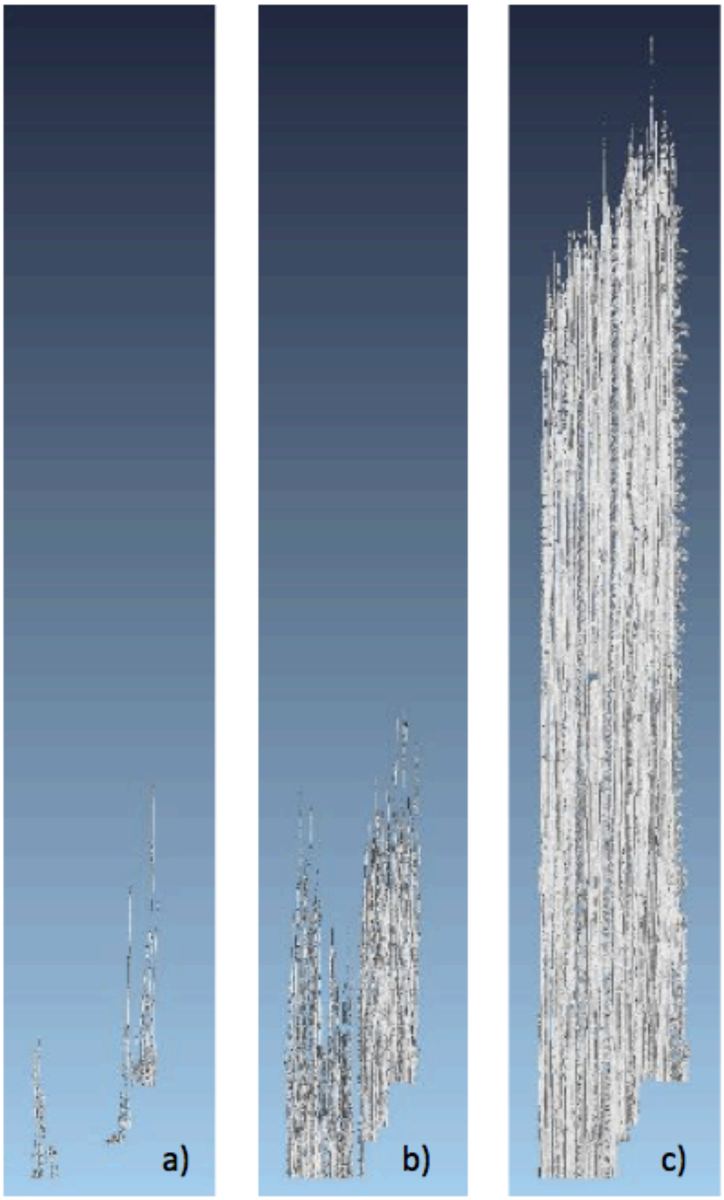

Figure 6.4: Progression of 0° ply split growth and pinning behaviour between load steps. (a) 60% σ_f, (b) 70% σ_f, (c) 80% σ_f.

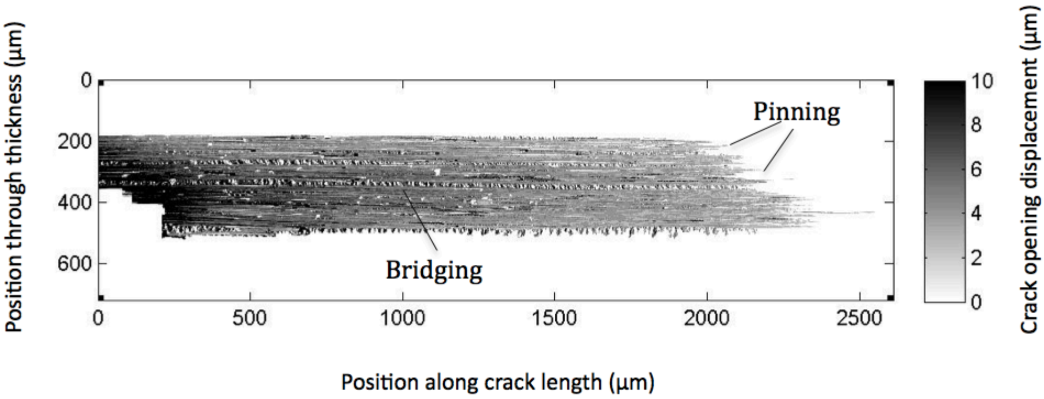

Figure 6.5: Experimentally measured COD plot for 0° ply split at 80% σ_f.

Within each bin, the displacement values for voxels along the split were averaged across the bin width to produce the curves shown in Figure 6.6.

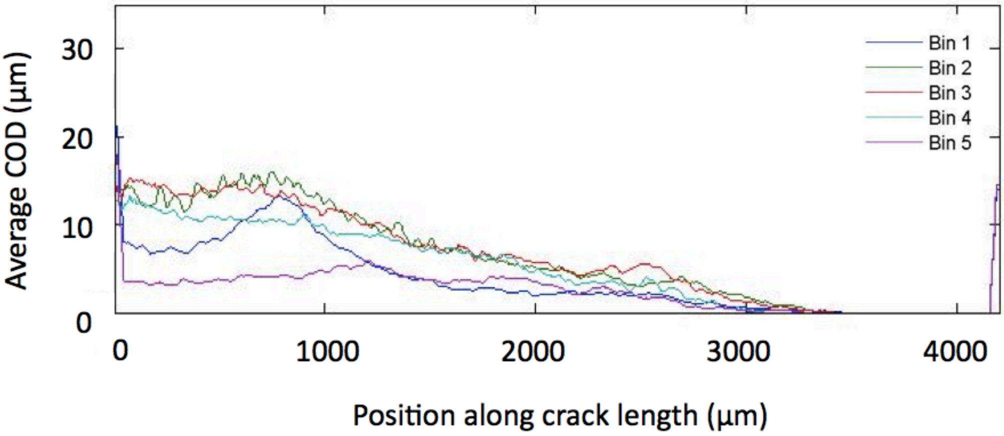

Figure 6.6: Plot of experimentally measured COD along 0° ply split at 80% σ_f. Combined contribution from mechanical load and thermal residual stress.

6.2.2.2 Crack sliding displacements

Particular features within the volumes, predominantly the aluminium particles described in Section 3.2; experiment set 3, have been identified, segmented and tracked between load steps. The relative displacement of feature pairs across the split flanks due to local strain has been measured to determine the mode II displacements in the vicinity of the 0° splits, plotted in Figure 6.7. Each of the features used in the calculation along the split was located at a distance of less than 140 μm from the surface of the 0° ply split in the direction of the normal to the surface. Migration of the aluminium particles from resin flow during cure was low, and the particles remained within the ply interface regions. The plot shown in Figure 6.7 represents the CSD at a 90°/0° ply interface where the majority of the particles were identified. Although the technique is dependant on the presence of suitable features, manual segmentation of these features in a single 2-D slice of an SRCT scan is reasonably straightforward. This becomes a time consuming process, however, when the task is expanded to encompass a slice-by-slice interrogation of the entire 3-D volume ($\sim$ 700 slices). Although feature tracking is an accurate and reliable method by which local displacements can be obtained, an automated approach must be developed if a large number of volumes are to be analysed.

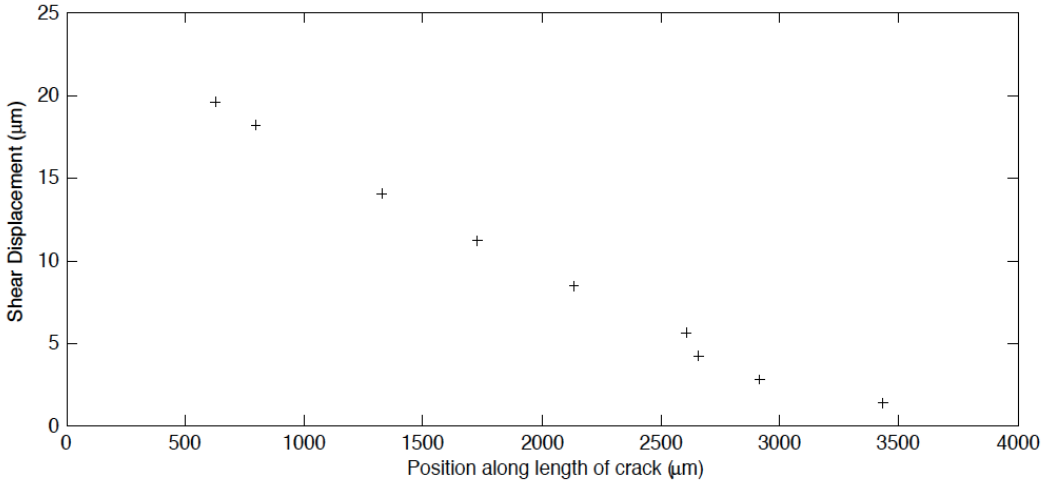

Figure 6.7: Plot of experimentally measured sliding displacement at the 0°/90° ply interface along the split at 80% σ_f. Combined contribution from mechanical load and thermal residual stress.

6.2.2.3 Crack length *vs.* load

Split lengths for the range of loads were measured for comparison with the model predictions calculated using SERR results. Figure 6.8 shows a plot of crack length in the samples at loads of 40%, 65%, 80% and 90% σ_f. The split is only a few tens of microns in length until 65% σ_f beyond which point rapid growth occurs with further increases in load.

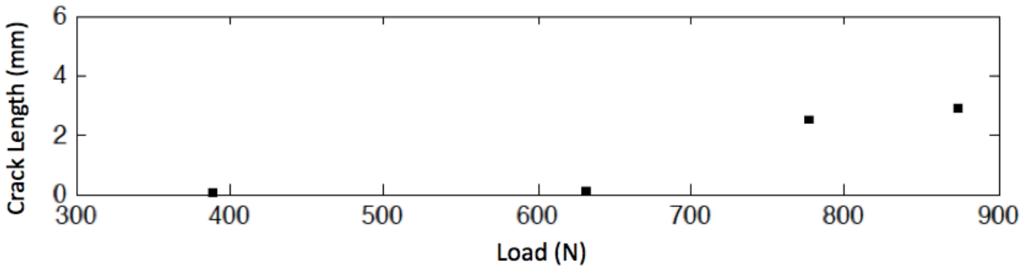

Figure 6.8: Plot of experimentally measured crack length with increasing load.

6.2.3 Finite element model

6.2.3.1 Model construction

The model is based on the simulation described in previous work [130] and uses duplicated nodes to embed a pre-existing split in the model. The location and split length is specified to reproduce damage conditions observed in the experiment data. Elastic, 20-node, quadrilateral, 3-D, solid continuum elements with reduced integration points were used to create a mesh with three planes of material symmetry to allow a model of $1/8^{\mathrm{th}}$ of the specimen volume to be specified with appropriate boundary conditions for the nodal degrees of freedom. Eight layers of elements were used to model each ply thickness with a refined mesh at the crack tip. The idealizations of the observed features and mechanisms are compared for six simulations, described below and summarized in Table 6.1. Figure 6.2 shows that the growth of splits, TPCs and delaminations is not symmetrical and this difference will be a source of error in the predicted results. The aim of the present work is to determine the capability of SRCT as a technique to provide quantitative data to inform model development and against which to compare model predictions. More accurate representation of damage distribution in models is discussed in the conclusions of this thesis in the context of future work.

Table 6.1: Model approximations to features and mechanisms observed during SRCT imaging.

Simulation	Approximation
1	Baseline model. Minimum observed crack length.
2	Baseline model. Area averaged crack length.
3	Baseline model. Maximum observed crack length.
4	As simulation 2 with modified material properties.
5	As simulation 2 with mid-ply resin rich regions.
6	As simulation 5 with modified material properties.

The material properties for each ply have been matched to the manufacturer's published data, shown in Table 6.2 [124]. The epoxy resin properties were initially chosen using the transverse lamina properties from the manufacturer's data sheet and subsequently adjusted to determine the sensitivity to microstructural effects such as toughening particle precipitates. A rule of mixtures approach was used to estimate the modified resin properties based on the local volume fraction of rubber toughening particles, measured to be 60% by SRCT [135]. Local variations in the fibre volume fraction have been approximated by incorporating mid-ply resin rich regions. The baseline model uses a single resin rich region between the 0° and 90° plies. A refined model is included in the study that incorporates the observed mid-ply resin rich regions which arise due to the combination during manufacture of two half-thickness plies to constitute a single pre-preg ply. The length of the embedded crack was initially determined using an area-averaged approximation and modified in later iterations according to the minimum and maximum location along the split of the crack front.

Table 6.2: Material property constants used to define M21/T700 carbon fibre-epoxy composite in the fibre direction for finite element modelling.

Young's modulus E (GPa)	Poisson's ratio ν	Shear modulus G (GPa)	Thermal coefficient of expansion α ($10^{-6}K^{-1}$) [a]
$E_{11} = 148.0$	$\nu_{12} = 0.35$	$G_{12} = 3.8$	$\alpha_{11} = -1.0 \times 10^{-3}$
$E_{22} = 7.8$	$\nu_{13} = 0.35$	$G_{13} = 3.8$	$\alpha_{22} = 34.0$
$E_{33} = 7.8$	$\nu_{23} = 0.35$	$G_{23} = 2.9$	$\alpha_{33} = 34.0$

[a] Stress free temperature of 180 °C

6.2.3.2 Virtual crack closure technique

To determine the strain energy release rate (SERR) driving crack growth at the crack tip, the virtual crack closure technique (VCCT) was applied to the benchmark 0° ply split model. Prior to this, the implementation of the technique was first validated for pure mode I, pure mode II and mixed mode I, II SERR using double cantilever beam (DCB), edge-notched flexure (ENF) and end-loaded split (ELS) examples in which analytical solutions shown in Figure 6.9 [142] were compared to finite element solutions. Figure 6.10 shows the finite element model construction for the particular example of the DCB simulation to determine mode I SERR. The DCB model contains the same crack tip mesh as the 0° split in the $[90/0]_S$ laminate model. Nodal reaction forces were obtained using symmetry boundary conditions for the geometry to enable solution outputs to be requested from the FE solver (Figure 6.10b). The reaction forces ahead of the crack tip and the nodal displacements in the wake of the crack tip at the locations shown in Figure 6.10c were combined to determine the SERR according to equation 2.11. To determine the parameters used in this equation, a set of four nodes is identified at each location through the thickness of the model in Figure 6.10c. At each location the product of mode I force ahead and mode I displacement in the wake of the crack tip was calculated for the corner nodes $(Z_{C_i}, w_{C_i} - w_{C_i*})$ and mid-side nodes $(Z_{M_i}, w_{M_i} - w_{M_i^*})$. The sum of all force-displacement products at each corner node and mid-side node location was calculated for all locations along the width of the crack.

The factor of $\frac{1}{2\Delta A}$ was applied to the result, where ΔA is equal to the crack surface area represented by the extension of the crack width by the distance corresponding to the edge length of an element behind the crack tip. Similar models were constructed for ENF and ELS examples with the results of a comparison between the exact solutions from the literature and the model predictions shown in Table 6.3.

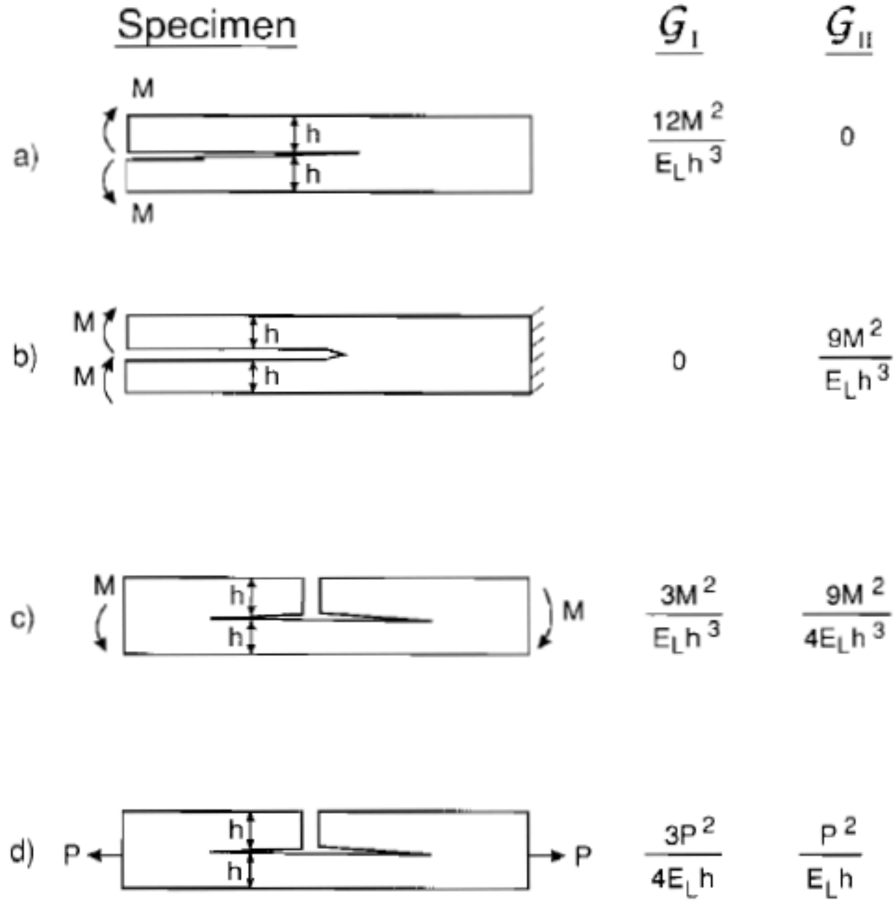

Figure 6.9: Analytical solutions for G_I and G_{II} for pure mode I, pure mode II and mixed mode I, II loading (reproduced from Hutchinson and Suo [142]). E_L is the Young's Modulus in the longitudinal direction.

The practical application of VCCT to the $[90/0]_S$ laminate model is presented at the end of this sub-section, for which an alternative method was required to obtain the components of force at the nodes ahead of the crack tip. The 0° split is embedded within the model geometry, and the surfaces are not subject to nodal constraints such as those for symmetry, and as such reaction forces cannot be requested as solution outputs. It was determined from the documentation for ABAQUS™ that nodal forces can be obtained instead for any element in the model using the output request, *nforc*. The meshing script for the model is an automated version of a manual mesh which

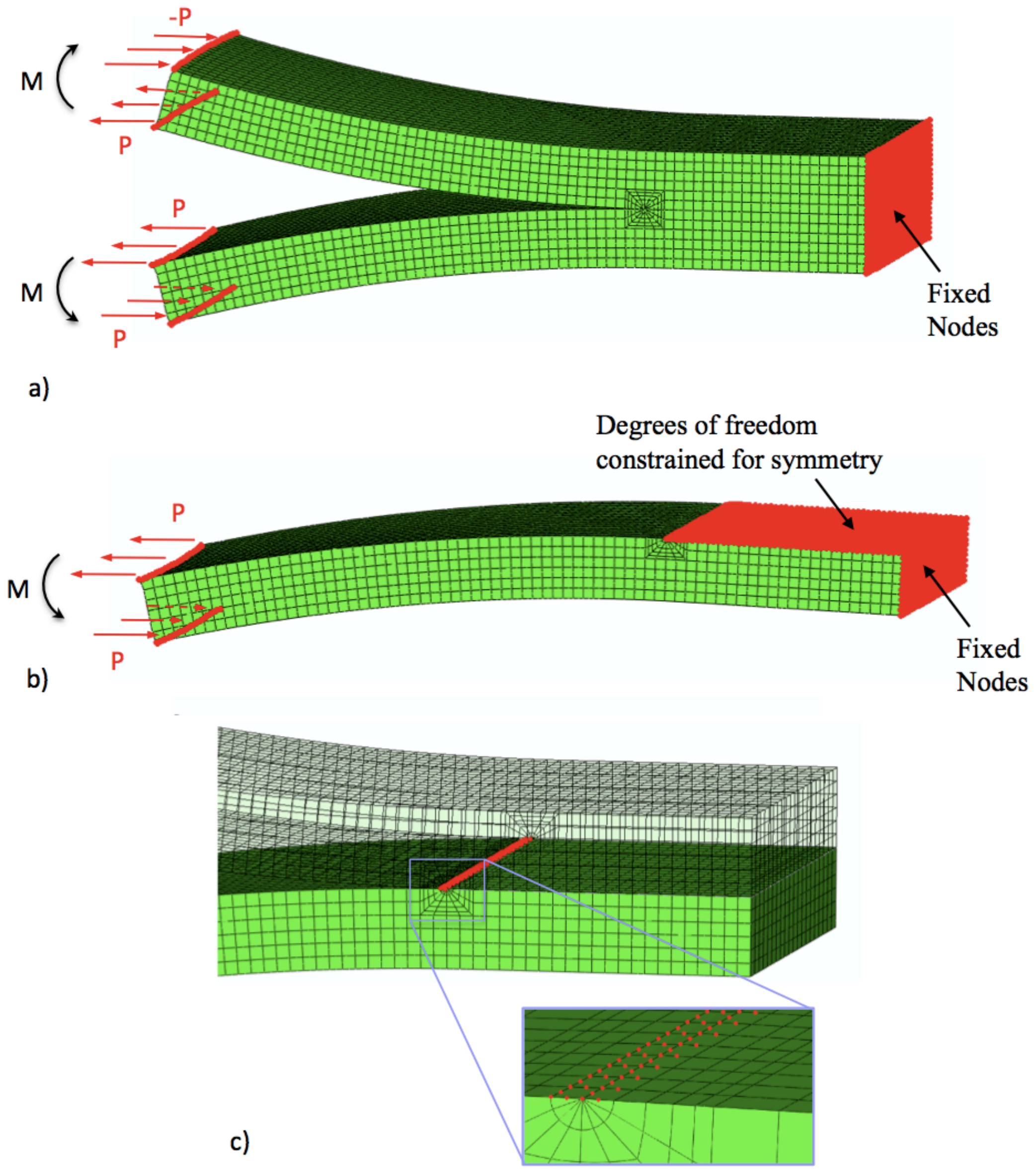

Figure 6.10: Implementation of DCB loading to determine G_I within the finite element model. (a) Model representation of DCB loading; (b) nodes constrained using symmetry conditions to enable output of reaction forces; (c) nodes used to determine force and displacement vectors for VCCT calculation in the region of the crack tip.

Table 6.3: Comparison of model predictions and analytical solutions for values of G for mode I, mode II and mixed mode I, II strain energy release rate.

Load case	Mode	Type of analysis	G_I; G_{II} (Jm^{-2})	Difference (%)
DCB	I	FE Analytical	1.46x10^{-5}; 0 1.46x10^{-5}; 0	0.2, -
DCB	II	FE Analytical	0; 6.15x10^{-7} 0; 6.59x10^{-7}	-, 6.6
ENF	I, II	FE Analytical	2.20x10^{-7}; 1.54x10^{-7} 2.20x10^{-7}; 1.65x10^{-7}	0.3, 6.6
ELS	I, II	FE Analytical	2.45x10^{-8}; 3.04x10^{-8} 2.44x10^{-8}; 3.25x10^{-8}	0.2, 6.6

defines node coordinates for element connectivity throughout the entire model geometry. As such the elements and nodes that form the crack faces and the crack tip are known before the model is solved, and the element based nodal forces can be requested from the solution outputs.

Figure 6.11 shows the mesh geometry, in which the particular elements that contain the nodes of interest are highlighted. A script was written using MATLAB™ to identify and combine the occurrences of these node forces from the output results. The method was validated through a further DCB example in which forces were extracted using the element-based, nodal forces (*nforc*) and compared to the more conventional reaction forces from symmetry constraints (Figure 6.10). The two approaches produced identical results.

6.2.3.3 Crack opening and crack sliding displacements

To obtain crack opening (COD) and crack sliding displacement (CSD) results, the displacement of the nodes that initially occupied the same co-ordinates on the opposing crack faces were recorded after loading. For the COD results, the relative opening translation of each node pair was determined along the length of the split and for each of the elements through the thickness of the 0° ply. The CSD was calculated as the relative in-plane sliding translation of the node pairs along the split length. Using a similar approach to plots of experimental COD, the crack surface within the model was

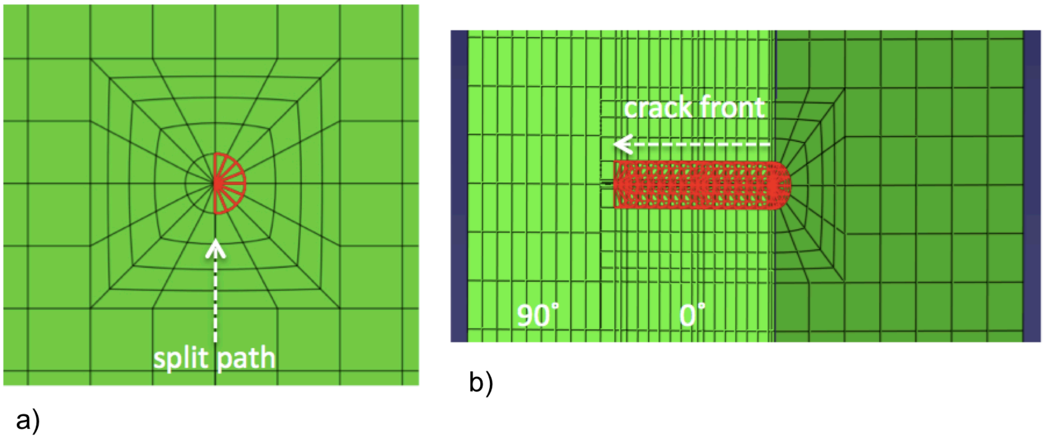

Figure 6.11: Mesh geometry showing elements required for the extraction of the element-based nodal forces using *nforc*. (a) Crack tip; (b) sectioned view along split path of crack front.

divided into four bins of equal width through the 0° ply thickness. The node pairs along the split were assigned to a bin according to their location on the crack surface. Bin 1 represents the region closest to the 90°/0° ply interface and bin 4 is closest to the 0°/0° interface. Within each bin for the ply thickness, nodes were further divided into 50 bins along the length of the split to produce grouped nodes within a grid on the crack surface. The displacement values for the nodes within each grid segment were averaged to produce single values for COD and CSD predictions at comparable points for the FE simulations.

Figures 6.12 and 6.13 show COD results and the variation in predictions for each of the model simulations in a sample loaded to 80% σ_f. Figure 6.12 shows a comparison of the benchmark model at a load of 80% σ_f with split lengths equal to: the minimum value on the crack front (simulation 1); the area averaged split length (simulation 2); the maximum observed value on the crack front (simulation 3). Each of the four curves per plot represents the position through the thickness of the 0° ply. The curve with the greatest value of COD is at the centre of the double thickness 0° ply, while the curve with the least value of COD is closest to the 0°/90° ply interface. There is little difference between the results for the three simulations. The profile of COD at the tip and the centre of the crack remains unchanged, while the COD at the root shows a very slight reduction with the longer crack front (simulation 3). This trend may be explained by the notch geometry as the effect on stress concentrations and COD in the vicinity of the notch may be dominated by the size and shape of the notch, masking the contribution from the variation in effective crack front length.

Features and mechanisms observed in the SRCT images, such as bridging, crack pinning and resin-rich regions were addressed in the FE models by adapting the benchmark simulation. A comparison of the results of these simulations is shown in Figure 6.13. Within each simulation the split length was equal to the area averaged value of 3.0 mm. The benchmark model (simulation 2) is shown in Figure 6.13a; the benchmark model with adjusted material properties to account for the toughening behaviour of the polymer precipitates in the resin (simulation 4) is shown in Figure 6.13b; the benchmark model with additional mid-ply resin rich regions (simulation 5) is shown in Figure 6.13c; the benchmark model with additional mid-ply resin rich regions and adjusted material properties (simulation 6) is shown in Figure 6.13d.

The opening displacement in the region of the crack tip remains the same for each simulation in Figure 6.13, however there are differences along the crack length and at the root. There is a smaller spread between the COD values through the thickness as the material properties are changed to incorporate the effect of the lower modulus rubber toughening phase (simulation 4). The maximum COD at the root of the crack is also larger for the simulation with amended material properties. The change in COD along the split length is greater for the simulation containing the mid-ply resin rich regions (simulation 5), however there is no change at the root. Simulation 6 includes both adjusted material properties and resin rich regions and exhibits the greatest variation from the benchmark model. The trend of the COD profile combines the effects of the two approximation approaches resulting in a plot with a more consistent gradient of opening displacement along the length of the split.

Figures 6.14 and 6.15 show the sliding displacements along the split length with each plot comprising four curves, which again represent position through the ply thickness. The combination of simulation comparisons is the same as that for Figures 6.12 and 6.13. The magnitude of the sliding displacement in comparison to the opening displacement demonstrates that the split is dominated by mode II. The sliding displacements for the change in split length/ pinning approximation show the same trend as for crack opening displacement in that there is very little change in absolute value or trend for the variations in crack length that approximate pinning (simulations 1-3). The increase in crack front length results in a very slight increase in CSD at the

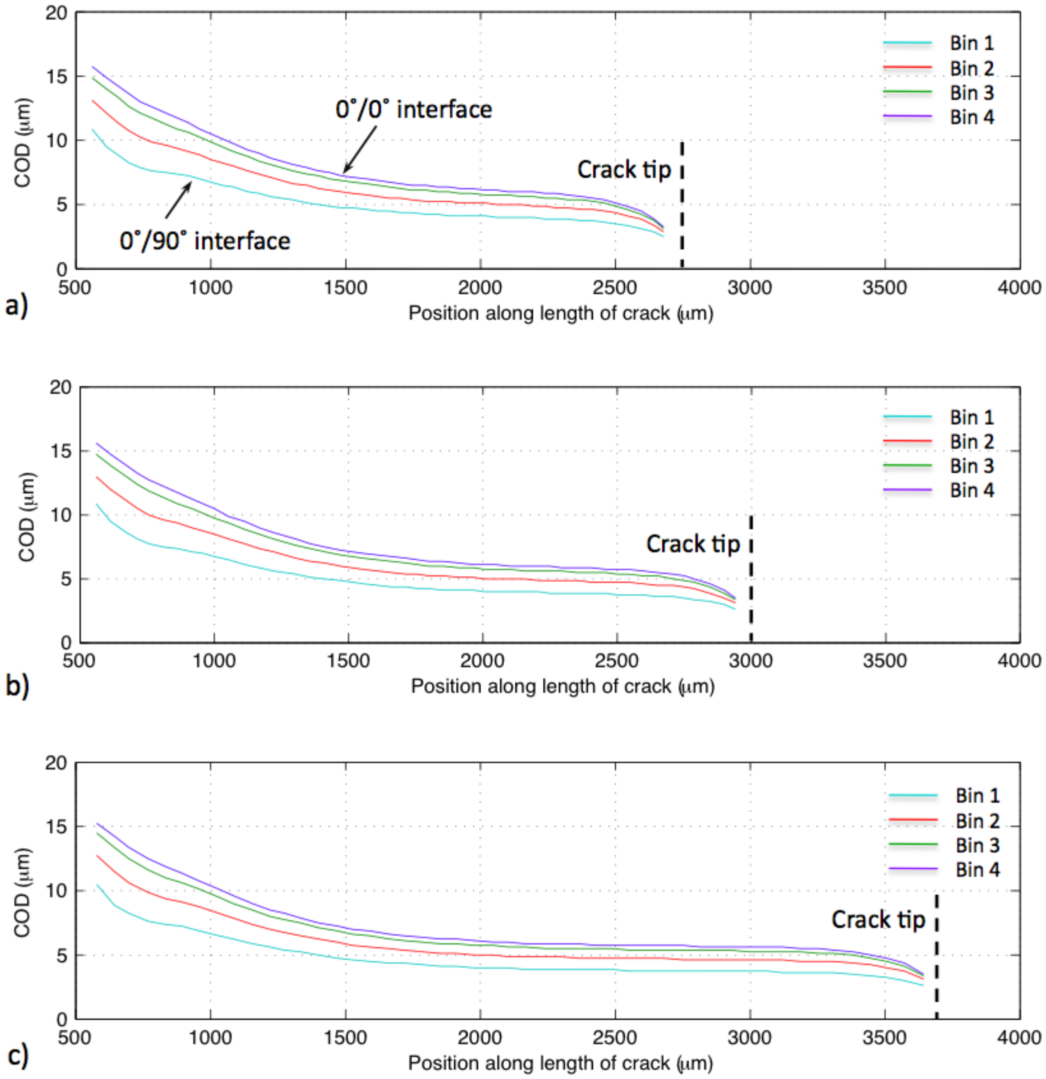

Figure 6.12: Plots of finite element model predictions for COD along 0° ply split at 80% σ_f: (a-c) simulation 1-3. Combined contribution from mechanical load and thermal residual stress.

crack root.

The comparison of simulations 4 - 6 with the benchmark model show significant differences. The mode II displacement at the crack tip remains unchanged, however each of the approximation models shows a large variation in displacement at the crack root.

Similar to the COD trends, there is a decrease in variation through the thickness when the modulus of the epoxy layers is reduced (simulation 4). There is an increase in displacement at the crack root for both the modification of the material properties (simulation 4) and the introduction of resin rich regions (simulation 5). The combination of these variations (simulation 6) results in an increase of 30% in the

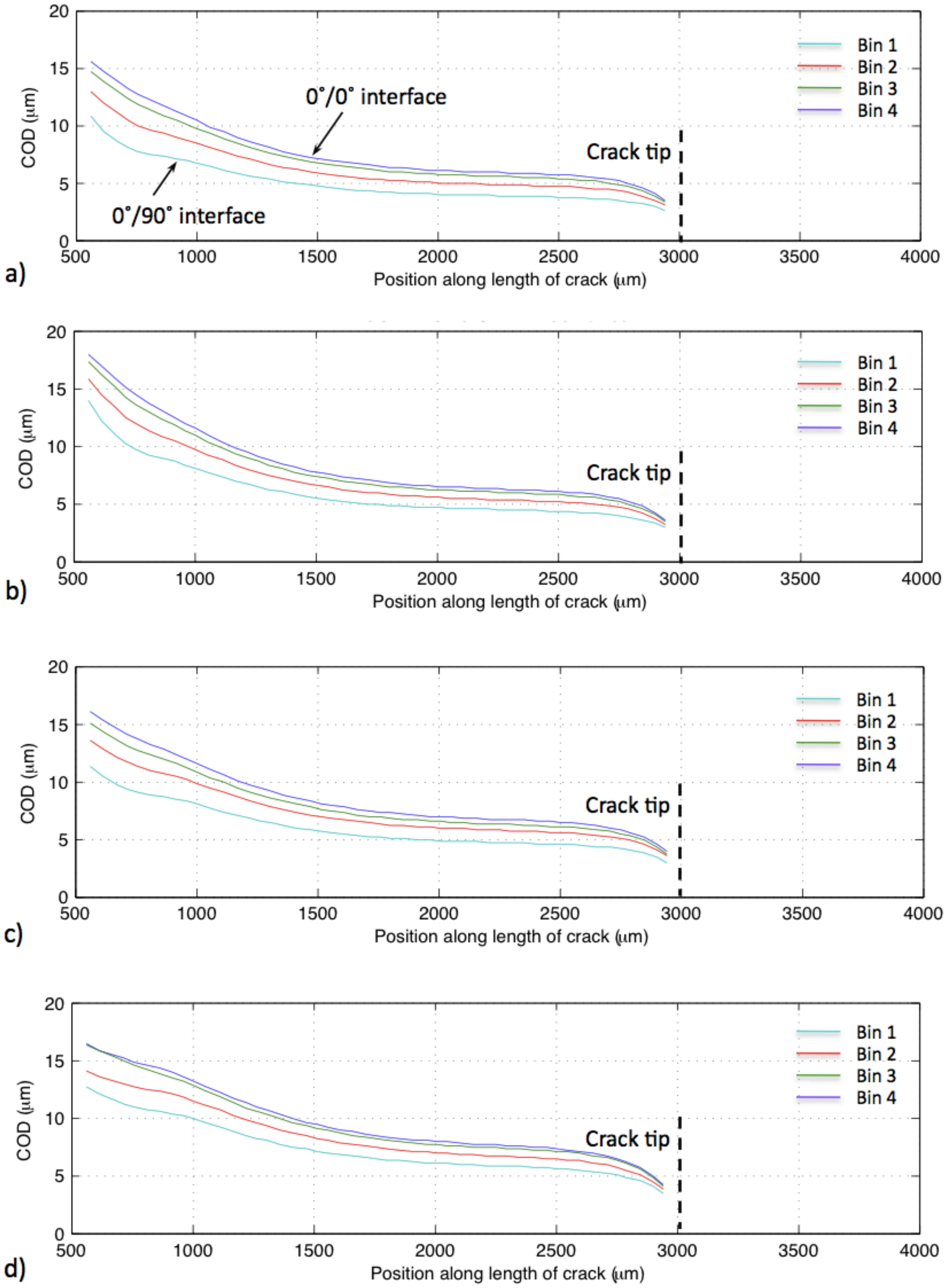

Figure 6.13: Plots of finite element model predictions for COD along 0° ply split at 80% σ_f. (a) simulation 2, (b-d) simulation 4-6. Combined contribution from mechanical load and thermal residual stress.

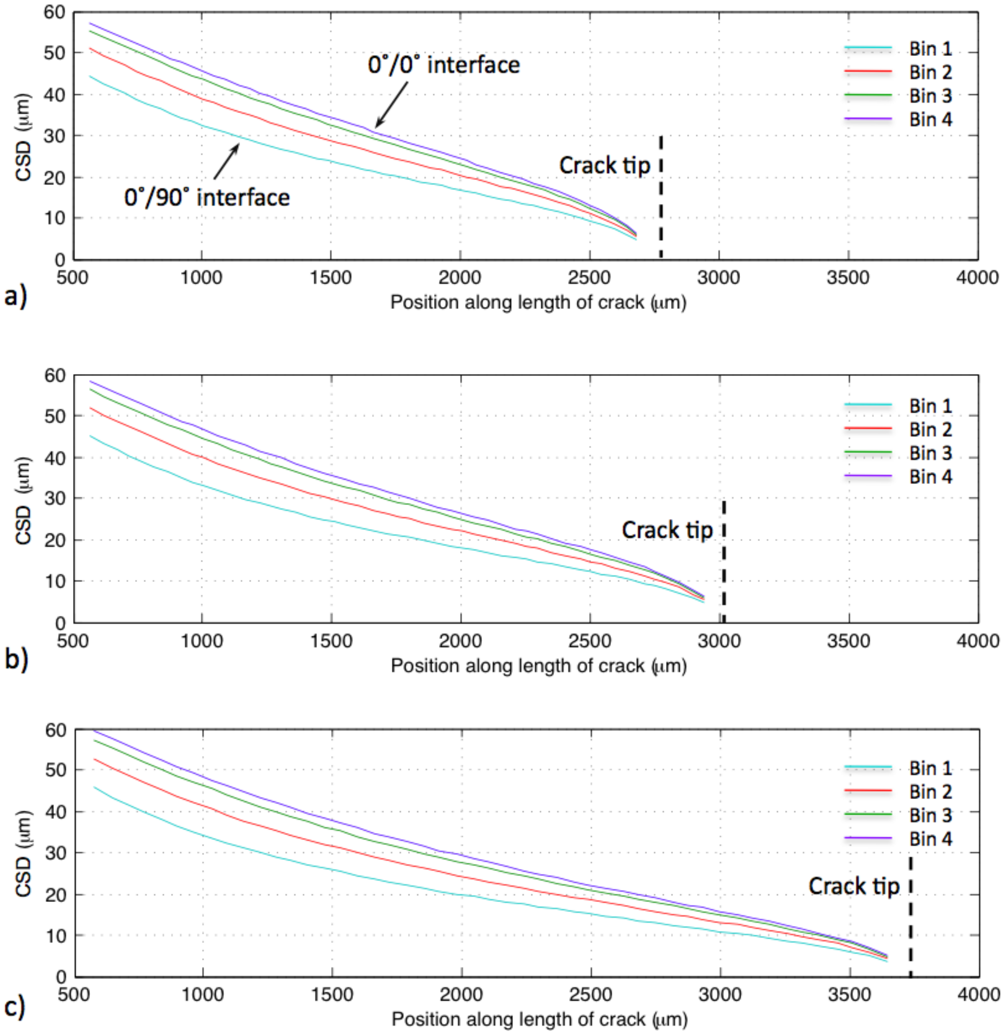

Figure 6.14: Plots of finite element model predictions for CSD along 0° ply split at 80% σ_f: (a-c) simulation 1-3. Combined contribution from mechanical load and thermal residual stress.

sliding displacement.

The CSD varies considerably through the thickness of the laminate. Figure 6.16 shows plots of CSD along the length of the split for an area averaged crack length at a load of 80% σ_f (simulation 2) at three locations through the 0° ply: at the 0°/90° ply interface, at the mid-ply region of a single 0° ply and at the 0°/0° ply interface.

The displacement is resisted by the remainder of the undamaged laminate at the 90°/0° ply interface. The contribution to the modulus of the interface from the fibre volume and the toughening particles would be expected to have a significant effect on the magnitude of CSD in this region. The gradient of the displacement profile through the thickness of the laminate is greatest close to the 90°/0° interface. At the crack root there is a decrease in CSD of approximately 40% between the 0°/90° ply interface and

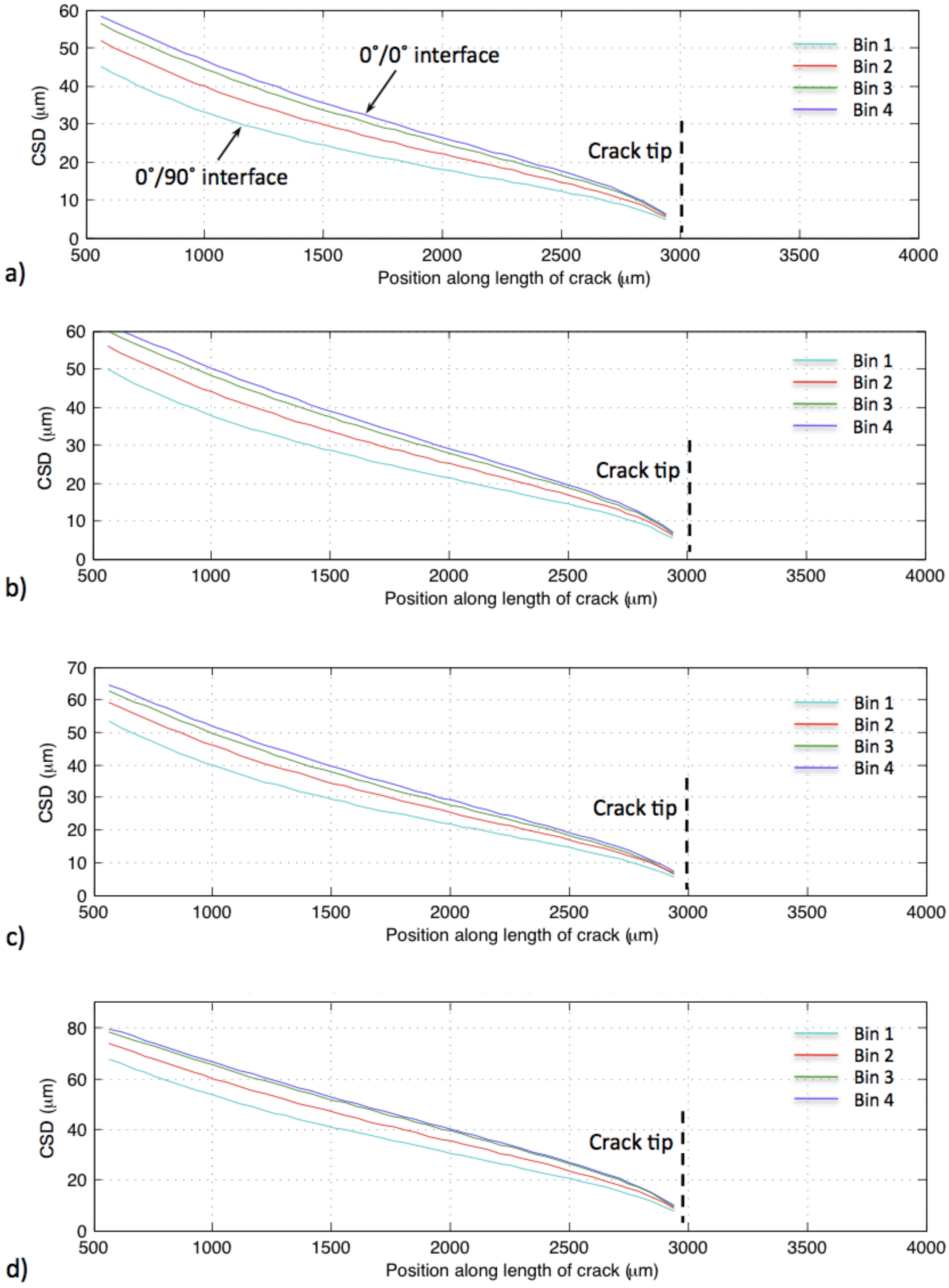

Figure 6.15: Plots of finite element model predictions for CSD along 0° ply split at 80% σ_f. (a) simulation 2, (b-d) simulation 4-6.

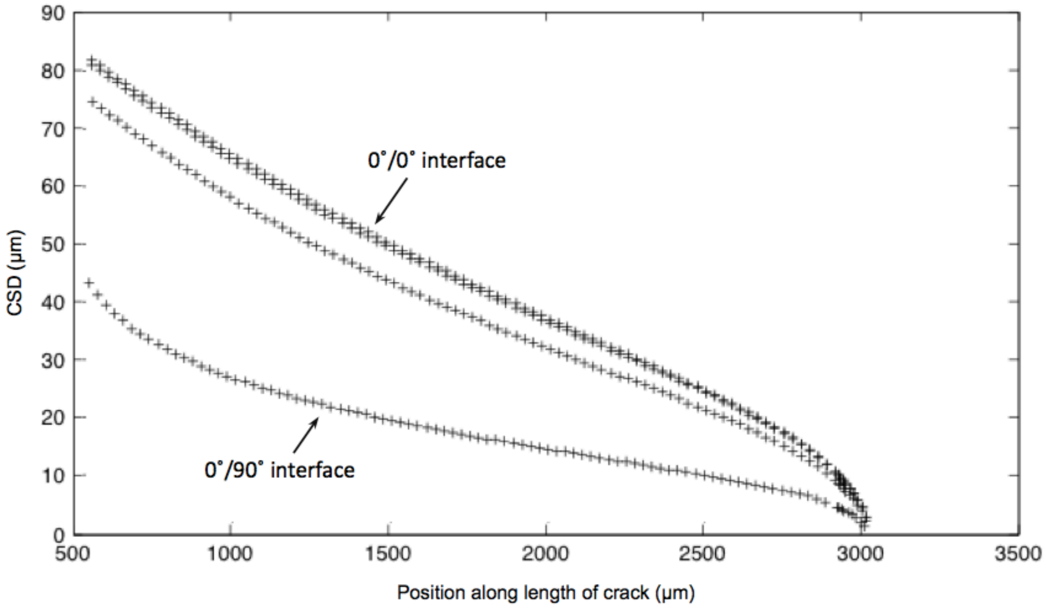

Figure 6.16: Plots of finite element model predictions for CSD along 0° ply split length at the 0°/90° interface, mid-ply region and 0°/0° interface at 80% σ_f.

the mid-ply region, compared to a decrease of approximately 7% for the remaining half-thickness between the mid-ply region and 0°/0° ply interface. The trend of the CSD along the length of the split away from the notch is similar throughout the 0° ply with very little change through the lamina thickness at the crack tip.

6.2.3.4 Strain energy release rate

Once validated, the VCCT method was applied to the benchmark model containing the 0° ply split. Figure 6.17 shows the graph of the variation in the calculated G_{II} and G_{II} with crack length for separated components of thermal residual stress and mechanical load.

As indicated by comparison of the COD and CSD results, the 0° ply split is shown to be mode II dominated. In addition, there is a mode I component to the strain energy release rate (SERR) induced by the thermal residual stresses resulting from the cure process. This is corroborated by experiment data in which approximately half of the opening displacement is accounted for in the unloaded (thermally induced) load-state [129, 130]. As the crack extends away from the vicinity and influence of the notch tip the predicted SERR becomes less sensitive to the crack length.

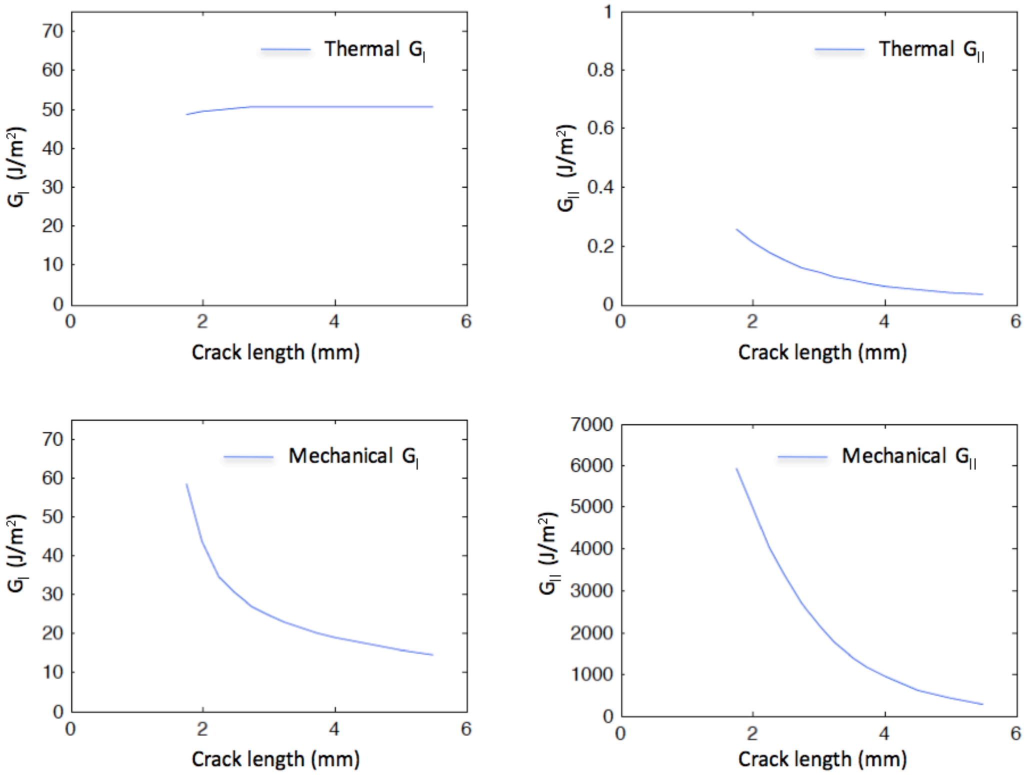

Figure 6.17: Plots of finite element model predictions for G_I, G_{II} *vs.* crack length. Mechanical and thermal contributions shown separately.

Assuming that crack growth is governed by application of the Griffith fracture criterion for the mode II component only, the strain energy release rate calculations from the model can be re-arranged and calculated to show predicted crack length versus load for a particular value of G_{IIC}. Figure 6.18 shows the predicted crack length with increasing load with G_{IIC} of 1400 Jm^{-2} [143].

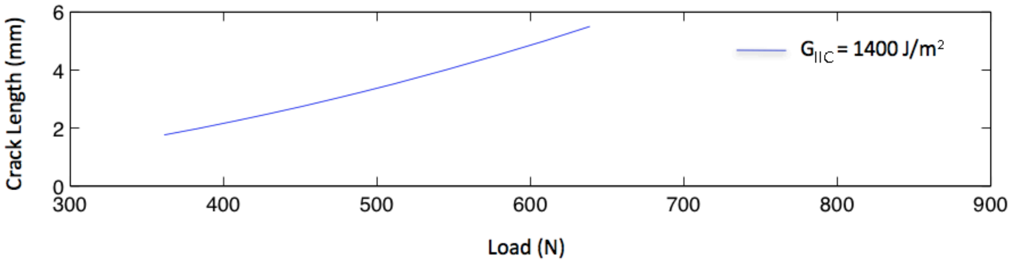

Figure 6.18: Plot of predicted crack length against applied load for constant G_{IIC}.

The VCCT technique was also applied to the modified models. Simulations 4, 5 and 6 produced a difference in mode II SERR of +30%, +9%, and +107% respectively. Crack growth occurs when local $G > G_C$ and therefore this increase in SERR would indicate a larger predicted split length for a given load and G_{IIC}.

Experiment results and model predictions show that values for SERR decrease as damage propagates within these laminates and therefore it is not necessarily valid to assume a single value of G_C to predict crack growth with load. It may be more appropriate instead to use this value to predict initial onset of damage using a mixed mode fracture criterion such as that demonstrated by Zhang *et al.* [112].

6.2.4 Model - experiment comparison

The results for crack opening and sliding displacements are similar to previous comparisons of model predictions [130], which have shown a reasonable approximation to the overall trends observed in the SRCT data. However, the absolute values of displacements vary considerably along the length of the crack with the greatest difference occurring in the region of the crack tip. The greatest variation between model and experiment data occurs with the comparison of CSD for which the model predicts values of approximately two times greater than that observed experimentally at the equivalent location through the laminate thickness. The principal reason for the variation between the model and experiment data is the difficulty in making a direct comparison between the local variations in the crack parameters in the model and the experiment data. The value of the crack length is the most evident example of this since the crack front pinning means that there is no single value that defines the crack length. The variation in crack length between the minimum observed value and maximum observed value (simulation 1 to simulation 3) does not affect the COD profile and is therefore not an adequate approach to modeling the pinning observed in the experimental results. The pinning by toughening particles in the crack wake is likely to be particularly effective at limiting crack sliding displacements. Accurate modelling of the crack opening and sliding displacements, and the resulting strain energy release rates should incorporate the pinning effect of the toughening particles directly. Conversely, the effect of the reduced elastic modulus of the rubber particle precipitates in the resin (simulation 4) has very little influence on the profile approaching the crack tip, although the crack does open more at the root. The explicitly modeled resin rich regions with baseline material (simulation 5) allows a greater range of COD through the laminate thickness due to the additional layers of material with greater compliance, however the profile remains to vary from the true results, with peak model values approximately twice that of the experimentally measured COD.

As a result of the inaccuracy in the prediction of the crack opening and sliding displacements the predictions of strain energy release rates will be in error. Consequently, the benchmark model predictions of crack length with load also result in large discrepancies with respect to the experimental data. In addition, the attempts to model the physical effects of experimentally determined mechanisms produce results with an even greater overestimation of crack length. However, the basic linear trend in crack growth with applied load, shown in Figures 6.8 and 6.18, is captured, and this suggests that a more detailed model for the effect of pinning by the toughening particles might allow for a better prediction of the experimental data.

It is also interesting to note that significant strain energy release rates are obtained for split growth in the absence of delamination. This is in contrast to previous work [31, 32, 144, 145] which used a quasi-3-D model, based on stacking of 2-D layers, which suggested that delamination was necessary to allow for splitting to occur.

6.3 Conclusion

Quantitative damage growth data have been obtained from SRCT imaging of notched carbon fibre epoxy laminate samples and used to inform the development of a model for damage growth. The effects of resin rich regions, crack front pinning and local toughening were incorporated into the model to explore the influence of these microstructural features.

The SRCT data has provided a further insight into the accumulation of composite damage, however the adjusted models have not been able to predict completely the effects of the features and mechanisms identified from the experiment results. Trends in behaviour are captured accurately, however, and there is clear evidence that a more faithful simulation of the microstructure would lead to a more accurate prediction of damage growth.

There are many local micro-mechanisms and microstructural features that affect crack growth. The crack morphology in resin rich regions differs from high fibre density regions, with accompanying variations in fibre bridging and de-bonding of the rubber toughening particles in the matrix. Key features are apparent on inspection of SRCT data. Crack pinning and bridging in the form of echelon cracks initiated by toughening particle de-bonding are examples of a local variation in fracture toughness arising from local microstructural inhomogeneities. The laminate is modelled using elements with homogenous orthotropic material behaviour and does not account for the microstructural effects such as pinning and the fibre/matrix interface at the location of the splits. It is believed that these inhomogeneities must be modelled explicitly, and that simple approximations are not capable of accounting for the accumulated effects of the interacting damage mechanisms. Future work should aim to encompass local variations in the laminate properties and include the shape of the crack front in the model.

The work presented herein provides key insights as to the features that need to be included in any micromechanical description of composite damage, and provide a first step in the utilisation of high fidelity computed tomography data to inform such models. The richness of such data opens up the possibility of ‘data rich mechanics’ in which models for material response can be completely calibrated to the local micromechanical behaviour.

CHAPTER 7

MODELLING THE EFFECTS OF CRACK PINNING IN A TOUGHENED COMPOSITE MATRIX

This chapter describes the development of the model to control the crack front geometry for the 0° ply split to simulate the observed crack pinning from SRCT data. The predicted effects of pinning on crack opening displacement, sliding displacement and crack length with load in the model are compared to the experimental results in Chapter 6, and the limitations of the modelling approach are discussed. The experimental results are identical to those described in Chapter 6; however the qualitative observations focus here on the mechanisms involved in pinning. As such, the process by which the results were obtained is included for continuity but is limited to a brief overview and the quantitative results are included in a model-experiment comparison for review. SRCT post-processing for quantitative experimental results and segmented images of damage was carried out by Mark Mavrogordato [21].

Progressive damage in laminated, double edge notched carbon fibre-epoxy $[90/0]_S$ composites has been recorded using *in situ* synchrotron radiation computed tomography (SRCT). Quantitative measurements of damage accumulation including crack opening and sliding displacements around cracks and delaminations have been obtained for tensile loads ranging from 30% nominal failure stress to failure. In addition to previous work in which a 3-D finite element (FE) model was constructed to predict crack opening behaviour, sliding displacements and strain energy release rate to predict crack growth with load, the pinning in a 0° ply split caused by local toughening effects has been explicitly simulated. The crack pinning model further explores the sensitivity of the model-experiment comparison in which particular microstructural features or properties of a laminate have a direct effect on local fracture toughness and damage growth.

7.1 Introduction

Laminated carbon fibre-epoxy composites are subject to a number of failure mechanisms under tensile loading conditions; these predominantly include 0° ply splitting, transverse ply cracks, delamination, and ultimately fibre rupture [27–30, 146]. Accurate representation and prediction of the accumulation of damage requires a model that incorporates an appropriate representation or approximation of the interacting fracture processes. While there are a large number of models within the literature that compare well to the experimental behaviour of particular laminate configurations and loading regimes, it is widely acknowledged that there is no single model that captures the fundamental interactions of composite failure such that accurate predictions can be made for laminate response across a significant spectrum of load cases, material systems and laminate stacking sequences [11]. For industrial or commercial applications, little confidence is afforded for component design without additional reassurance from a large array of physical tests [2]. Modelling approaches that apply a local homogenisation of material behaviour and microstructural features, such as cohesive zone modelling, have demonstrated an ability to simulate damage initiation and progression in generic composite structures [17]; however these models first require calibration of element behaviour from physical experiments and material characterisation. An understanding of the effect on material properties of the local variation in microstructure and mechanisms is therefore vital to implement appropriate behaviour laws to such models.

This paper extends a previous study of the application of synchrotron radiation computed tomography (SRCT) to characterise full field damage accumulation, resolving mechanisms such as cracks and fibre breaks to less than 1 μm in size [125, 128–130, 135, 136, 140, 141] and the use of this experimental data to inform the construction of a 3-D finite element model. This work reported the evolution of damage in a notched cross-ply laminate subjected to uni-axial tension, and the influence on crack morphology of particular microstructural features and mechanisms such as crack bridging in resin rich regions with rubber toughening precipitates. The model included a sensitivity study of the effects of these features and compared particular damage parameters (crack opening, sliding displacement and crack growth with load) to quantitative experimental measurements. A principal conclusion regarding that model related to the effect of the difficulty in making direct model-experiment comparisons for crack lengths since toughening mechanisms and local microstructure give rise to significant pinning of the crack front through the ply thickness. The present work has been further developed from the initial model that contained a split with a single area averaged crack length to include a geometrically non-linear crack front corresponding to the experimentally observed pinning in the 0° ply split. In addition to COD and CSD predictions, the resultant change in strain energy release rate (SERR) at the crack tip has been calculated using the virtual crack closure technique (VCCT) [115] to investigate the effect of pinning on model predictions and to consider toughening due to local features when developing models that incorporate homogenised elements.

The experimental results presented in this paper are taken from data sets reported in Chapter 6, which are available for public access at the University of Southampton Materials Data Centre [139].

7.2 Results and discussion

7.2.1 Experimental results

The SRCT technique provides data in the form of high-resolution 3-D images of the specimen under test allowing internal damage and micro-structural detail to be observed and measured with an exceptional level of fidelity and confidence. The images consist of a 3-D array of grey-scale values corresponding to the local X-ray absorption coefficient of the material. In addition the phase contrast conditions result in the presence of a bright fringe where a change in phase occurs, for example at the interface between continuous material and air that constitutes a crack. Figure 7.1 shows a maximum intensity projection (MIP) of the notched region of a $[90/0]_S$ laminate at a load of 80% σ_f in which vertical splits in the central 0° plies, horizontal transverse ply cracks in the outer 90° plies, and the texture of the notch are readily identified.

Microfocus CT was used to obtain this image, therefore zinc iodide was required to provide the contrast to resolve the damage at the crack surfaces. All subsequently reported results were obtained using SRCT for which zinc iodide was not used.

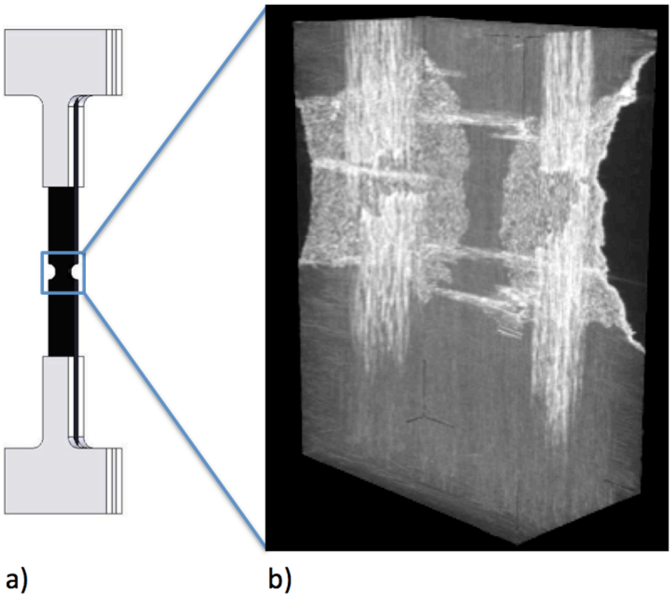

Figure 7.1: Damage in a $[90/0]_S$ M21/T700 specimen loaded to 80% σ_f. (a) Schematic of specimen; (b) MIP of notched region.

Post-processing using ImageJ™, MATLAB™ and VG Studio Max 2.0™ was carried out to visualise, segment and quantify features of interest such as cracks, delaminations, fibre bridging, fibre breaks and de-cohesion of rubber toughening precipitates in resin rich areas [128, 140, 141]. Figure 7.2 shows a 3-D rendering of the notched region at a load of 90% σ_f in which splits, transverse ply cracks and delaminations have been identified and segmented.

The split profiles shown in Figure 7.2 can be quantified to produce crack opening displacement (COD) plots of the damage [128]. Figure 7.3 shows COD plots of a growing 0° ply split between load steps of 65%, 80% and 90% of the nominal failure strength.

The 3-D nature of SRCT volume reconstruction enables high-resolution analysis of the specimen at a particular region of interest. For example, interrogation of sequential 2-D slices through the volume reveals that the local microstructure is responsible for the crack pinning observed in the COD plots in Figure 7.3. Figure 7.4a shows a binarised plot of the data shown in Figure 7.3c to reveal the outlined profile of the crack. A 2-D slice through the volume at a position of 3250 μm along the split length is shown in

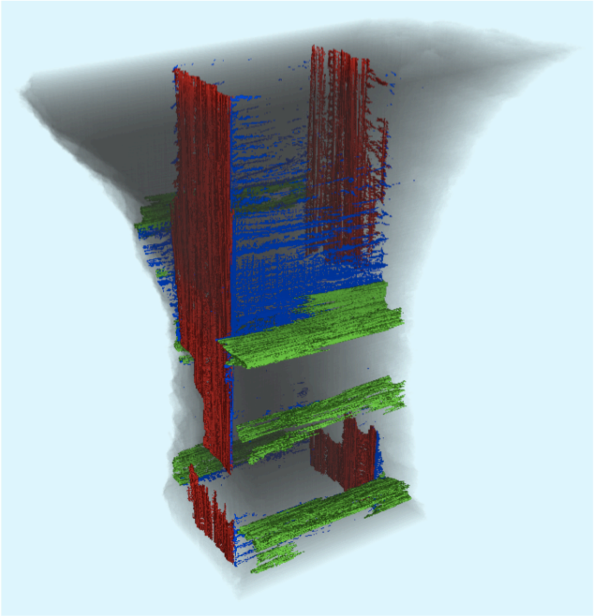

Figure 7.2: 3-D SRCT visualisation of damage in a notched $[90/0]_S$ laminate at a load of 90% σ_f. Damage consists of 0° ply splits (red), transverse ply cracks (green) and delaminations (blue) [141].

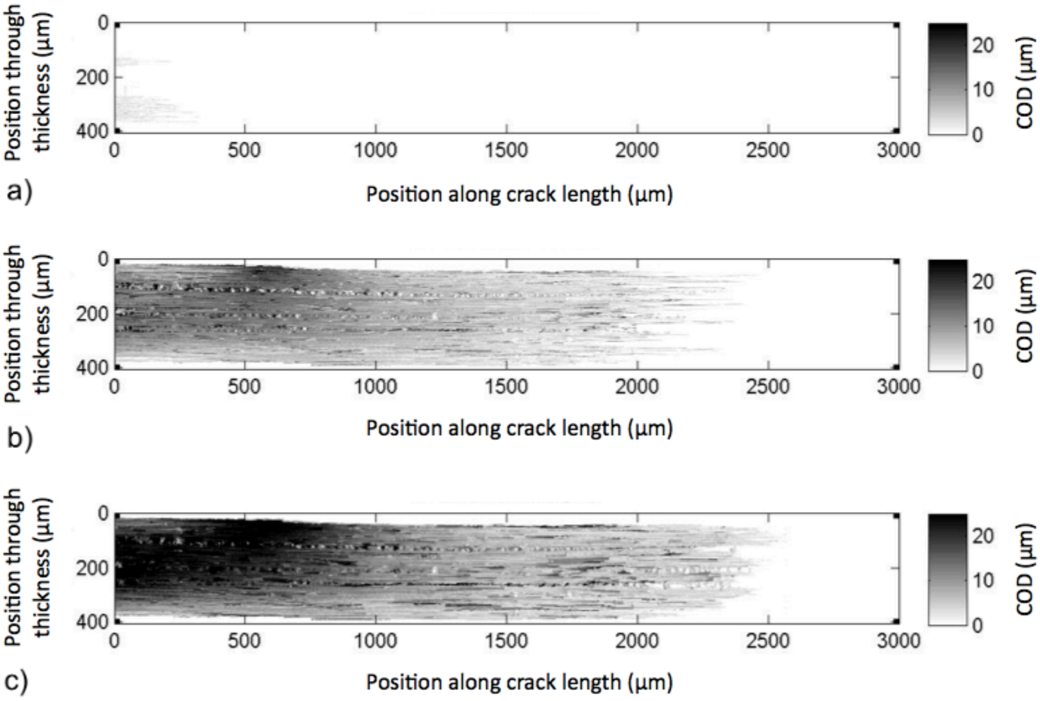

Figure 7.3: Crack opening displacement plots of 0° ply split growth between incremental load steps. (a) 65% σ_f; (b) 80% σ_f; (c) 90% σ_f.

Figure 7.4b. Near its tip, the crack is abruptly arrested in the mid-ply resin rich regions where the density of rubber toughening particles is greatest. The resin rich regions appear at the interface between two adjacent plies, resulting in three corresponding resin toughened regions in the central 0°/0° ply surfaces and two regions at the 90°/0° ply interfaces. Crack bridging between fibres is also observed at the crack tip where the opening displacement is not sufficient to overcome the bridging tractions. The variation in fracture toughness through the laminate gives rise to the crack front shown in Figure 7.4a. In the remainder of the present paper the effects of the crack front behaviour are simulated in the model and the results are compared to the SRCT measurements.

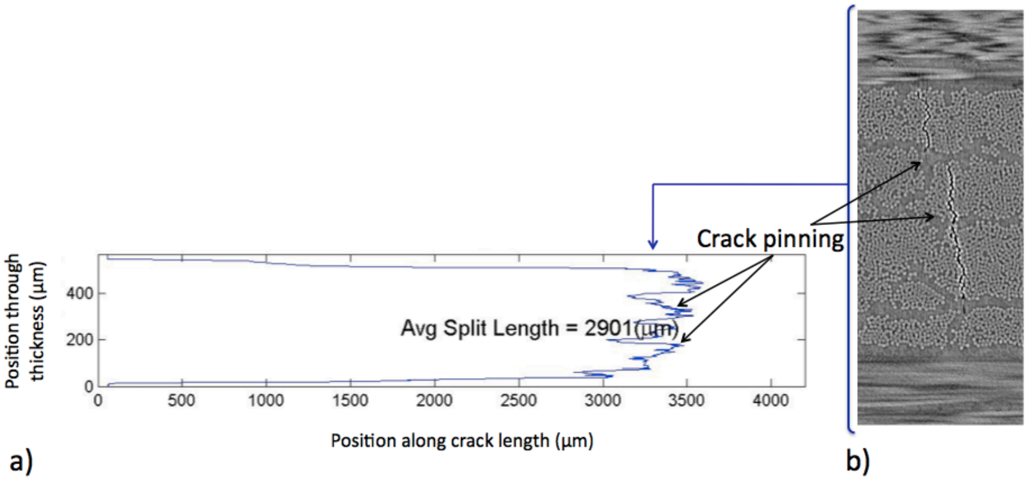

Figure 7.4: Experimentally measured COD extracted from SRCT data. (a) Outlined profile of 0° ply split at 90% σ_f; (b) 2-D slice at position of 3250 μm along split showing resin rich regions corresponding to locations of crack pinning.

7.2.2 Finite element model

7.2.2.1 Model construction

For this work the damage in 0° plies alone is modeled. Future work will include other types of observed damage such as transverse ply cracks and delaminations, however in the first instance the representation of damage in the 0° ply represents a simplified benchmark against which to compare the performance of this modeling approach. The model was implemented using ABAQUS™ and is based on the construct described in previous work [130]. Quadratic, hexahedral, elastic elements of type 3D20R were used to create a mesh with three planes of geometrical symmetry allowing a model of 1/8$^{\text{th}}$

of the specimen volume to be specified with appropriate boundary conditions for the nodal degrees of freedom. Eight layers of elements were used to model each ply through the thickness, with a refined mesh at the crack tip. Duplicated nodes for neighbouring elements along a pre-determined path were used to embed a split in the 0° ply. The location and split length was specified to reproduce the damage conditions observed in the experimental data. A load was applied using an enforced displacement and, since the simulation is linear-elastic, the appropriate scaling factor was applied to the model outputs based on the ratio of the experimentally applied load to the model reaction force at the symmetry constraints. Crack opening and shear results were calculated as the difference in mode I and II displacements at each of the node pairs for all elements along the length of the split and through the thickness of the 0° ply. To enable comparison with the experimental results from the loaded and unloaded SRCT data, the components of displacement due to thermal residual stress and due to mechanical loading were separately determined in the post-processing stage of the model analysis. The plots of COD and CSD for the experimental data and model predictions were produced using the binning and averaging method described in Chapter 6. The displacement field on the surface of the crack flanks was divided into bins of equal area along the crack length and through the ply thickness. Displacement values within each bin were averaged to reduce the continuous 2-D data to a single curve per bin. Bin 1 corresponds to a position closest to the 0°/90° interface, and bin 4 corresponds to a position closest to the 0°/0° interface. The material properties for each ply were based on the manufacturer's published data sheets and are described in Table 7.1 [124].

Table 7.1: Material property constants used to define M21/T700 carbon fibre-epoxy composite in the fibre direction for finite element modelling.

Young's modulus E (GPa)	Poisson's ratio ν	Shear modulus G (GPa)	Thermal coefficient of expansion α ($10^{-6}K^{-1}$) [a]
$E_{11} = 148.0$	$\nu_{12} = 0.35$	$G_{12} = 3.8$	$\alpha_{11} = -1.0 \times 10^{-3}$
$E_{22} = 7.8$	$\nu_{13} = 0.35$	$G_{13} = 3.8$	$\alpha_{22} = 34.0$
$E_{33} = 7.8$	$\nu_{23} = 0.35$	$G_{23} = 2.9$	$\alpha_{33} = 34.0$

[a] Stress free temperature of 180 °C

Figure 7.5 illustrates the model geometry, lay-up and crack front shape with respect to a schematic of the sample and the SRCT volume. Figure 7.5a shows the schematic of the sample with aluminium end tabs for load transfer in the load rig. Figures 7.5b and

7.5c provide a comparison between the crack fronts in the SRCT data and the model and Figure 7.5d illustrates the trajectory of the crack front for pinning in the mid-ply resin rich region. While it is apparent that the model crack front does not match exactly the shape of the observed crack front, it represents an initial approximation to the pinning behaviour observed in all the specimens tested experimentally for comparison with the experimental results.

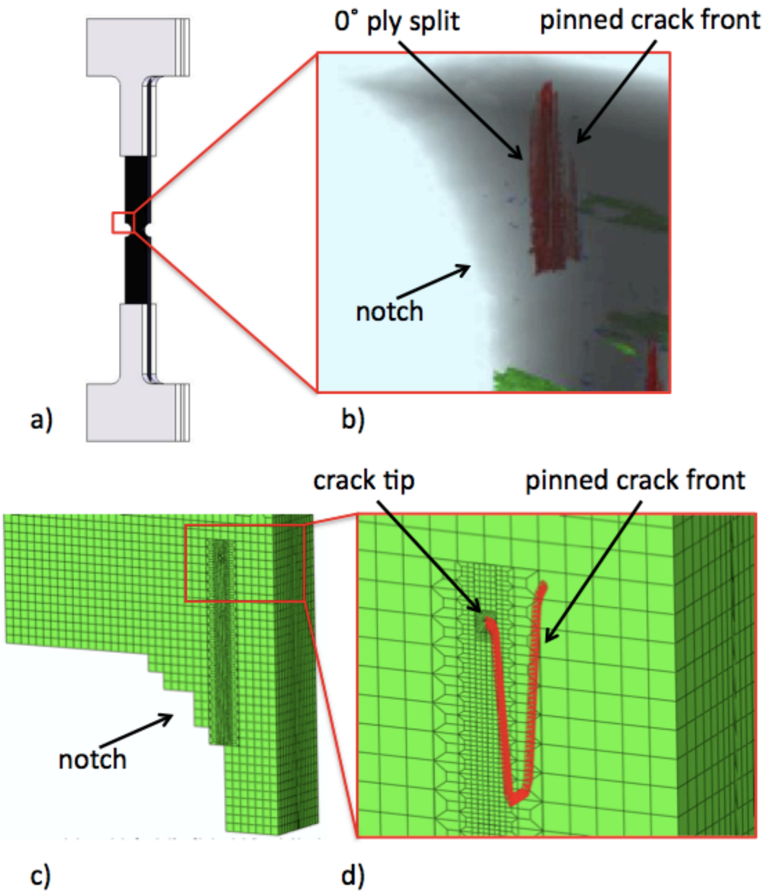

Figure 7.5: Finite element model representation of a 0° split within a $[90/0]_S$ specimen. (a) Sample schematic; (b) segmented 0° ply split from SRCT data showing crack pinning; (c) FE model showing crack path; (d) FE model crack front trajectory.

7.2.2.2 Effect of model construction

The pinned model construction requires a different meshing approach to that of the un-pinned model presented in previous work due to the path of the nodes and the connections that define the crack front trajectory elements. The pinned crack front geometry was constructed using ten separate segments of elements; with adjacent surfaces of each segment connected using tied surfaces. To determine the effect of the pinned construction on the mesh behaviour, a model employing the pinned construction was produced with the length of the pinned front set to zero for comparison with the equivalent un-pinned model.

Figures 7.6 and 7.7 illustrate that the use of tied surfaces in place of direct node connectivity results in a mesh with significantly reduced stiffness. COD is plotted along the length of the split at a load of 80% σ_f for the un-pinned model (Figure 7.6a) and for the pinned model with zero pinned length (Figure 7.6b). Figure 7.7 shows the equivalent results for CSD. The effect of the tied surfaces on the mesh behaviour should be addressed in future modelling work to eliminate the reduction in stiffness. However, where comparison is made between the pinned and un-pinned model predictions described in the present work, the un-pinned model data will be obtained from the mesh with tied surfaces and benchmark simulation parameters described in Chapter 6.

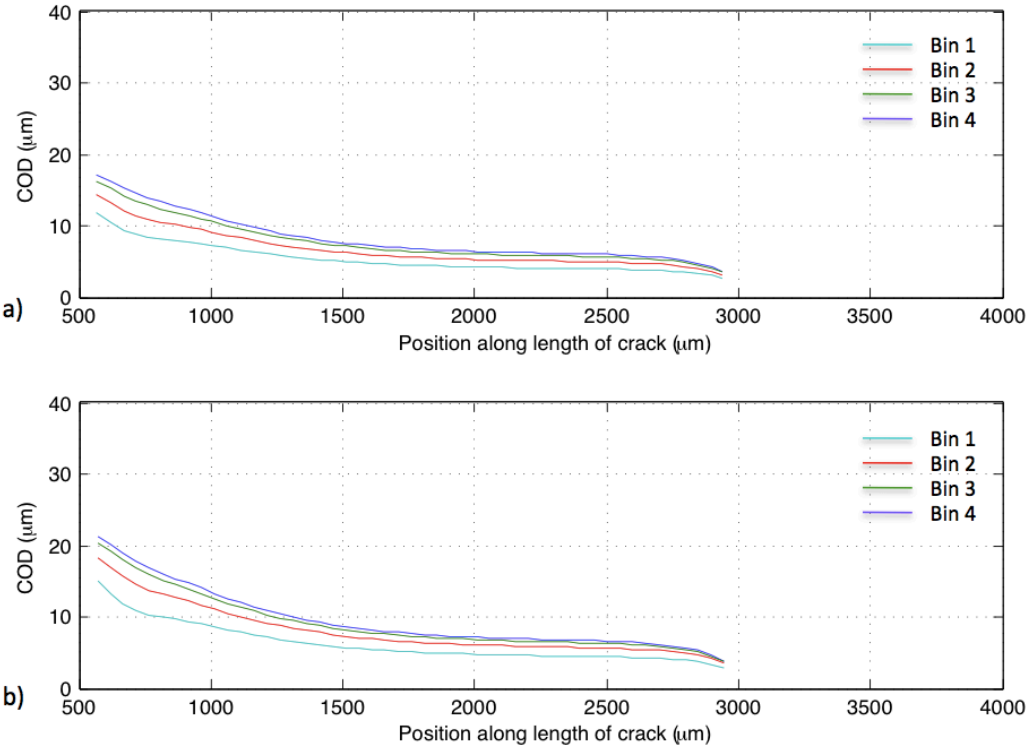

Figure 7.6: Plots of finite element model predictions for COD along the split length at 80% σ_f. (a) Un-pinned model; (b) pinned model with zero pinned length. Combined contribution from mechanical load and thermal residual stress.

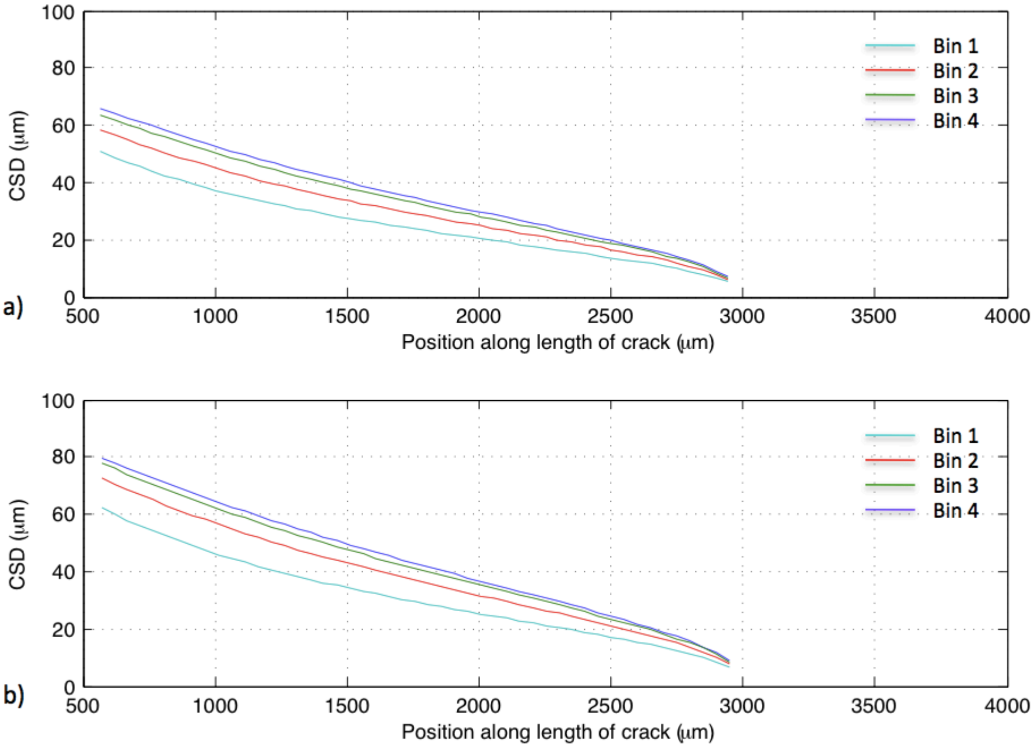

Figure 7.7: Plots of finite element model predictions for CSD along the split length at 80% σ_f. (a) Un-pinned model; (b) pinned model with zero pinned length. Combined contribution from mechanical load and thermal residual stress.

7.2.3 Model - experiment comparison

7.2.3.1 Crack opening displacement

Figure 7.8 shows plots of COD against crack length at 80% σ_f for the un-pinned model predictions (Figure 7.8a), the pinned model predictions (Figure 7.8b), and the corresponding experimental results (Figure 7.8c). The overall trend of COD for the un-pinned model compares reasonably well with the experimental data in the central region of the split, however there is a considerable variation in absolute values at the crack root and crack tip. Within the pinned model, the trend of COD approaches a more accurate comparison with the experimental results, in particular the variation of opening at the root, and the gradient at the tip, however the model significantly over-predicts the magnitude of the COD.

Further comparison is made in Figure 7.9 in which the separated contribution from thermal and mechanical loading is identified. When compared to the benchmark model for mechanical loading, the pinning introduces a more pronounced variation in COD

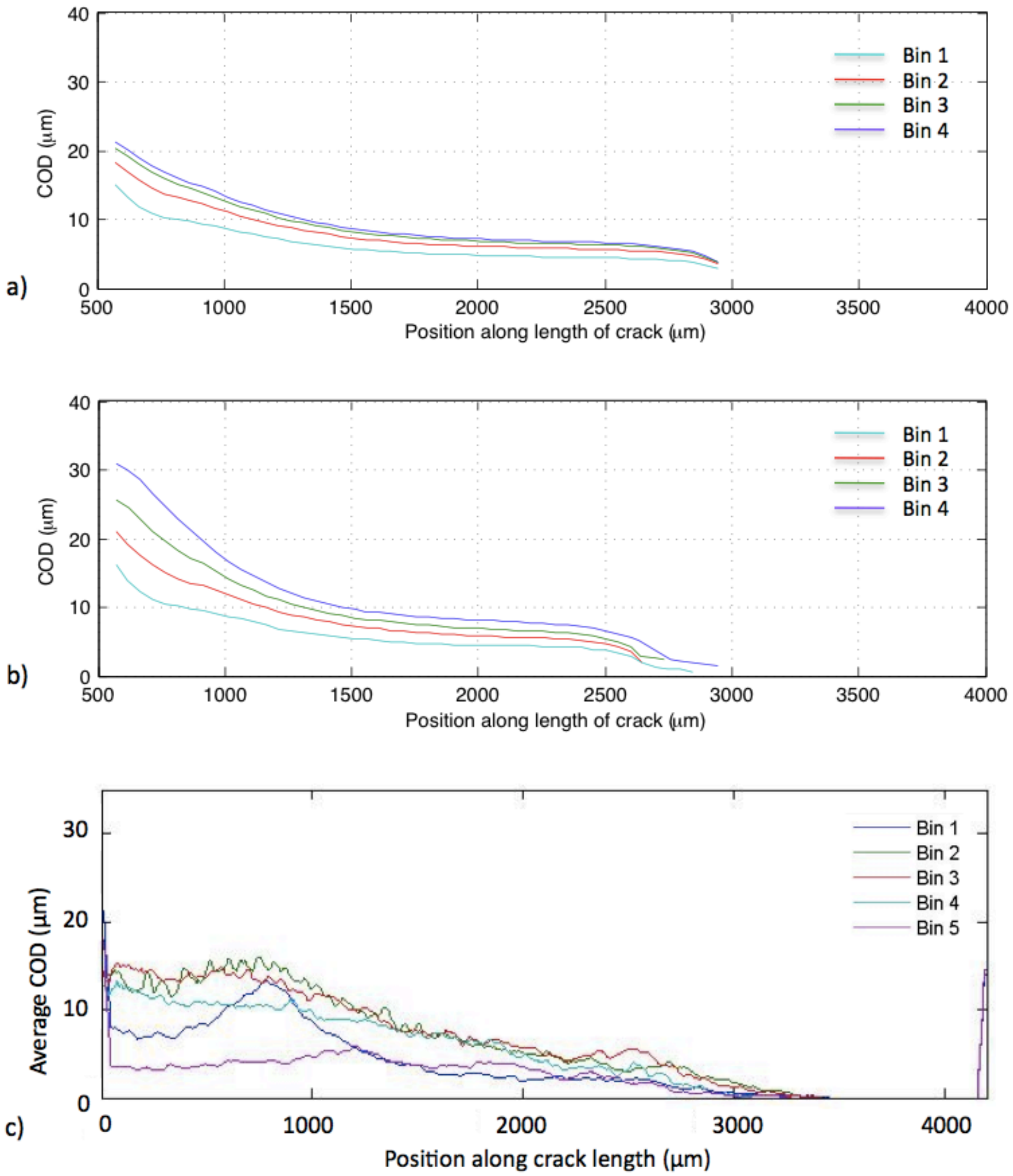

Figure 7.8: Plots of finite element model predictions and experimentally measured COD along the crack length at 80% σ_f. (a) Benchmark model with no pinning; (b) model with pinned crack front; (c) experiment results. Combined contribution from mechanical load and thermal residual stress.

through the laminate thickness at the crack root. Although this trend correlates more accurately to the experimental data the magnitude of the variation exceeds the maximum recorded value at the crack root by a through-thickness average of approximately 300%. The thermal contribution to the total opening displacement accounts for a significant proportion of the total COD, and the comparison between experiment and model shows a more accurate prediction both in trend and magnitude, however the variation in thermal opening through the thickness of the laminate is more uniform in the model than that of the experiment results.

Figure 7.10 shows the variation in COD for the pinned model predictions as the load is increased, with crack length corresponding to experimental observations for each load. Although the intervals of approximately 10% σ_f between load steps provides an insight into damage progression, further refinement would be required to capture sufficient data for comparison between loading steps as it was found that the majority of 0° ply splitting occurred between 70% and 80% UTS.

Similar to the predictions for the un-pinned model in Chapter 6, the displacement at the crack root varies little with increasing load and crack length. The mesh construction along the split path varies considerably from that of the model in Chapter 6, however the mesh in the region of the notch is identical, providing further evidence that the stress state at the crack root may be dominated by the notch geometry. Future models should explore the effect of the model construction on stress concentrations near the crack root.

7.2.3.2 Crack sliding displacement

The experimental measurements of sliding displacement were obtained by the identification and tracking of aluminium particles embedded between the laminate plies during manufacture. Since the particles were distributed at the ply interfaces only, the full profile of sliding displacements is not accounted for, and it is not possible to make a complete through-thickness comparison with the experimental data. The bulk of the measurements were close to the 0°/90° ply interface where the shear strain is resisted by the ply orientation mis-match and the experiment shear data therefore represents the lower limit of displacement. A comparison of the CSD at the 0°/90° ply interface

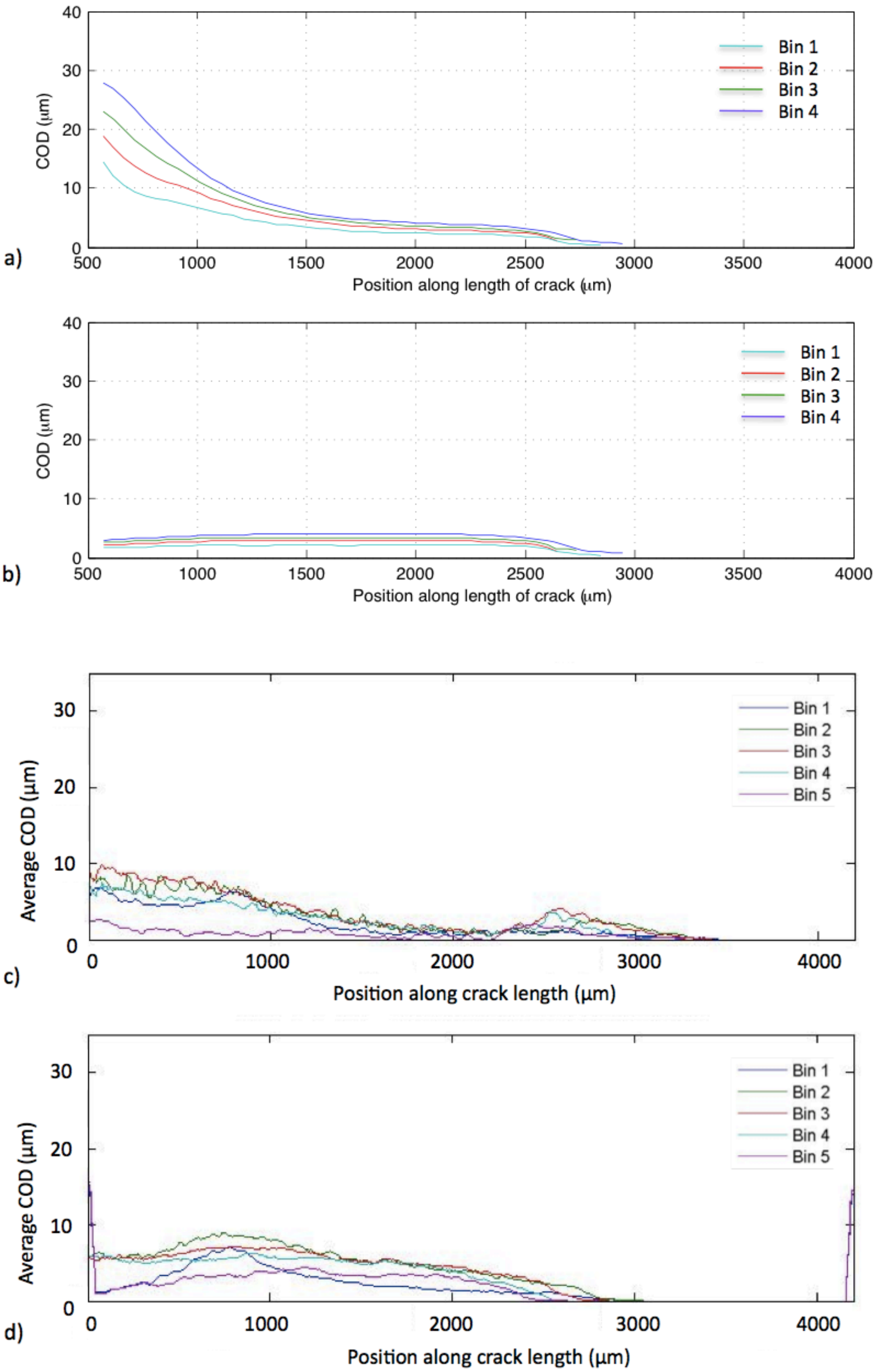

Figure 7.9: Plots of mechanical and thermal contribution to finite element model predictions and experimentally measured COD along the crack length at 80% σ_f. (a) Pinned model mechanical contribution, (b) pinned model thermal contribution, (c) experimental mechanical contribution, (d) experimental thermal contribution.

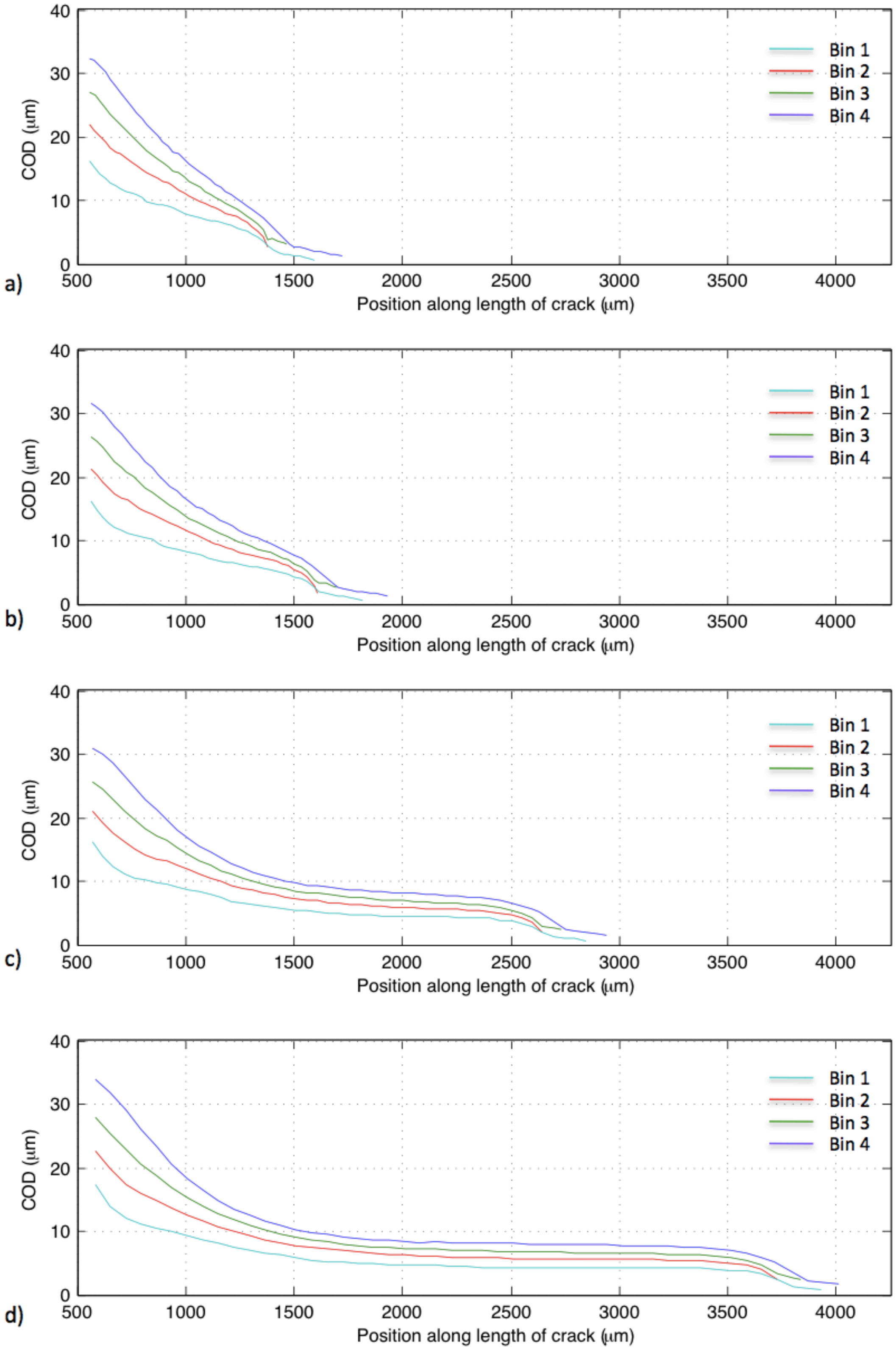

Figure 7.10: Plots of pinned finite element model predictions for COD along the crack length. Curves correspond to loads of: (a) 65% σ_f, (b) 70% σ_f, (c) 80% σ_f, (d) 90% σ_f. Combined contribution from mechanical load and thermal residual stress.

for the pinned model, un-pinned model and experiment data is shown in Figure 7.11 for a load of 80% σ_f.

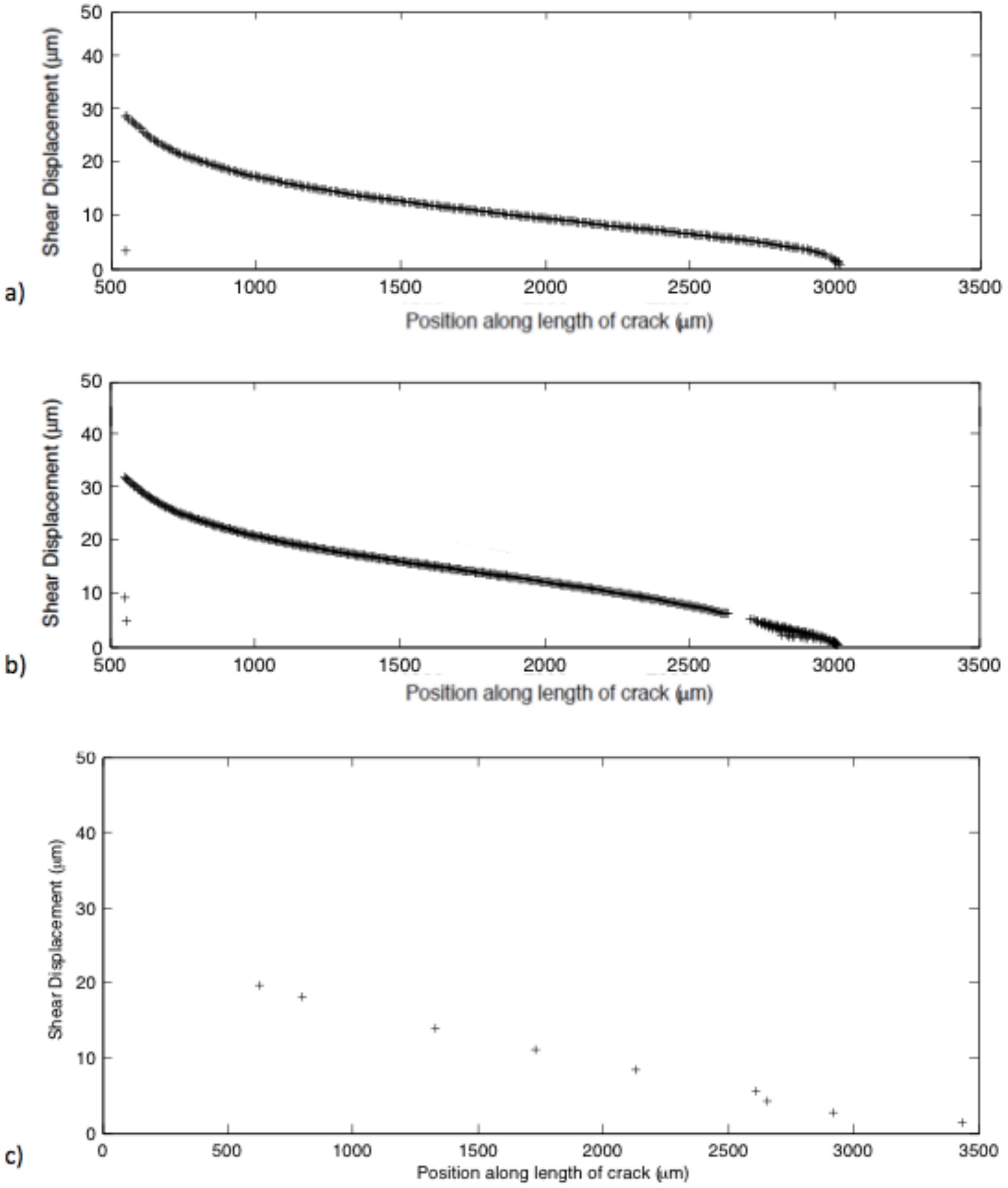

Figure 7.11: Plots of finite element model predictions and experimentally measured sliding displacement along the crack length at 80% σ_f. (a) Benchmark un-pinned model, (b) pinned crack front model, (c) experiment results. Combined contribution from mechanical load and thermal residual stress.

The approximately linear trend of the predictions for both models in the central region of the split is in good agreement with the experiment, with strong correlation between the absolute values. The gradient of the curve at the crack tip and crack root is slightly reduced in the pinned model, with an increase of approximately 25% in the central section of the split. The contribution to the effective compliance from resin rich regions, rubber toughening precipitates, transverse ply cracking and delamination would be significant in this region and these micromechanical details must therefore be accounted for in future work.

Figure 7.12 shows the profile of CSD through the thickness of the 0° ply. The plot of CSD at the 0°/90° interface correlates well with the experimental results and, consistent with the model predictions in Chapter 6, the gradient of the displacement profile through the thickness of the laminate is greatest close to the 90°/0° interface. The significant change in displacement through the thickness of the 0° ply accounts for the difference between the binned model predictions and the experimental data at a single through-thickness location and demonstrates the importance of the ability to obtain accurate full field measurements of experimental data for comparison with models.

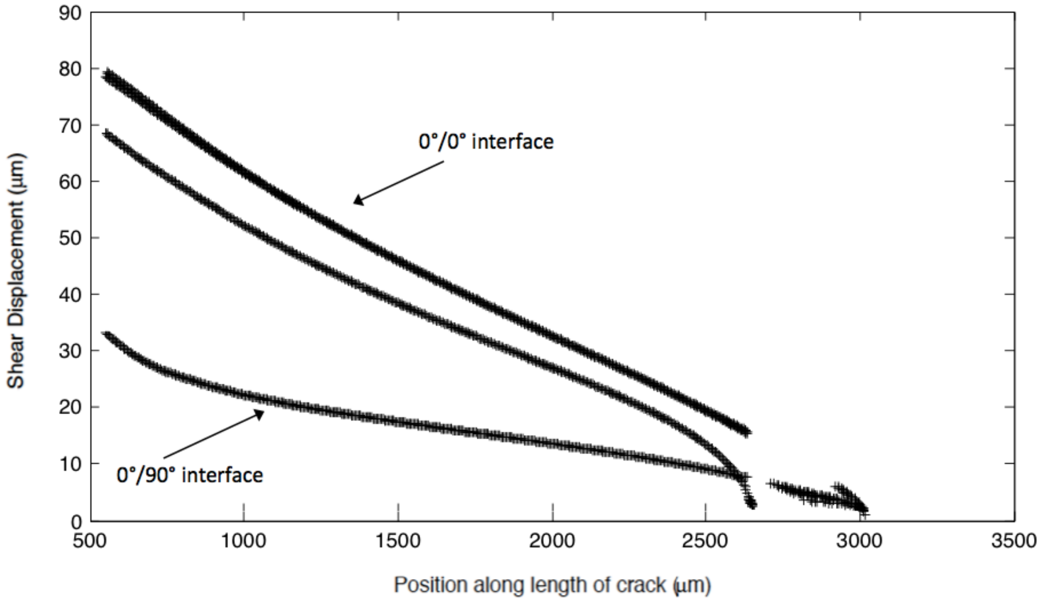

Figure 7.12: Plot of experimentally measured sliding displacement along the crack length at a load corresponding to 80% $\sigma_f$for the pinned model at the 90°/0° ply interface, mid-ply region, and 0°/0° ply interface. Combined contribution from mechanical load and thermal residual stress.

Figure 7.13 shows the change in CSD with increase in load and crack length for the pinned model. In contrast to the mode I opening displacement which showed no change at the crack root between load steps, the CSD increases significantly as the crack extends.

The curves of CSD against crack length remain generally linear with a similar gradient as the crack extends, however the variation through the thickness between the binned

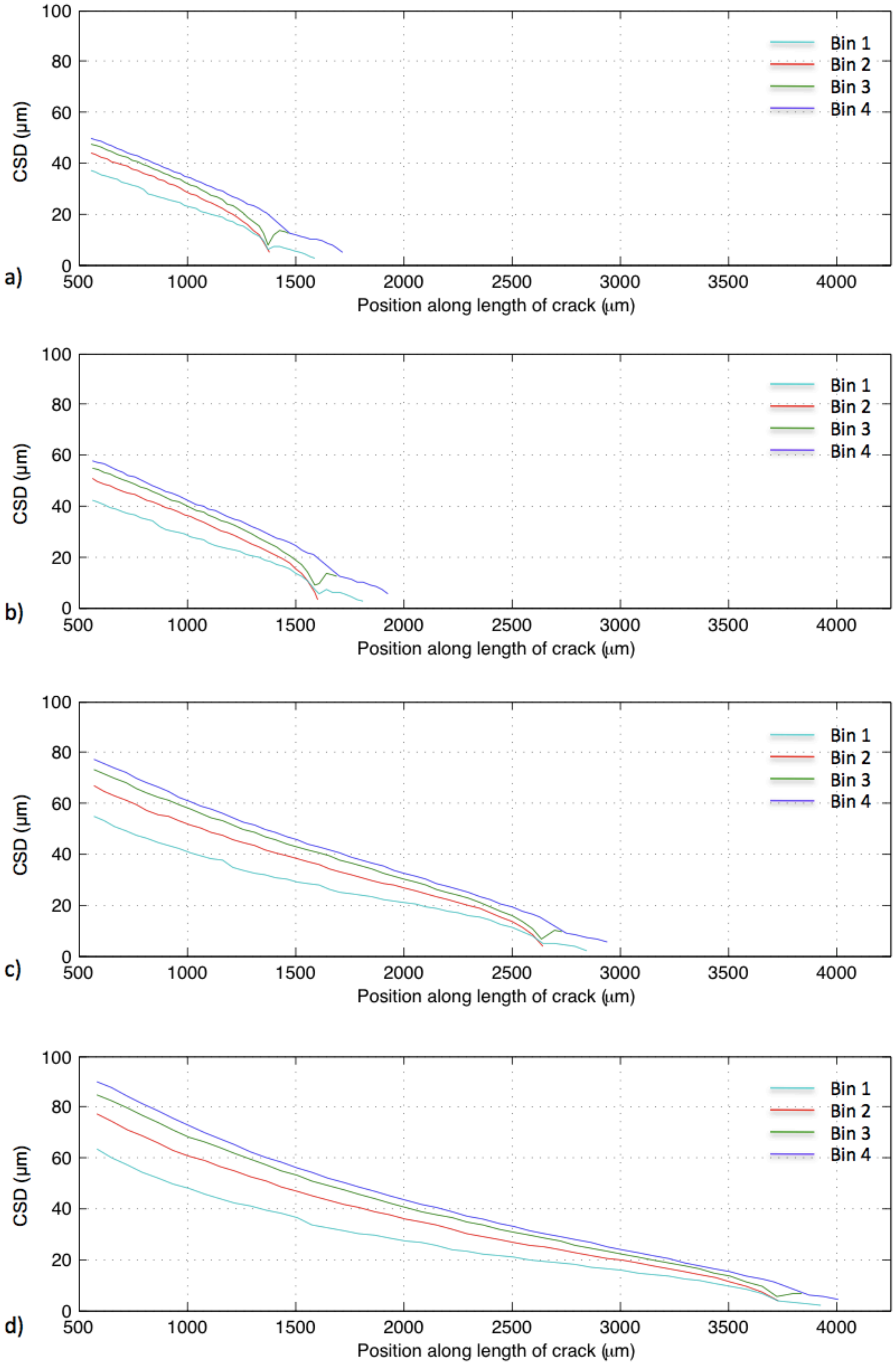

Figure 7.13: Plots of pinned finite element model predictions of CSD along the crack length at loads corresponding to increasing percent failure strength. (a) 65% σ_f, (b) 70% σ_f, (c) 80% σ_f, (d) 90% σ_f. Combined contribution from mechanical load and thermal residual stress.

plots increases as the crack extends. Coupled with the data in Figure 7.12, in which the difference in absolute value between the 0/90 interface, mid-ply region and 0/0 interface is shown to be large, the model predicts that the increase in CSD as the crack extends is much more pronounced at the 0/0 interface. Due to the large change in CSD through the thickness, significant loss off data resolution occurs during the binning and averaging process in both the model and experiment data, and therefore care must be taken that a similar comparison between data sets is made.

The model predicts larger values for the displacement fields compared with the measurements from experiment data. Analysis of the SRCT volumes shows that bridging ligaments exist along the entire surface of the split, with corresponding tractions that will result in lower CSD and COD compared to the model. This observation further illustrates that additional microstructural and micromechanical details should be included in future modelling work.

7.2.3.3 Crack length *vs.* load

The strain energy release rate (SERR) has been calculated using the virtual crack closure technique in which the energy term is determined from the forces ahead, and displacements in the wake of the crack tip for the 0° ply split. Figure 7.14 shows the graph of predicted G_{IC} and G_{IIC} with crack length for separated components of thermal residual stress and mechanical load for the benchmark model in and the pinned model. Consistent with the SERR calculations for the benchmark un-pinned model, and with the predictions of sliding displacement for the pinned model, the 0° ply split is mode II dominated. The values of mode I strain energy release rate are 250% to 300% greater than those for the unpinned model, however the ratio of contribution from the thermal to mechanical components is similar to the un-pinned model, in which approximately half of the opening displacement is accounted for in the unloaded (thermally induced) load-state [130]. The thermal contribution to mode II SERR remains negligible with respect to the mechanical contribution, which has increased by approximately 160% in comparison with the un-pinned predictions at the peak value. A further effect of the pinning on mode II SERR is evident from a comparison between the gradient of the plot for the pinned and un-pinned models. The change in SERR with crack length is steeper for the model with a pinned crack front, indicating that the pinned model would approach a similar value of SERR to the un-pinned model as the crack extends away from the influence of the notch. The magnitude and gradient of the SERR plots suggests that, for constant G_{IIC}, initial crack propagation close to the notch will be more rapid with a pinned crack front, with the rate of new crack surface formation decreasing at a lower crack length. Further analysis with extended crack lengths would provide a better understanding of the effect of pinning of the crack driving force.

Further differences between the modelling approaches are illustrated by the comparison in Figure 7.15 in which the change in SERR along the crack front is identified for the pinned and un-pinned models. Each plot shows the contribution to the energy term for the mode I and model II SERR and the corresponding length of the crack along the crack front for a simulated load of 80% UTS. Figure 7.15a and Figure 7.15b shows the contribution to SERR for the un-pinned and pinned models respectively.

Despite the similar values of COD and, to a lesser degree, values of CSD between the pinned un-pinned models, the contribution to G_I and G_{II} in Figure 7.15 shows that the crack front pinning has a dramatic effect on the crack driving energy. As expected, the un-pinned model predictions indicate that the SERR will exhibit a smooth transition from a maximum value at the $0°/0°$ interface to a value of zero at the constrained $0°/90°$ interface. This trend is also observed in the pinned model, however it acts in conjunction with the more pronounced effect on the energy values of the gradient of the crack front trajectory. Two principal peak values are observed, which correspond to maximum pinning of the crack front. Locations of maximum change in energy occur in the regions where there is a change in gradient of the pinning geometry.

It should be noted that if a constant value of G_C is assumed, the maximum energy values correspond to regions where the maximum generation of crack surface should occur. This is in contradiction to the profile of the pinned model plots, indicating that the modification of the crack front geometry to simulate experiment observations introduces artefacts into the numerical solution; that the quality and shape of the elements (due to the distortion that results from the crack front trajectory within the mesh) has a detrimental effect on the behaviour of the mesh; or that the local variation in fracture toughness in regions where the pinning occurs results in a corresponding variation in G_C that dominates the resistance to crack growth. These considerations should be addressed in any future modelling work.

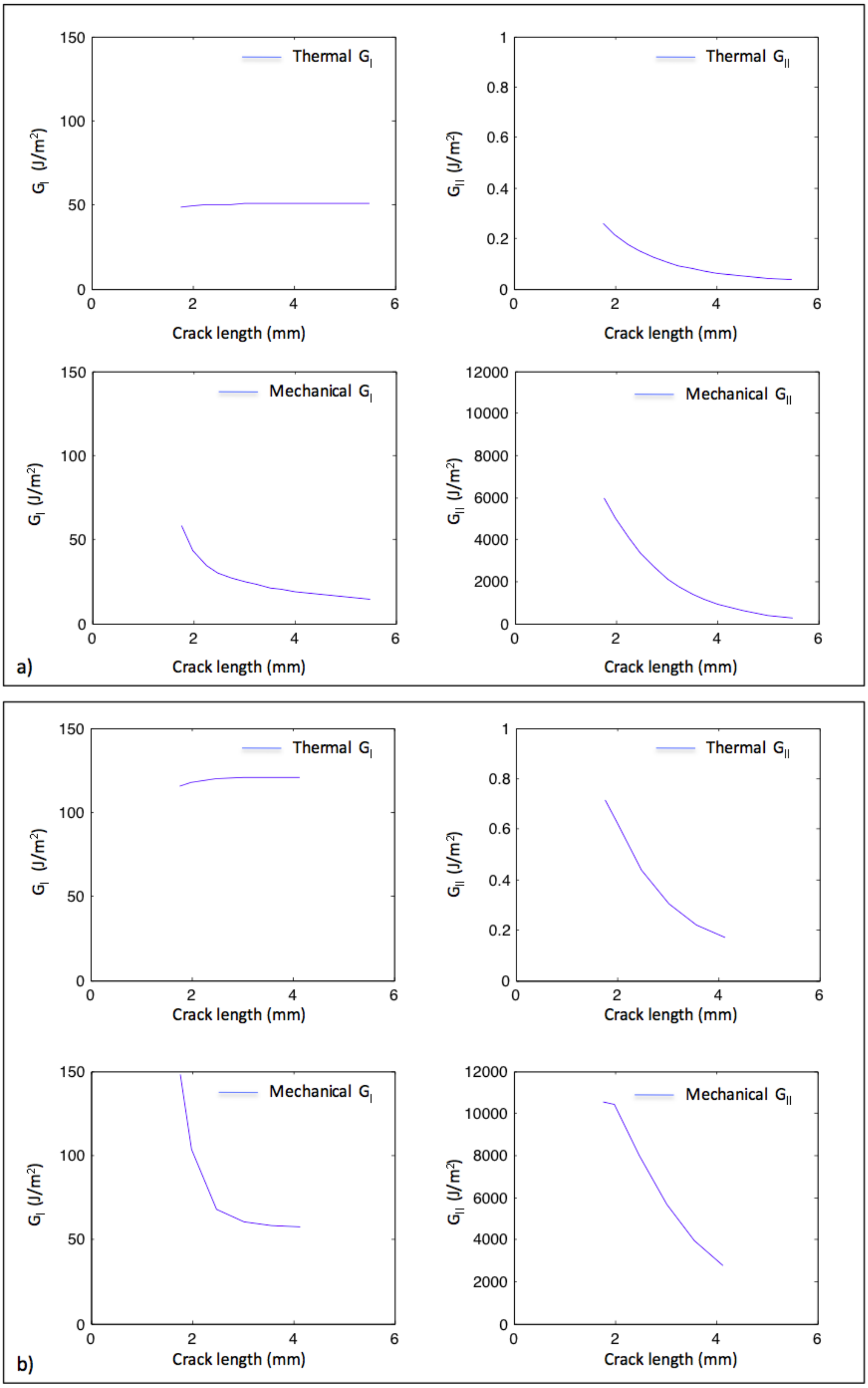

Figure 7.14: Plots of finite element predictions for G_I and G_{II} *vs.* crack length for separated mechanical and thermal components. (a) Unpinned model, (b) pinned model.

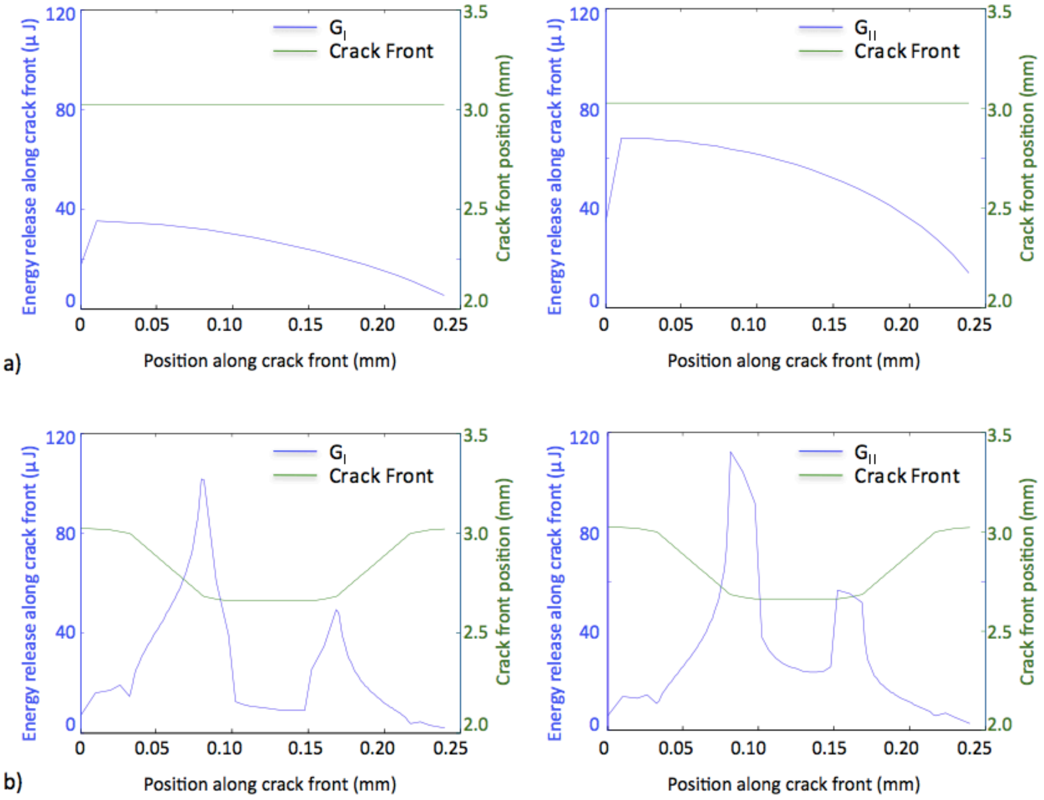

Figure 7.15: Plots of the variation in contribution to SERR along the crack front according to crack front shape. (a) Un-pinned model, (b) pinned model. Combined contribution from mechanical load and thermal residual stress.

7.3 Conclusion

The use of *in situ* SRCT enables the full extent of damage growth to be captured for comparison with model predictions and the results presented here provide an insight into the interaction of mechanisms that govern the accumulation of damage. Previous comparisons for model predictions of crack opening and sliding displacements have shown only a weak correlation to the experimental data, due predominantly to the complexity of the damage mechanisms and local material heterogeneity. The identification of key features and toughening effects from direct SRCT observations have been modelled explicitly, and while some damage parameters have been more accurately predicted due to the inclusion of a pinned crack front, it is clear that the behaviour of the laminate has not been adequately captured. The results of this work demonstrate that large variations in predicted displacement fields are obtained for modest adjustments in material properties and toughening effects, even for this simplified model of a single 0° split. There are still large discrepancies between experimental results and the model predictions, with a stronger correlation between mode I opening and a considerably weaker correlation for mode II behaviour when pinning is introduced. The principal contribution to the discrepancy between model and experiment data arises from the effect of the absence of matrix cracking in 90° plies, delaminations and the interactions at the microstructural scale. While the effect of toughening, resin-rich regions and crack pinning have been modelled through material properties and geometry, fundamental interactions such as reduction in stiffness due to matrix cracking and delaminations have not been accounted for. For more complete modelling, with the inclusion of additional damage mechanisms, the potential complexity of the system increases dramatically. The effect of local microstructure on laminate behaviour and global material properties for carbon-epoxy composites in terms of morphology, interactions of damage mechanisms and resistance to crack growth is therefore a critical consideration if accurate model representation is to be achieved. This observation has significant implications for the micromechanical approach to modelling composite failure processes.

CHAPTER 8

CONCLUSIONS AND FUTURE WORK

High resolution synchrotron radiation computed tomography has been used to obtain qualitative observations and quantitative measurements of damage growth in laminated carbon fibre-epoxy composites for a variety of practical lay-up configurations. The SRCT volumes represent a unique data set in which the interactions of principal mechanisms involved in composite failure processes have been identified. A 3-D finite element model has been constructed to simulate the observed 0° ply splitting in a $[90/0]_S$ laminate in parallel with a detailed analysis of the SRCT data sets. The FE predictions for mode I opening displacements, mode II sliding displacements, and crack extension with load were compared with the experimental results to evaluate the suitability and capability of SRCT as a technique to inform model development and assess their performance. Following this work, concluding remarks are presented, and the implication of these conclusions on the applications of SRCT data for further characterisation and modelling of composite damage is discussed.

8.1 Conclusions

- SRCT has been validated as a powerful tool for the characterization of material microstructure and damage interactions. The use of *in situ* SRCT enables the full extent of damage growth to be captured for comparison with model predictions and the results presented here provide an insight into the interaction of mechanisms that govern the accumulation of damage. Reconstruction and analysis of SRCT volumes has enabled the bulk microstructure and *in situ* damage growth of polymer composite materials to be characterised in three dimensions on a scale not previously obtainable in non-destructive testing. Contiguous damage has been mapped with exceptional spatial fidelity throughout PMC laminates with applied lay-up configurations. The images presented in this work demonstrate the ability to obtain structural information in 3-D on a microscopic scale, providing the opportunity to gain a deeper understanding of damage growth and failure in composite materials.

- Splitting in the 0° plies has been studied in particular detail to evaluate the complex crack morphology in toughened composite materials. Toughening particles have been identified in the resin-rich regions in which both crack pinning and bridging mechanisms have been observed. In the regions where fibres are more densely packed, the splits are less constrained and appear able to advance more freely. Using microstructural features it has been possible to resolve local displacement fields around the intralaminar 0° splits to calculate crack opening and sliding displacements along the length of the splits. This information has been used to inform the development of a finite element model of the intralamina damage. SRCT imaging and analysis allows internal, micron-scale damage to be resolved, offering a unique approach for comparison with model predictions under loading conditions of interest. The initial model construction was in reasonable agreement with the trends of COD and CSD, however there was significant deviation in magnitude. This was attributed to the global homogenisation of each ply within the model, in contrast to the widespread variation in microstructural detail observed in SRCT volumes.

- The influence of microstructural features such as resin rich regions, crack front pinning and local toughening on laminate behaviour was explored through additional FE modelling in which the effects of these features were represented directly, or approximated using adjusted material properties. The adjusted model predictions also showed a weak correlation to the absolute values of the experimentally determined results, however the general trends in behaviour were captured more accurately. In addition, the virtual crack closure technique was employed to calculate the strain energy release rate at the crack tip. The SERR was used to predict crack growth with load using a constant value of G_C for additional comparison with experiment data. The model over-predicted the extent of crack growth, indicating along with the COD and CSD results that simple approximations are not capable of accounting for the accumulated effects of the interacting damage mechanisms and that inhomogeneities and local variations in laminate properties must be modelled explicitly. Comparison with the SRCT data highlighted particular micromechanical detail that was not adequately addressed by the model. Key considerations included: the difficulty in selecting a single split length within the 0° ply due to the shape of the crack front; incomplete characterisation of laminate microstructure and differences in resin rich regions with respect to high fibre density regions; poor approximation of the effect of toughening due to pinning and local variation in fracture toughness due to mechanisms such as fibre bridging and de-bonding of the rubber toughening particles within the matrix. Although the model provided limited predictive capability, the model-experiment comparison provided an insight towards the features that must be included in any micromechanical description of composite damage. In addition, the application of high fidelity computed tomography data to inform model development was demonstrated. The richness of such data opens up the possibility of 'data rich mechanics' in which models for material response can be completely calibrated to the local micromechanical behaviour.

- The greatest difference between the observed experimental laminate damage and the model construction was the shape of the crack front. The pinned crack front was included in the final iteration of model developments to determine its effect on the displacement fields surrounding the 0° ply split and on the strain energy release rate. The pinned crack front model predictions were in closer agreement with experimental results than the un-pinned model, however the displacements and SERR were still significantly over-estimated. The contribution to SERR was plotted along the trajectory of the crack front, which showed that the introduction of pinning results in large variations of crack driving force through the laminate. The trajectory of the pinned crack front was constructed using tied surfaces between element sets in the region surrounding the 0° ply split, resulting in a reduction in the stiffness of the mesh. This illustrates that, in addition to the laminate material behaviour, the approach for constructing the model mesh must also be validated for finite element models.

- The observations presented in this work have significant implications for the micromechanical approach to modelling composite failure processes. Despite modelling explicitly the key features and toughening effects from direct SRCT observations, it is apparent that the behaviour of the laminate has not been adequately captured. Large variations in predicted displacement fields are obtained for modest adjustments in material properties and toughening effects for the simplified model of a single 0° split. For models that intend to simulate delamination, off-axis matrix cracking, toughening due to particle de-bonding and fibre-bridging for a more complete set of laminate damage, the inclusion of additional damage mechanisms would increase the complexity of the system dramatically. The effect of local microstructure on laminate behaviour and global material properties for carbon-epoxy composites in terms of morphology, interactions of damage mechanisms and resistance to crack growth is therefore a critical consideration if accurate model representation is to be achieved.

8.2 Future work

8.2.1 Experimental

- The specimens used in the experimental program described in Chapter 3 are small, with a net section width of just 4 mm, since the high resolution images obtained using SRCT are achieved at the cost of specimen size. In addition, the quality of the reconstructed images is dependent on the transmission of the synchrotron radiation through the specimen and therefore best suited to geometry with constant axial cross section. While the damage characterisation presented in this work provides unique insight into the failure of laminated polymer matrix composites, the data is less relevant to practical applications where the length scales of laminates are several orders of magnitude greater, and generally have a high aspect ratio cross-section. A further study of *in situ* laminate damage growth for a greater variety of specimen sizes and geometries would provide a more complete data set for comparison with models aimed at practical engineering structures.

  Micro-focus X-ray CT could be used for larger specimens with a corresponding reduction in volume resolution, however synchrotron radiation computed laminography (SRCL) is an emerging technology which may enable a study of larger specimens, while maintaining a greater spatial resolution with respect to other characterisation techniques. The technique is similar to SRCT, with the axis of specimen rotation inclined towards the incident X-ray beam. The inclination of the axis presents a more uniform projected area to the beam when used with planar specimens and achieves an effective compromise between specimen size and image resolution [147].

- The majority of the splitting in the 0° plies occurred between loads of 70% σ_f and 80% σ_f. Repetition of the experiment sets with further refinement in load steps between 60% σ_f and 80% σ_f would capture earlier stages of damage initiation and produce a more detailed map of damage growth for 0° splitting. Similarly, refinement in load steps between 30% σ_f and 60% σ_f would provide important damage growth data for transverse ply cracks. The additional observations would assist calibration of model behaviour for particular mechanisms and provide a larger data set for comparison with model predictions.
- The specimens used within this investigation are simple laminate constructions and represent an approximation to notched structural components with a more practical stacking sequence. Damage was introduced into the specimens by the application of static tensile loads. The combination of specimen structure and load case constitutes a single permutation of service conditions. Expansion of the experiment program to include, for example, compression after impact and fatigue load cases; and environmental conditions, such as temperature extremes and high humidity, would provide further important insights into composite damage progression.

8.2.2 Modelling

- There is significant scope to extend the modelling work presented here to include additional damage mechanisms and improve the construction of the mesh. Delaminations and transverse ply cracks must be included for more complete modelling of laminate failure, however the present approach for scripted mesh generation would require additional element blocks to achieve this. The current use of nodes in the pinned model is not efficient, and the limit of node numbering for implementation in ABAQUS™ has been reached for the maximum observed split length. In order to adapt the mesh with the inclusion of additional sections, larger model geometries or refined mesh densities, the meshing script would need to be modified. An investigation into the trajectory and shape of the elements that comprise the pinned crack front geometry should also be performed to evaluate the effect on mesh behaviour.

- The SRCT data sets offer the opportunity to develop additional modelling approaches. Progression towards a non-linear analysis could be achieved through the placement of cohesive elements at locations corresponding to experimentally observed damage processes [148]. Cohesive zone models have shown the potential to simulate damage mechanisms and the effect of local microstructure for good predictions of laminate behaviour, such as crack initiation and propagation. Observations and measurements from experimental data for particular areas of laminates, for example resin rich ply interfaces containing rubber toughening particles, may be used to calibrate cohesive law parameters that define element behaviour in the corresponding area to account for the variations in fracture toughness through the laminate that arise from the complex interactions of multiple damage mechanisms. In addition, the segmented damage within SRCT volumes indicates that matrix cracking in the 0° and 90° plies is not symmetric. The use of cohesive interface elements in regions containing material inhomogeneities such as toughening particles and resin-rich regions may provide useful predictions for non-uniform initiation and propagation of laminate damage. While initial studies of transverse ply cracks in 90° plies has been carried out [135], there is significant scope to extend this work with a CZM approach to enable matrix cracks to develop and examine the effect on laminate behaviour.

8.2.3 Image processing

- The post processing of SRCT volume reconstruction is one of the most important considerations for future work. Data reduction for model-experiment comparisons was limited in specimen sample size due to the intensive manual work required to generate the results. Further research into high fidelity automatic segmentation and feature extraction processes would allow a more complete quantification of the damage mechanisms that are subject to a high degree of statistical variation such as fibre failure. More than 160 specimens were scanned using high resolution SRCT at a variety of loads within the experimental program for this work. Automated identification and quantification of delaminations and matrix cracking would provide a comprehensive repository of fully characterised laminate failure to complement the raw volumes that are currently available from the University of Southampton Materials Data Centre.

REFERENCES

[1] http://www.easa.europa.eu/certification. JAR 25.603.

[2] FAA Workshop for Composite Damage Tolerance and Maintenance (2006).

[3] Maimi, P., Camanho, P.P., Mayugo, J.A., Davila, C.G., A continuum damage model for composite laminates: Part I - Constitutive model. *Mechanics of Materials*, 2007, **39**(10): pp. 897-908.

[4] Maimi, P., Camanho, P.P., Mayugo, J.A., Davila, C.G., A continuum damage model for composite laminates: Part II - Computational implementation and validation. *Mechanics of Materials*, 2007, **39**(10): pp. 909-919.

[5] Yokozeki, T., Shinji, O., Shunsuke, Y., Toshio, O., Simple constitutive model for nonlinear response of fiber-reinforced composites with loading-directional dependence. *Composites Science and Technology*, 2007, **67**(1): pp. 111-118.

[6] Barbero, E.J., Abdelal, G.F., Caceres, A., A micromechanics approach for damage modeling of polymer matrix composites. *Composite Structures*, 2005, **67**(4): pp. 427-436.

[7] Davila, C.G., P.P. Camanho, Rose, C.A., Failure criteria for FRP laminates. *Journal of Composite Materials*, 2005, **39**(4): pp. 323-345.

[8] McCartney, L.N., Energy-based prediction of progressive ply cracking and strength of general symmetric laminates using an homogenisation method. *Composites Part A: Applied Science and Manufacturing*, 2005, **36**(2): pp. 119-128.

[9] Gotsis, P.K., Chamis, C.C., Minnetyan, L., Application of progressive fracture analysis for predicting failure envelopes and stress-strain behaviors of composite laminates: a comparison with experimental results. *Composites Science and Technology*, 2002, **62**(12-13): pp. 1545-1559.

[10] Soden, P.D., Hinton, M.J., Kaddour, A.S., A comparison of the predictive capabilities of current failure theories for composite laminates. *Composites Science and Technology*, 1998, **58**(7): pp. 1225-1254.

[11] Hinton, M.J., Kaddour, A.S., Soden, P.D., A comparison of the predictive capabilities of current failure theories for composite laminates, judged against experimental evidence. *Composites Science and Technology*, 2002, **62**(12-13): pp. 1725-1797.

[12] Hinton, M.J., Kaddour, A.S., Soden, P.D., A further assessment of the predictive capabilities of current failure theories for composite laminates: comparison with experimental evidence. *Composites Science and Technology*, 2004, **64**(3-4): pp.549-588.

[13] Li, S., Thouless, M.D., Waas, A.M., Schroeder, J.A., Zavattieri, P.D., Mixed-mode cohesive-zone models for fracture of an adhesively bonded polymer-matrix composite. *Engineering Fracture Mechanics*, 2006, **73**(1): pp. 64-78.

[14] Cox, B. and Yang, Q.D., In Quest of Virtual Tests for Structural Composites. *Science*, 2006, **314**(5802): pp. 1102-1107.

[15] Dugdale, D.S., Yielding of steel sheets containing slits. *Journal of the Mechanics and Physics of Solids*, 1960, **8**(2): pp. 100-104.

[16] Barenblatt, G.I., The Mathematical Theory of Equilibrium Cracks in Brittle Fracture. *Advances in Applied Mechanics*, 1962, **8**: pp. 55-129.

[17] Yang, Q.D. and Cox, B., Cohesive models for damage evolution in laminated composites. *International Journal of Fracture*, 2005, **133**(2): pp. 107-137.

[18] Dr Polly Sinnet-Jones, University of Southampton, Department of Engineering Materials.

[19] Dr Xiaowei Fu, University of Southampton, Department of Engineering Materials.

[20] Dr Andrew Moffat, University of Southampton, Department of Engineering Materials.

[21] Dr Mark Mavrogordato, University of Southampton, Department of Engineering Materials.

[22] Hull, D. and Clyne, T.W., An Introduction to Composite Materials. Cambridge University Press Cambridge, 1996.

[23] Jones, R.M., Mechanics of Composite Materials (2nd Edition). Brunner-Routledge Press New York, 1999.

[24] Daniel, I.M. and Ishai, O., Engineering Mechanics of Composite Materials (2nd edition). Oxford University Press New York, 2006.

[25] Peters, S.T., Handbook of Composites (2nd Edition). Springer Press: Verlag, 1998.

[26] Sutherland, L. S., Shenoi, R. A., Lewis, S. M., Size and scale effects in composites: I. Literature review. *Composites Science and Technology*, 1999, **59**(2): pp. 209-220.

[27] Talreja, R., Stiffness properties of composite laminates with matrix cracking and interior delamination. *Engineering Fracture Mechanics*, 1986, **25**(5-6): pp. 751-762.

[28] Xu, L.-Y., Interaction between matrix cracking and edge delamination in composite laminates. *Composites Science and Technology*, 1994, **50**(4): pp. 469-478.

[29] Ogihara, S., Takeda, N., Kobayashi, A., Experimental characterization of microscopic failure process under quasi-static tension in interleaved and toughness-improved CFRP cross-ply laminates. *Composites Science and Technology*, 1997, **57**(3): pp. 267-275.

[30] Rebiere, J. -L., Maatallah, M.-N., Gamby, D., Analysis of damage mode transition in a cross-ply laminate under uniaxial loading. *Composite Structures*, 2002, **55**(1): pp. 115-126.

[31] Kortschot, M.T. and Beaumont, P.W.R., Damage Mechanics of Composite Materials. I: Measurements of Damage and Strength. *Composites Science and Technology*, 1990, **39**(4): pp. 289-301.

[32] Spearing, S.M. and Beaumont, P.W.R., Fatigue damage mechanics of composite materials. I: Experimental measurement of damage and post-fatigue properties. *Composites Science and Technology*, 1992, **44**(2): pp. 159-168.

[33] Sorensen, L., Botsis, J., Gmur, Th., Humbert, L., Bridging tractions in mode I delamination: Measurements and simulations. *Composites Science and Technology*, 2008, **68**(12): pp. 2350-2358.

[34] Griffith, A.A., The Phenomena of Rupture and Flow in Solids. *Philosophical Transactions, Series A*, 1920, **221**: pp. 163-198.

[35] Irwin, G.R., Fracture Dynamics. Fracturing of Metals, American Society for Metals, Cleveland, 1948. pp. 147-166.

[36] Anderson, T.L., Fracture Mechanics Fundamentals and Applications. CRC Press: New York, 1995.

[37] Rice, J.R., A Path Independant Integral and the Approximate Analysis of Strain Concentration by Notches and Cracks. *Journal of Applied Mechanics*, 1968, **35**: pp. 379-386.

[38] Cherepanov, G. P., Crack Propagation in Continuous Media. *Journal of Applied Mathematics and Mechanics*, 1967, **31**(3): pp. 503-512.

[39] Wisnom, M.R., Khan. B., Hallett. S.R., Size effects in unnotched tensile strength of unidirectional and quasi-isotropic carbon/epoxy composites. *Composite Structures*, 2008, **84**(1): pp. 21-28.

[40] Wisnom, M. R., Size effects in the testing of fibre-composite materials. *Composites Science and Technology*, 1999, **59**(13): pp. 1937-1957.

[41] Hitchon, J.W., Phillips, D.C., The effect of specimen size on the strength of CFRP. *Composites*, 1978, **9**(2): pp. 119-124.

[42] Spearing, S.M., Lagace, P.A., McManus, H.L.N., On the Role of Lengthscale in the Prediction of Failure of Composite Structures: Assessment and Needs. *Applied Composite Materials*, 1998, **5**: pp. 139-149.

[43] Zweben, C., Rosen, B.W., A statistical theory of material strength with application to composite materials. *Journal of the Mechanics and Physics of Solids*, 1970, **18**(3): pp.189-206.

[44] Zweben, C., Designer's corner: Is there a size effect in composites? *Composites*, 1994, **25**(6): pp.451-454.

[45] Tabiei, A., Sun, J., Statistical aspects of strength size effect of laminated composite materials. *Composite Structures*, 1999, **46**(3): pp. 209-216.

[46] Thoppul, S. D., Finegan, J., Gibson, R.F., Mechanics of mechanically fastened joints in polymer-matrix composite structures - A review. *Composites Science and Technology*, 2009, **69**(3-4): pp. 301-329.

[47] Scott, I.G., Scala, C.M., A review of non-destructive testing of composite materials. *NDT International*, 1982, **15**(2): pp. 75-86.

[48] Reynolds, W.N, Nondestructive testing (NDT) of fibre-reinforced composite materials. *Materials & Design*, 1984-1985, **5**(6): pp. 256-270.

[49] Greenhalgh ES, Hiley MJ. Fractography of polymer composites: current status and future issues. In: Proceedings of ECCM-13, Stockholm, Sweden; 2008.

[50] Kim, J.-K., MacKay, D.B., Mai, Y.-W., Drop-weight impact damage tolerance of CFRP with rubber-modified epoxy matrix. *Composites*, 1993, **24**(6): pp. 485-494.

[51] Williams, G.J., Bond, I.P., Trask, R.S., Compression after impact assessment of self-healing CFRP. *Composites Part A: Applied Science and Manufacturing, Special Issue: Repair*, 2009, **40**(9): pp. 1399-1406.

[52] Faraz, A., Biermann, D., Weinert, K., Cutting edge rounding: An innovative tool wear criterion in drilling CFRP composite laminates. *International Journal of Machine Tools and Manufacture*, 2009, **49**(15) pp. 1185-1196.

[53] Mouritz, A. P. , Townsend, C., Shah Khan, M. Z., Non-destructive detection of fatigue damage in thick composites by pulse-echo ultrasonics. *Composites Science and Technology*, 2000, **60**(1): pp. 23-32.

[54] Yashiro, S., Takatsubo, J., Toyama, N., An NDT technique for composite structures using visualized Lamb-wave propagation. *Composites Science and Technology*, 2007, **67**(15-16): pp.3202-3208.

[55] Yolken, H.T., Matzkanin, G.A., Nondestructive Evaluation of Advanced Fiber Reinforced Polymer Matrix Composites - A Technology Assessment. LF99-7709/NASA/CR-2009-215566, 2009.

[56] Pierce, S. G., Dong, F., Atherton, K., Culshaw, B., Worden, K., Manson, G., Monnier, T., Guy, P., Baboux, J.-C., Assad, J., Moulin, E., Grondel, S., Delebarre, C., Agostini, V., Delsanto, P.-P., Genesio, I., Mino, E., Boller, C., Damage assessment in smart composite structures: the DAMASCOS programme. *Air & Space Europe*, 2001, **3**(3-4): pp. 132-138.

[57] Summerscales, J. (Ed.), 1987. Non-Destructive Testing of Fiber-Reinforced Plastic Composites, volume 1. Elsevier, Amsterdam.

[58] Kortschot, M. T., Zhang, C. J., Characterization of composite mesostructures and damage by de-ply radiography. *Composites Science and Technology*, 1995, **53**(2): pp. 175-181.

[59] Wyrick, D.A., Adams, D.F., Damage sustained by a carbon/ epoxy composite material subjected to repeated impact. *Composites*, 1988, **19**(1): pp. 19-27.

[60] Stinchcomb, W.W., Nondestructive evaluation of damage accumulation processes in composite laminates. *Composites Science and Technology*, 1986, **25**(2): pp. 103-118.

[61] Kessler, S. S., Spearing, S.M., Atalla, M.J., Cesnik, C.E.S., Soutis, C., Damage detection in composite materials using frequency response methods. *Composites Part B: Engineering*, 2002, **33**(1): pp. 87-95.

[62] Maire, E., Bordreuil, C., Babout, L., Boyer, J.-C., Damage initiation and growth in metals. Comparison between modelling and tomography experiments. *Journal of the Mechanics and Physics of Solids*, 2005, **53**(11): pp. 2411-2434.

[63] Salvo, L., Cloetens, P., Maire, E., Zabler, S., Blandin, J. J., Buffière, J. Y., Ludwig, W., Boller, E., Bellet, D., Josserond, C., X-ray micro-tomography an attractive characterisation technique in materials science. *Nuclear Instruments and Methods in Physics Research Section B: Beam Interactions with Materials and Atoms*, 2003, **200**: pp. 273-286.

[64] Awaja, F., Arhatari, B.D., X-ray Micro Computed Tomography investigation of accelerated thermal degradation of epoxy resin/glass microsphere syntactic foam. *Composites Part A: Applied Science and Manufacturing, Special Issue: 15th French National Conference on Composites*, 2009, **40**(8): pp. 1217-1222.

[65] Wang, L. B., Frost, J. D., Voyiadjis, G. Z, Harman, T. P., Quantification of damage parameters using X-ray tomography images. *Mechanics of Materials: Multi-scale Modeling of Materials*, 2003, **35**(8): pp. 777-790.

[66] Hounsfield, G. N. Computerized transverse axial scanning (tomography): Part 1. Description of system. *British Journal of Radiology*, 1973, **46**: pp. 1016-1022.

[67] Landis, E.N., Keane, D.T., X-ray microtomography. *Materials Characterization*, 2010, **61**(12): pp.1305-1316.

[68] Maire, E., Buffière, J. Y., Salvo, L., Blandin, J. J., Ludwig, W. and LÃ©tang, J. M., On the Application of X-ray Microtomography in the Field of Materials Science. *Advanced Engineering Materials*, 2001, **3**: pp. 539-546.

[69] Krimmel, S., Baumann, J., Kiss, Z., Kuba, A., Nagy, A., Stephan, J., Discrete tomography for reconstruction from limited view angles in non-destructive testing. *Electronic Notes in Discrete Mathematics: Proceedings of the Workshop on Discrete Tomography and its Applications*, 2005, **20**: pp. 455-474.

[70] Kak, A.C. and Slaney, M., Principles of Computerized Tomographic Imaging. IEEE Press: New York, 1988.

[71] Stock SR, MicroComputed Tomography: Methodology and Applications. Boca Raton: FLCRC Press, Taylor & Francis Group; 2009.

[72] Baruchel, J., Buffière, J-Y., Cloetens, P., Di Michiel, M., Ferrie, E., Ludwig, W., Maire, E., Salvo, L., Advances in synchrotron radiation microtomography. *Scripta Materialia*, 2006, **55**(1): pp. 41-46.

[73] Banyay, G.A., Shaltout, M. M., Tiwari, H., Mehta, B. V., Polymer and composite foam for hydrogen storage application. *Journal of Materials Processing*, Technology, 2007, **191**(1-3): pp. 102-105.

[74] Bayraktar, E., Bessri, K., Bathias, C., Deformation behaviour of elastomeric matrix composites under static loading conditions. *Engineering Fracture Mechanics*, 2008, **75**(9): pp. 2695-2706.

[75] Bayraktar, E., Antolonovich, S., Bathias, C., Multiscale study of fatigue behaviour of composite materials by X-rays computed tomography. *International Journal of Fatigue*, 2006, **28**(10): pp. 1322-1333.

[76] Torquato, S., Modeling of physical properties of composite materials. *International Journal of Solids and Structures*, 2000, **37**(1-2): pp. 411-422.

[77] Schilling, P.J., Karedla, B. P. R., Tatiparthi, A. K., Verges, M. A., Herrington, P.D., X-ray computed microtomography of internal damage in fiber reinforced polymer matrix composites. *Composites Science and Technology*, 2005, **65**(14): pp. 2071-2078.

[78] Symons, D.D. Characterisation of indentation damage in 0/90 lay-up T300/914 CFRP. *Composites Science and Technology*, 2000, **60**(3): pp. 391-401.

[79] Shen, H., Nutt, S., Hull, D., Direct observation and measurement of fiber architecture in short fiber-polymer composite foam through micro-CT imaging. *Composites Science and Technology*, 2004, **64**(13-14): pp. 2113-2120.

[80] Tsao, C.C., Hocheng, H., Computerized tomography and C-Scan for measuring delamination in the drilling of composite materials using various drills. *International Journal of Machine Tools & Manufacture*, 2005, **45**: pp.1282-1287.

[81] http: //www.esrf.fr/.

[82] Cloetens, P., Ludwig, W., Baruchel, J., Guigay, J. P., Pernot-Rejmankova, P., Salome-Pateyron, M., Schlenker, M., Buffière, J. Y., Maire, E., Peix, G., Hard X-ray phase imaging using simple propagation of a coherent synchrotron radiation beam. *Journal of Physics D-Applied Physics*, 1999, **32**(10A): pp. A145-A151.

[83] Cloetens, P., Bolle, E., Ludwig, W., Baruchel, J., Schlenke, M., Absorption and phase imaging with synchrotron radiation. *Europhysics News*, 2001, **32**(2): pp. 46-50.

[84] Baruchel, J., Bleuet, P., Bravin, A., Coan, P., Lima, E., Madsen, A., Ludwig, W., Pernot, P., Susini, J., Advances in synchrotron hard X-ray based imaging. *Comptes Rendus Physique*, 2008, **9**(5-6): pp. 624-641.

[85] Snigirev, A., Snigireva, I., Kohn, V., Kuznetsov, S. and Schelokov, I. On the Possibilities of X-ray Phase Contrast Micro-imaging by Coherent High-energy Synchrotron Radiation. *Review of Scientific Instruments*, 1995, **66**(12): pp. 5486-5492.

[86] Spanne, P., Raven, C., Snigireva, I., Snigirev, A., In-line holography and phase-contrast microtomography with high energy X-rays. *Physics in Medicine and Biology*, 1999, **44**(3): pp. 741-749.

[87] Wevers, M., De Meester, P., Microfocus X-ray computer tomography in materials research. Proceedings of the 15th World Conference on Non-Destructive Testing, 2000.

[88] Vidal, F.P., Letang, J.M., Peix, G., Cloetens, P., Investigation of artefact sources in synchrotron microtomography via virtual X-ray imaging. *Nuclear Instruments and Methods in Physics Research Section B: Beam Interactions with Materials and Atoms*, 2005, **234**(3): pp. 333-348.

[89] www.e-radiography.net.

[90] Kataoka, M.L., Hochman, M.G., Rodriguez, E.K., Lin, P.-J.P., Kubo, S., Raptopolous, V. D., A review of factors that affect artifact from metallic hardware on multi-row detector computed tomography. *Current Problems in Diagnostic Radiology*, 2010, **39**(4): pp. 125-136.

[91] Krumm, M., Kasperl, S., Franz, M., Reducing non-linear artifacts of multi-material objects in industrial 3D computed tomography. *NDT & E International*, 2008, **41**(4): pp. 242-251.

[92] Xu, F., Hu, X.-F., Miao, H., Zhao, J.-H., In situ investigation of ceramic sintering by synchrotron radiation X-ray computed tomography. *Optics and Lasers in Engineering*, 2010, **48**(11): pp. 1082-1088.

[93] Morgeneyer, T. F., Starink, M. J., Sinclair, I., Evolution of voids during ductile crack propagation in an aluminium alloy sheet toughness test studied by synchrotron radiation computed tomography. *Acta Materialia*, 2008, **56**(8): pp. 1671-1679.

[94] Khor, K. H., Buffière, J. Y., Ludwig, W., Sinclair, I., High resolution X-ray tomography of micromechanisms of fatigue crack closure. *Scripta Materialia*, 2006, **55**(1): pp. 47-50.

[95] Moffat, A. J., Barnes, S., Mellor, B. G., Reed, P. A. S., The effect of silicon content on long crack fatigue behaviour of aluminium-silicon piston alloys at elevated temperature. *International Journal of Fatigue*, 2005, **27**(10-12): pp. 1564-1570.

[96] Requena, G., Cloetens, P., Altendorfer, W., Poletti, C., Tolnai, D., Warchomicka, F., Degischer, H.P., Sub-micrometer synchrotron tomography of multiphase metals using Kirkpatrick-Baez optics. *Scripta Materialia*, 2009, **61**(7): pp.760-763.

[97] Muller, B., Beckmann, F., Huser, M., Maspero, F., Szekely, G., Ruffieux, K., Thurner, P., Wintermantel, E., Non-destructive three-dimensional evaluation of a polymer sponge by micro-tomography using synchrotron radiation. *Biomolecular Engineering*, 2002, **19**(2-6): pp.73-78.

[98] Cosmi, F., Bernasconi, A., Sodini, N., Phase contrast micro-tomography and morphological analysis of a short carbon fibre reinforced polyamide. *Composites Science and Technology*, 2011, **71**(1): pp. 23-30.

[99] Requena, G., Fiedler, G., Seiser, B., Degischer, P., Di Michiel, M., Buslaps, T., 3D-Quantification of the distribution of continuous fibres in unidirectionally reinforced composites. *Composites Part A: Applied Science and Manufacturing*, 2009, **40**(2): pp.152-163.

[100] Almgren, K.M., Gamstedt, E.K., Nygard, P., Malmberg, F., Lindblad, J., Lindstrom, M., Role of fibre-fibre and fibre-matrix adhesion in stress transfer in composites made from resin-impregnated paper sheets. *International Journal of Adhesion and Adhesives*, 2009, **29**(5): pp.551-557.

[101] Forsberg, F., Mooser, R., Arnold, M., Hack, E., Wyss, P., 3D micro-scale deformations of wood in bending: Synchrotron radiation μCT data analyzed with digital volume correlation. *Journal of Structural Biology*, 2008, **164**(3): pp.255-262.

[102] Williams, J.J., Flom, Z., Amell, A.A., Chawla, N., Xiao, X., De Carlo, F., Damage evolution in SiC particle reinforced Al alloy matrix composites by X-ray synchrotron tomography. *Acta Materialia*, 2010, **58**(18): pp.6194-6205.

[103] Raz-Ben Aroush, D., Maire, E., Gauthier, C., Youssef, S., Cloetens, P., Wagner, H.D., A study of fracture of unidirectional composites using in situ high-resolution synchrotron X-ray microtomography. *Composites Science and Technology*, 2006, **66**(10): pp. 1348-1353.

[104] Orifici, A.C., Herszberg, I., Thomson, R.S., Review of methodologies for composite material modelling incorporating failure. *Composite Structures*, 2008, **86**(1-3): pp. 194-210.

[105] Balzani, C., Wagner, W., An interface element for the simulation of delamination in unidirectional fiber-reinforced composite laminates. *Engineering Fracture Mechanics*, 2008, **75**(9): pp. 2597-2615.

[106] Shet, C., Chandra, N., Effect of the shape of T-delta cohesive zone curves on the fracture response. *Mechanics of Advanced Materials and Structures*, 2004, **11**(3): pp. 249-275.

[107] Chandra, N. and C. Shet, A micromechanistic perspective of cohesive zone approach in modeling fracture. *Computer Modeling in Engineering & Sciences*, 2004, **5**(1): pp. 21-33.

[108] Shet, C. and N. Chandra, Analysis of energy balance when using cohesive zone models to simulate fracture processes. *Journal of Engineering Materials and Technology - Transactions of the Asme*, 2002, **124**(4): pp. 440-450.

[109] Espinosa, H.D., S. Dwivedi, and H.C. Lu, Modeling impact induced delamination of woven fiber reinforced composites with contact/cohesive laws. *Computer Methods in Applied Mechanics and Engineering*, 2000, **183**(3-4): pp. 259-290.

[110] Vaughan, T.J., McCarthy, C.T., Micromechanical modelling of the transverse damage behaviour in fibre reinforced composites. *Composites Science and Technology*, In Press: Corrected Proof, Available online 9 December 2010, ISSN 0266-3538, DOI: 10.1016/j.compscitech.2010.12.006

[111] Andersons, J., Tarasovs, S., Sparnins, E., Finite fracture mechanics analysis of crack onset at a stress concentration in a UD glass/epoxy composite in off-axis tension. *Composites Science and Technology*, 2010, **70**(9): pp. 1380-1385.

[112] Zhang, J., Soutis, C., Fan, J., Strain energy release rate associated with local delamination in cracked composite laminates. *Composites*, 1994, **25**(9): pp. 851-862.

[113] Kashtalyan, M., Soutis, C., Analysis of composite laminates with intra- and interlaminar damage. *Progress in Aerospace Sciences*, 2005, **41**(2): pp. 152-173.

[114] Alfano, G., On the influence of the shape of the interface law on the application of cohesive-zone models. *Composites Science and Technology*, 2006, **66**(6): pp. 723-730.

[115] Krueger, R., The Virtual Crack Closure Technique: History,Approach and Applications. 2002. NASA/CR-2002-211628/ ICASE Report No. 2002-10.

[116] Cornell Fracture Group. http://www.cfg.cornell.edu/education/education.htm.

[117] Irwin, G.R., Fracture I, In: *Handbuch der Physik VI, Flügge, Ed.*, 1958, pp. 558-590.

[118] http://www.nikonmetrology.com/

[119] CT-Pro V.2.0, Metris, Tring.

[120] VG StudioMax V.2.0, Volume Graphics, Heidelberg.

[121] ImageJ NIH Image, National Institutes of Health, Maryland.

[122] Amira; V.4.1.1TM Konrad-Zuse-Zentrum fuÂ¨r Informationstechnik Berlin (ZIB), Germany and Mercury Computer Systems.

[123] MATLAB, V.7.10, The MathWorks, Natick.

[124] http: //www.hexcel.com/.

[125] Wright, P.M., Fu, X., Sinclair, I., Spearing, S.M., Ultra high resolution computed tomography of damage in notched carbon fiber-epoxy composites. *Journal of Composite Materials*, 2008, **42**(19): pp. 1993-2002.

[126] Spearing, S.M., Beaumont, P.W.R. and Ashby, M.F., Fatigue damage mechanics of notched graphite-epoxy laminates. In O'Brien, T.K. (ed.), Composite Materials: Fatigue and Fracture, ASTM STP 1110, 1991. pp. 596-616.

[127] Cox, B.N., Spearing, S.M. and Mumm, D.R., Chapter 1: Practical challenges in formulating virtual tests for structural composites. In: Camanho, P. (ed.). Mechanical Response of Composites, Springer. 2008.

[128] Moffat, A.J., Wright, P., Buffière, J.-Y., Sinclair, I., Spearing, S.M., Micromechanisms of damage in 0° splits in a $[90/0]_S$ composite material using synchrotron radiation computed tomography. *Scripta Materialia*, 2008, **59**(10): pp. 1043-1046.

[129] Moffat, A.J., Wright, P., Buffière, J.-Y., Sinclair, I. Spearing, S.M., In situ calibration of cohesive zone models for composite damage. Proceedings of the American Society for Composites 23rd Technical Conference, Memphis.

[130] Wright, P., Moffat, A., Sinclair, I., Spearing, S.M., High resolution tomographic imaging and modelling of notch tip damage in a laminated composite. *Composites Science and Technology*, 2010, **70**(10): pp. 1444-1452.

[131] Marissen R, Westphal T, Sterk JC. Fracture of quasi-isotropic composite sheets with sharp notches. *Composites Science and Technology*, 2006, **66**(11-12): pp. 1803-12.

[132] Hassan, N.M., Batra, R.C., Modeling damage in polymeric composites. *Composites Part B: Engineering*, 2008, **39**(1): pp. 66-82.

[133] Sun, Z., Daniel, I.M., Luo, J.J., Modeling of fatigue damage in a polymer matrix composite. *Materials Science and Engineering A*, 2003, **361**(1-2): pp. 302-311.

[134] Iannucci L, Ankersen J. An energy based damage model for thin laminated composites. *Composites Science and Technology*, 2006, **66**(7-8): pp. 934-51.

[135] Renault, A., Moffat, A.J., Wright, P., Sinclair, I., Spearing, S.M., Direct measurement of transverse ply crack opening using synchrotron X-ray tomography and comparison with models, *Journal of Composite Materials*, in review.

[136] Wright, P., Moffat, A., Fu, X., Buffière, J.-Y., Sinclair, I., Spearing, S.M., Very high resolution computed tomography of damage in laminated composites. Proceedings of the 13th European Conference on Composite Materials, Stockholm.

[137] Toda, H., Sinclair, I., Buffière, J. -Y., Maire, E., Khor, K.H., Gregson, P., Kobayashi, T., A 3D measurement procedure for internal local crack driving forces via synchrotron X-ray microtomography. *Acta Materialia*, 2004, **52**(5): pp. 1305-1317.

[138] ABAQUS/ CAE V.6.9, Dassault Systemes.

[139] http://www.materialsdatacentre.com/.

[140] Mavrogordato, M.N., Wright, P., Helfen, L., Sinclair, I., Spearing, S.M., Assessment of laminate damage micromechanisms using high resolution synchrotron radiation computed tomography & laminography. *Proceedings of the 14th European Conference on Composite Materials, Budapest.*

[141] Wright, P., Moffat, A., Mavrogordato, M.N., Renault, A., Sinclair, I., Spearing, S.M., High resolution computed tomography for modelling laminate damage. Proceedings of the 17th International Conference on Composite Materials, Edinburgh.

[142] Hutchinson, J.W., Suo, Z., Mixed Mode Cracking in Layered Materials. *Advances in Applied Mechanics*, 1992, **29**: pp. 63-191.

[143] Ilyas, M., Lachaud, F., Espinosa, C., Salaün, M., Dynamic delamination of aeronautic structural composites by using cohesive finite elements. Proceedings of the 17th International Conference on Composite Materials, Edinburgh.

[144] Spearing, S.M., Beaumont, P.W.R., Ashby, M.F., Fatigue damage mechanics of composite materials. II: A damage growth model. *Composites Science and Technology*, 1992, **44**(2): pp. 169-177.

[145] Kortschot, M.T., Beaumont, P.W.R., Damage mechanics of composite materials: II - a damaged-based notched strength model. *Composites Science and Technology*, 1990, **39**(4): pp. 303-326.

[146] Scott, A.E, Mavrogordato, M., Wright, P., Sinclair, I., Spearing, S.M., In situ fibre fracture measurement in carbon-epoxy laminates using high resolution computed tomography. *Composites Science and Technology*, 2011, **71**(12): pp. 1471-1477.

[147] Moffat, A.J., Wright, P., Helfen, L., Baumbach, T., Johnson, G., Spearing, S.M., Sinclair, I., In situ synchrotron computed laminography of damage in carbon fibre-epoxy $[90/0]_S$ laminates, *Scripta Materialia*, 2010, **62**(2): pp. 97-100.

[148] Burke-Veliz, A., Mavrogordato, M. N., Wright, P., Moffat, A., Sinclair, I., Spearing, S.M., FE modelling and validation of interacting cohesive zones in CFRP with high resolution imaging. *Proceedings of the 14th European Conference on Composite Materials*, Budapest.